WELDING METALLURGY AND TOUGHNESS IMPROVEMENT

FOR MILD AND LOW-ALLOYED STEEL ELECTROSLAG WELDMENTS

Dawei Yu

B.S., Peking Mechanical Engineering Institute, China, 1968

M.S., Shanghai Jiao-tong University, China, 1981

A dissertation submitted to the faculty
of the Oregon Graduate Center
in partial fulfillment of the requirements
for the degree
Doctor of Philosophy
in
Materials Science and Engineering

March, 1988

The dissertation "Welding Metallurgy and Toughness Improvement for Mild and Low-alloyed Steel Electroslag Weldments" by Dawei Yu has been examined and approved by the following Examination Committee:

Jack H. Devletian, Thesis Advisor
Professor

William E. Wood, Thesis Advisor
Professor

Paul Clayton
Professor

Anthony E. Bell,
Associate Professor

ACKNOWLEDGMENT

The author wishes to express his sincerest appreciation to both Dr. William E. Wood and Dr. Jack H. Devletian for their guidance, continuing patience and encouragement throughout the course of this research work. And, the author sincerely thanks Dr. Paul Clayton and Dr. Anthony E. Bell for examining this dissertation. The author is also grateful to the U.S. Department of Transportation/Federal Highway Administration for financial support under the contract DTFH 61-83-C-00112. The author also wishes to thank Mr. Robert Turbin, Mr.David Roberts and Andy Villeneuve of OGC, and Dr. Khalid Khan and Mr. Tom Stoody of University of Portland for their very kind assistance in the experimental work during this DOT project.

Special thanks are due Dr. Hee-Sung Ann, the author's project partner, for his great co-work.

Words are inadequate to express the author's deep appreciation to his wife, Jennifer (Bingrou Zhang), for her encouragement, support and understanding without equal.

TABLE OF CONTENTS

	Page
ACKNOWLEDGMENT	ii
List of Figures	vi
LIST of Tables	xi
ABSTRACT	xii
I. INTRODUCTION	1
A. Electroslag Welding Technique and Its Current Status	1
B. Statement of Purpose	7
II. BACKGROUND REVIEW	9
A. Property Requirements and Process Improvement in ESW Technique	9
B. Formation of Weld Morphology	12
1. Solidification Structure of Weld Metal	13
2. Austenite Decomposition Products in Weld Metal	16
3. Morphology of Electroslag Weld Metal	20
C. Influence of Alloying Additions on Microstructure and Properties	24
III. EXPERIMENTAL PROCEDURES	31
A. Materials	31
1. Base Materials and Filler Metals	31
2. Flux	33
B. Welding Process	34
1. Equipment	34
2. Guide Plate Design	37
3. Narrow Gap Technique	39
C. Evaluations	41
1. Metallography	41
2. Chemical Analysis	41
3. Hardness	41
4. Charpy V-Notch Toughness	42
5. Plane Strain Fracture Toughness	43
D. Summary of Weld Experiment	43

Page

IV. RESULTS ---------- 46

A. Chemical Composition of Weld Metals ---------- 46

B. Morphological Characteristics of Weld Metal ---------- 47
1. Variation of Solidification and Ferritic Substructures ---------- 47
2. Measurement of Dendrite Arm Spacing ---------- 56
3. Weld Pool Form Factor ---------- 60
4. Solidification Hot Cracking ---------- 66
5. Distribution of Inclusions ---------- 70

C. Effects of Alloying Additions on Microstructure ------- 74
1. Alloying-Induced Equiaxed Dendrites ---------- 74
2. Cr-Mn-Mo Alloying ---------- 74
3. Ni-Mn-Mo Alloying ---------- 77

D. Tubular Vs. Solid Filler Metal ---------- 84

E. HAZ Appearance ---------- 90

F. Mechanical Properties ---------- 95
1. Hardness Level ---------- 95
2. Charpy V-Notch Toughness ---------- 99
3. Plane Strain Toughness ---------- 112

V. DISCUSSION ---------- 116

A. Correlation Between Solidification Substructures and As-Welded Morphology ---------- 116
1. Formation of Solidification structures ---------- 116
2. Formation of Austenite ---------- 123
3. Ferritic Transformation ---------- 124
4. A Modelling Morphological Changes ---------- 128

B. Influence of Alloying Elements ---------- 133
1. Formation of Equiaxed Dendrites ---------- 133
2. Formation of Grain-Boundary and Side-Plate ferrites ---------- 135
3. Formation of Acicular and Bainitic Ferrite ------- 143
4. Contribution of Ni Addition ---------- 144
5. Alloying Design of Ni-Mn-Mo Steel Filler Metal --- 153
6. Characteristic Parameter for Accicular Ferrite Study ---------- 154

C. Tubular Filler Metals ---------- 158
1. Advantages of Metal powder-cored Filler Metals --- 158
2. Weld Metal Oxygen Content ---------- 159

Page

D. Electroslag Thermal Transfer Pattern ---------- 161
1. Special Features of Heat Generation and Transfer in electroslag Weldments ---------- 161
2. Effects of Weld Pool Geometry on Heat Affected Zone Size ---------- 162
3. Heat Affected Zone Reduction ---------- 165

E. Fusion Line HAZ Toughness ---------- 167

VI. SUMMARY AND CONCLUSIONS ---------- 171

VII. REFERENCES ---------- 173

VIII. APPENDIX : Charpy V-Notch Toughness Test Data ------- 178

LIST OF FIGURES

Page

Figure 1. Schematic illustration of the consumable guide electroslag welding process ---------- 2

Figure 2. Typical appearance of electroslag weldments ---- 3

Figure 3. Typical grain microstructures in electroslag weld metal ---------- 6

Figure 4. Variation of solidification mode in weld metal - 14

Figure 5. Four types of grain morphologies of steel ES welds classified by Paton ---------- 22

Figure 6. Classification of ES weld metal Morphology for mild steels ---------- 23

Figure 7. Cross sectional photograph of TW8544 filler metal ---------- 32

Figure 8. Power supply of ES welding ---------- 35

Figure 9. Wire feeding device used for ESW ---------- 36

Figure 10. Copper cooling shoes for ESW ---------- 38

Figure 11. Configuration and size of consumable guide plates ---------- 40

Figure 12. Typical dendritic structures defined in this study ---------- 48

Figure 13. Typical renucleation events in the solidification structure in mild steel welds --- 49

Figure 14. Variation of dendrite inclination angle -------- 50

Figure 15. Correlation between the amount of cellular dendrites and the extent of the CCG zone ------- 54

Figure 16. Comparison between solidification structure and solid state microstructure ---------- 55

Figure 17. Effect of welding speed on primary dendrite arm spacing at the same heat input level ------- 57

Figure 18. Effect of heat input on primary dendrite arm spacing at the same welding current ---------- 58

Page

Figure 19. Effect of welding case on primary dendrite arm spacing ---------- 59

Figure 20. Distribution of dendrite arm spacing in case 4 welds ---------- 60

Figure 21. Correlation between the magnitude of form factor and the amount of coarse columnar grains - 62

Figure 22. Schematic expression of relationship between weld case, form factor, macro/microstructure ---- 63

Figure 23. correlation between weld current and coarse columnar grains ---------- 64

Figure 24. Correlation between welding and coarse columnar grains ---------- 65

Figure 25. Centerline cracking in case 3 ES weld ---------- 67

Figure 26. Radial hot cracking in case 4 ES weld ---------- 68

Figure 27. Distribution of inclusions near the fusion boundary ---------- 71

Figure 28. Distribution of inclusions in the columnar dendrite region ---------- 72

Figure 29. Distribution of inclusions near the weld center ---------- 73

Figure 30. Dendritic structures in the weld center -------- 75

Figure 31. Effect of Cr-Mo additions on the weld metal constituent volume fractions ---------- 76

Figure 32. Weld center microstructure of A36 weld containing 0.67% Cr and 0.24% Mo ---------- 78

Figure 33. Weld center microstructure of A36 weld containing 1.2% Cr and 0.40% Mo ---------- 79

Figure 34. Bainitic ferrite in A588 weld containing 1.2% Cr and 0.4% Mo ---------- 80

Figure 35. Effect of Ni-Mo additions on the constituent volume fractions of Mild steels ---------- 81

Page

Figure 36. Weld center microstructure of A36 weld containing 0.5% Ni and 0.1% Mo ---------- 82

Figure 37. Weld center microstructure of A36 weld containing 1.20% Ni and 0.22% Mo ---------- 83

Figure 38. Typical microstructure of A36 ES weld deposited by a) 25P wire, ---------- 85
b) AS521 wire, ---------- 86
c) TW8544 wire ---------- 87

Figure 39. Comparison of tubular and solid filler metals on weld heat input ---------- 88

Figure 40. Effect of tubular filler metal on dilution of welds ---------- 89

Figure 41. Effect of tubular filler metal on weld form factor ---------- 91

Figure 42. Typical HAZ morphology of A36 ES weld ---------- 92

Figure 43. HAZ size of various 50mm A36 and A588 ES welds - 93

Figure 44. HAZ size of various &6mm A36 and A588 welds ---- 94

Figure 45. Hardness traverse across A36 and A588 welds deposited by mild steel wire ---------- 96

Figure 46. Hardness traverse across 50mm A36 welds deposited by Cr-Mo and Ni-Mo wires ---------- 97

Figure 47. Hardness traverse across 50mm A588 welds deposited by Cr-Mo and Ni-Mo wires ---------- 98

Figure 48. Comparison of CVN toughness levels between weld metals containing Cr-Mo and Ni-Mo addition- 100

Figure 49. CVN toughness of 50mm thick A36 ES welds as a function of Ni content ---------- 101

Figure 50. CVN toughness of 50mm thick A588 ES welds as a function of Ni content ---------- 102

Figure 51. CVN transition curves for 50mm A36 ES weld tested at 1/2 thickness location ---------- 103

Figure 52. CVN transition curves for 50mm A36 ES weld tested at 1/4 thickness location ---------- 104

Page

Figure 53. CVN transition curves for 50mm A588 ES weld tested at 1/2 thickness location ---------- 105

Figure 54. CVN transition curves for 50mm A588 ES weld tested at 1/4 thickness location ---------- 106

Figure 55. CVN transition curves for 50mm A36 weld deposited by TW8544 wire ---------- 107

Figure 56. CVN transition curves for 50mm A588 weld deposited by TW8544 wire ---------- 108

Figure 57. CVN fracture surfaces of 50mm A588 ES welds deposited by different wires ---------- 110

Figure 58. Minimum test temperature at which the CVN toughness of 50mm A588 weldment is 20J --------- 111

Figure 59. CVN and K_1c toughness levels of 76mm A588 weld metal at -18°C ---------- 114

Figure 60. Nominal HAZ-1 K_1c toughness of 76mm A588 ES welds ---------- 115

Figure 61. Variation of weld pool shape with different form factors ---------- 117

Figure 62. Left corner of Fe-C phase diagram ---------- 119

Figure 63. Variation of morphology during solidification and subsequent transformation ---------- 121

Figure 64. Schematic CCT diagram of low alloy steel weld -- 126

Figure 65. Sequence of Morphological change in low carbon steel welds ---------- 130

Figure 66. Solidification and solid state microstructures near fusion boundary ---------- 132

Figure 67. Left corners of Fe-C, Fe-Cr, Fe-Ni and Fe-Mo phase diagram ---------- 134

Figure 68. Effects of alloy elements on austenite decomposition ---------- 137

Figure 69. Effects of alloy elements on the C-curve of low carbon steel ---------- 138

Page

Figure 70. Variation of carbon concentration during austenitic decomposition ---------- 139

Figure 71. Local carbon concentration around the growth frontier between austenite and ferrite --------- 142

Figure 72. Acicular ferrite-predominant A36 ES weld metals - 148

Figure 73. Hall-Petch plots for Fe-3.28 pct Ni alloy at room temperature and 77°K ---------- 152

Figure 74. Correlation between the number density of acicular ferrite plates and CVN toughness ------ 156

Figure 75. Correlation between alloy content and the number density of acicular ferrite plates ------ 157

Figure 76. Oxygen levels in A36 and A588 ES weld metals --- 160

Figure 77. Analysis of thermal transfer in the molten pool of ES welds ---------- 163

Figure 78. CVN impact toughness of HAZ as a function of the distance from the fusion line ---------- 168

LIST OF TABLES

Page

Table 1. Compositions of base metals, electrodes and guide plate materials ---------- 33

Table 2. Composition and basicity index of Hobart 201 flux ---------- 34

Table 3. Summary of welds related to this study ---------- 44

Table 4. The main compositions of some typical weld metals ---------- 50

Table 5. Correlation between percentage of cellular dendrites and coarse columnar grains in weld metals deposited by ESW ---------- 53

Table 6. Solidification defects in narrow-gap ES weld metals ---------- 69

Table 7. Diffusion coefficient of alloys in gamma-Fe ----- 147

Table 8. Variation of weld characteristics ---------- 164

Table 9. Weld characteristics of various ESW processes --- 166

ABSTRACT

Welding Metallurgy and Toughness Improvement
for Mild and Low-alloyed Electroslag Weldments

Dawei Yu, Ph. D.
Oregon Graduate Center, 1988

Supervising Professors: Dr. Jack H. Devletian
Dr. William E. Wood

Fundamental aspects of welding metallurgy and microstructural relationships controlling fracture toughness improvement were studied during a series of experimental electroslag (ES) welding practices for joining A36 and A588 base materials with 50mm and 76mm thickness.

The weld metal solidification study revealed a correlation between the solidification structure and the as-deposited weld metal morphology. Based on this finding, a model describing the formation sequence of ES weld metal has been suggested. The cellular dendritic to columnar dendritic transition and the kinetics of austenitic growth were the key factors affecting the products of solid state transformation in the weld metal. Upon cooling, the cellular dendritic region first transformed to coarse columnar austenite grains, followed by the formation of a high percentage of acicular ferrite. The columnar dendritic region first transformed to thin columnar austenite grains, followed by the formation of a high percentage of grain boundary and side plate ferrite. Variation in the form factor of the weld pool influenced the morphology of solidification structure and consequent as-welded microstructure.

The effect of alloying additions to the weld metal were in-

tensively studied in order to develop an effective method for upgrading the toughness of as-deposited weldments. Small additions of Cr, Mo and Ni tended to promote equiaxed dendritic growth at the weld center of mild steel welds, which substantially improved resistance to hot cracking. Also, the presence of Cr, Ni and Mo in the weld metal effectively inhibited the formation of grain boundary ferrite and side-plate ferrite. However, Cr-Mo additions resulted in a bainitic ferrite weld metal with low CVN toughness. While the Ni addition, which was a strong promoter of acicular ferrite formation, improved the weld metal toughness. Ni-Mn-Mo alloying in A36 and A588 steel ES welds created a fine acicular ferrite-predominant weld metal microstructure with impressively improved toughness relative to conventional practices.

The metal powder-cored tubular filler metal is recommended for ESW, because of its advantages over the solid filler metal such as, lower heat input, lower base metal dilution, higher deposition rate, higher form factor, and higher resistance to hot cracking. A specially designed Ni-Mn-Mo alloyed tubular filler metal exhibited not only dramatically upgraded CVN impact toughness in the ES deposits of both A36 and A588 steel joints, but increased the K1c toughness values of A588 steel weldments.

Detailed investigations revealed that electroslag welds have special thermal Transfer characteristics. Its large molten slag pool delivers a enormous heat to the surrounding base metal. The HAZ size in ES weldments was controlled by not only the total heat input but also the geometry of the molten weld pool.

It was also demonstrated that, for ES weldments, the measured

CVN impact toughness of coarse HAZ is a sensitive function of the distance from the fusion line.

I. INTRODUCTION

A. ELECTROSLAG WELDING TECHNIQUE AND ITS CURRENT STATUS

Many different welding processes have been developed for structural welding applications. For joining thick section components, electroslag welding (ESW) is the most cost-efficient and productive welding technique.

Electroslag welding is rather different from other fusion welding techniques. In ESW, no arc exists except during weld initiation. The heat of fusion is generated by the ohmic heating of a molten slag pool with a passage of electric current through it. This ohmic heating melts both the filler metal and the surfaces to be joined. The filler electrode is continuously fed into the slag pool and melts above the top of molten metal pool. The distance between the electrode tip and the molten metal pool, which depends upon the resistivity of molten slag and the setting of welding current and voltage, provides the resistance heating. Fig.1 is a schematic illustration of this process.

ESW is usually carried out only in the vertical or near vertical position. The edges of the parent metal and the contact surfaces of metal cooling shoes confine the contour of the weld deposit. No matter how thick the base metal is, the joining can always be completed in a single pass, and, once started, has to proceed to the completion without interruption. Fig. 2 displays the appearances of both as-welded and sectioned weldments.

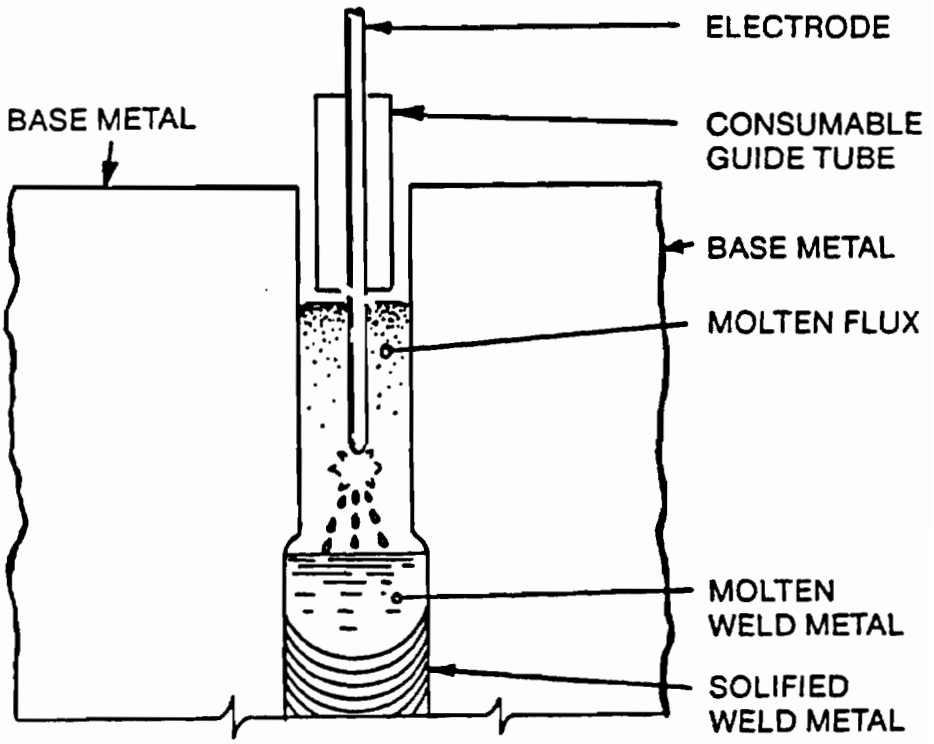

Fig. 1 Schematic illustration of the consumable guide electroslag welding process [1]

a) b)

Fig. 2 Typical appearance of electroslag weldments

a) as-welded joint; and b) macro-section.

This technique, in fact, was first invented by R. K. Hopkins in the United States in the 1930's [1]. But, the ESW process in its present form was first developed in the USSR in the early 1950's. Later, it was used in western Europe and introduced to the United States in the early 1960's. Around 1970, this technique began to gain acceptance as an alternative to submerged arc welding for fabricating heavy structural components. Its applications spread to the shipbuilding, heavy equipment manufacturing and field assembly fabrication.

There are two major variations of electroslag welding process: (1) the non-consumable guide (conventional) method, and (2) the consumable guide method. In the first method, a non-consumable contact tube is used to direct the filler electrode into the molten weld pool, and the entire welding head along with the cooling shoes must move up together at a predetermined rate consistent with the welding speed. The second method is more often used in industry, in which, the guide tube constantly melts into the weld pool thereby increasing the deposition rate. Also, the guide tube carries a portion of the current, which allows the usage of high welding current. In addition, no feeding head movement is needed during a consumable guide process. Welds of length up to 30 feet or more can be made in the case of no electrode oscillation. [1].

The electroslag welding process has many advantages over other welding processes, such as: one pass operation, no pre-heating, high deposition rate, low workmanship requirement, less surface preparation and less thermal distortion. However, it also leads to a number of special problems, these being additional to those encountered in other

welding situations. The most serious problem of ES weldments is their low toughness in the as-deposited state, since excessive heat input and slow welding speeds result in overheated weld metals and substantial grain growth in the heat affected zones (HAZ). This often restricted its use in many cases, for example, bridge constructions, ship assemblies, and other dynamically-loaded structures, where a postweld heat treatment cannot be conducted. Although there are few known cases of failure directly involving electroslag welded joints, low toughness and coarse grained microstructure do infer caution and must be upgraded before the acceptance of more practical applications.

A number of research projects have been devoted to overcoming the low toughness problem in steel ES weldments [2-5]. For the past several years, in a project conducted at the Oregon Graduate Center and sponsored by U.S. DOT /Federal Highway Administration, a narrow-gap ESW technique [6] has been developed for joining 2 inch (50mm) and 3 inch (76mm)-thick A36 and A588 plates. As compared with the traditional standard gap ESW, the narrow gap method (1) eliminated the need for electrode oscillation, (2) established a smaller weld pool and HAZ, (3) lowered power input and penetration, and (4) increased the deposition rate and weld efficiency. Thus, with optimized weld parameters, the CVN impact toughness and resistance to hot cracking were improved.

In general, the morphology of as-deposited mild steel weld metal shows two zones of grain structure (Fig.3): thin columnar grains (TCG) around the weld center, and coarse columnar grains (CCG) near the fusion interface. The former is composed largely of grain boundary ferrite and side-plate ferrite, which cannot withstand cleavage crack

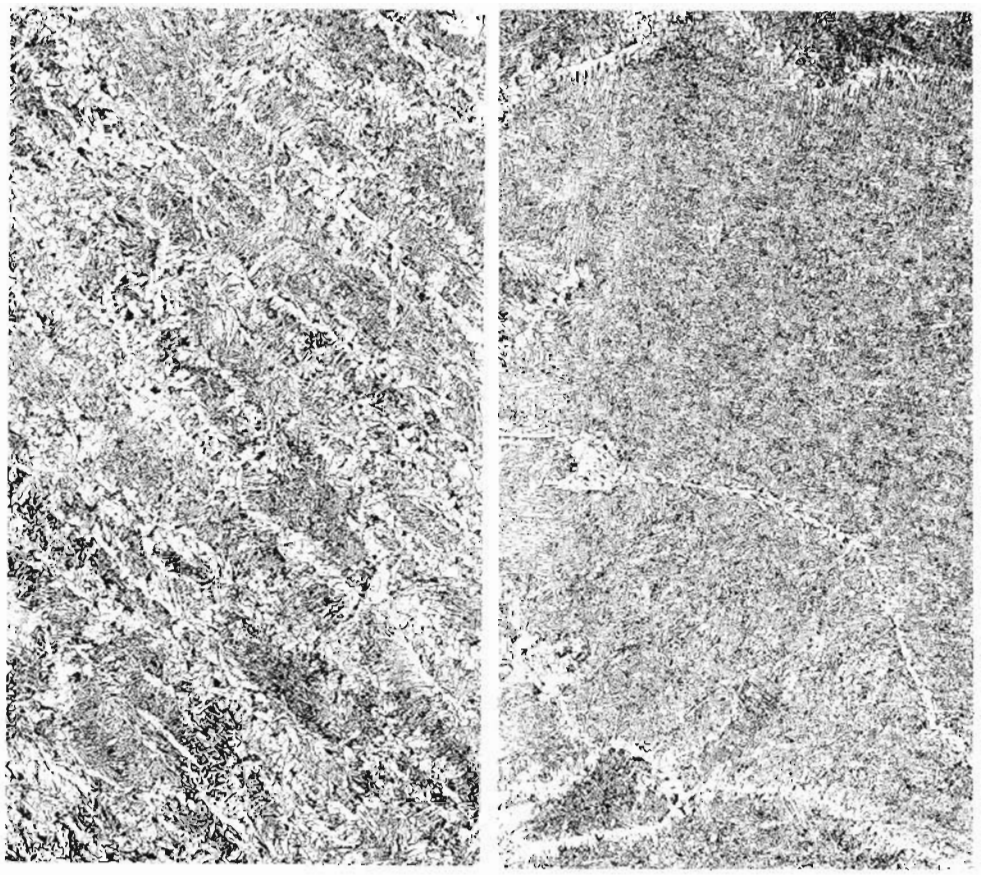

a) b)

Fig. 3 Typical microstructures of a) thin columnar grain and b) coarse columnar grain in electroslag weld metal

propagation, and the latter contains a predominantly acicular ferrite substructure which is quite resistant to cleavage.

Acicular ferrite, owing to its great contribution to toughness, is the most sought-after constituent for the as-welded low alloy steel microstructure. In ESW, the adjustment of welding parameters can increase the proportion of the acicular ferrite-rich CCG, but it does not substantially change the substructure of the remaining TCG. Alloying is thought to be a more effective way of developing a fully acicular ferrite weld structure [4,5,7]. However, as pointed by Grong and Matlock recently [8], even if a few alloy elements were known to promote the formation of acicular ferrite, surprisingly, little is fully understood about their role in weld metal transformation kinetics. Thus, during this project, work was concentrated on the broad area of the relationship between the alloying addition, the weld metal microstructure and the mechanical properties. Special attention was paid to both theoretical and practical aspects of choosing the most effective alloying combination. [7].

Later, a low alloy steel tubular electrode (TW8544) was designed and applied to the narrow gap consumable guide ESW process at OGC. Impressive results have been obtained in upgrading the microstructure and toughness of A36 and A588 electroslag weldments [9].

B. STATEMENT OF PURPOSE

In view of the potential importance of upgrading the microstructure and toughness of steel electroslag weldments, the major objectives of this research work were oriented to the following subjects:

1. establishing the correlation between the solidification structures and the as-deposited morphology of electroslag weld metals,
2. investigating the influence of alloying elements on the weld metal phase transformations, especially in term of the acicular ferrite formation,
3. determining the role of metal powder-cored filler metals on changing weld pool characteristics and welding heat input,
4. evaluating the improvement in toughness resulting from the low alloy tubular wire deposition,
5. studying the thermal transfer pattern of electroslag weldments and its effects on the heat affected zone.

Such knowledge is important in establishing a more reliable and effective electroslag welding technique, also for broadening the general understanding of welding metallurgy.

II. BACKGROUND REVIEW

A. PROPERTY REQUIREMENT AND PROCESS IMPROVEMENT IN ESW

High heat input and a prolonged thermal cycle result in coarse grained structures in both the electroslag weld metal and the heat affected zone. In the weld metal, the macrostructure of grains is quite anisotropic and non-homogeneous. Mechanical properties vary with locations and directions. This type of weld can not be considered acceptable when minimum notch toughness requirements are specified.

Paton first indicated the low notch toughness problems in ES welds in the early 1960's [10]. Later, this was also found in several research projects conducted by the Welding Institute [11-13]. In 1975, Shackleton [14] pointed out that whenever the electroslag welding process was used, the only problem area was always related to the weldment toughness. He also reported some exceptions to his tests [15]. For example, with a low Si (C-Mn type) filler metal, 44J Charpy energy was achieved at 0°C from some of the ES weld metals deposited on 50 mm-thick C-Mn mild steels. In the United states, since 1970, a few research projects have concentrated on this area [3, 16], and confirmed that the impact energy level of the central zone in ES welds is lower than that of the surrounding weld metal, and even lower than that of the base metal. In the Michigan DOT's research, J.Culp [17] reported that the ES weld metal microstructure was much more detrimental in the high strength low alloy steel A588 than it was in the construction grade of low carbon steel A36. He also noticed that the toughness of the HAZ was partially dependent on the toughness of the base metal itself. If base metals could meet the specified minimum toughness value,

the weldments would be much more reliable in service. Some Charpy impact toughness evaluations of ES weldments also revealed that (1) both the weld center and the coarse grained HAZ were often of very low toughness [18, 19], and (2) the coarse columnar zone was tougher than the weld center zone made up of thin columnar grains [20]. The second fact actually challenged the majority opinion that the coarse grain structure found in electroslag welds was indicative of a high susceptibility to brittle fracture.

A few codes were prepared to document the qualification of ES welds. For example, according to the AWS Code D 1.1 [21], in order to ensure the safety of electroslag weldments, the minimum impact toughness requirement for butt welds was 20J(15 ft-lb) at 0°F (-17.7°C). For tension members in bridge applications, more details were specified. As discussed by the NCH Report 201 [22], the notch toughness requirements for both the weld metal and the HAZ should be made mandatory. The average value of tested specimens must meet the minimum current AASHTO requirement for the steel being welded, such as, for A36 steel in the geographic Zone 2 service, the HAZ toughness has to meet 27J (20 ft-lb) at 5°C (40°F).

Since the Charpy toughness evaluation specimens sampled only a portion of the real welds, several investigators believed that it does not rate welds in their true order [23, 24, 25]. Shackleton, in 1981 [15], reported the opinion of the Welding Institute that the benefits could be gained by basing a toughness assessment on fracture mechanics parameters(CTOD) rather than on the Charpy test, which enabled toughness to be analyzed in terms of the condition existed, besides achiev-

ing more realistic toughness measurements. Based on the studies of Michigan DOT research projects, J. Culp suggested [19] that a complete understanding of the fracture toughness characteristics of ES welds had to be gained before a fracture-safe design could be achieved. Sovak [26] reported some fracture toughness data from the non-consumable guide ESW of A36 and A588 steels using subsized specimens, and considered that those data might underestimate the actual fracture resistance of full-sized weldments. Decreasing heat input was one approach to improve the toughness of ES weldments [10,23]. The adjustment of welding parameters (current, voltage, joint gap and guide plate /tube design) could directly vary the value of total heat input [6]. But, the degree of variation was limited by the susceptibility to hot cracking and lack of fusion [27]. Other methods have been also reported to decrease weld heat input, among them were feeding additional filler wires, metallic powders, chopped wires and lump filler metals into the weld pool [4, 5, 28]. However, problems such as macro-chemical heterogeneity and incomplete fusion limited these approaches. All the methods mentioned above only reduced the proportion of thin columnar grains in the weld metal, but did not change its substructure substantially [27, 28].

In 1978, the Materials Science and Engineering Department of the Oregon Graduate Center started a series of fundamental studies in the electroslag welding technique. Under the FHWA contract FH-11-9612, S. Venkataraman et.al. investigated the effects of various parameters on the welding consistency and quality in A588 steel ES welds. They indicated that a proper slag depth was required to control the process stability and the weld metal microstructure, and the winged guide

enabled low welding voltage (34-36 V) with complete penetration whereas the standard half inch diameter cylindrical guide tube required a minimum of 42V to achieve the side wall fusion. This winged guide design eliminated the need for electrode oscillations during welding thicker sections and minimized the errors involved in electrode positioning. They reduced the joint gap of 51 and 76 mm (2 and 3 inch) thick welds, from 32 mm (1.25 inch), standardgap, to 19 mm (0.75 inch), narrow-gap, and claimed that the high current /narrow gap /winged guide technique resulted in a 50% reduction in heat input and a 3-fold reduction in the welding time. They also found that the Charpy toughness values of their welds were 15 and 82 Joule (11 and 61 ft-lb) at -18°C (0°F) at the mid-thickness/weld centerline and coarse columnar grain zones respectively [29].

B. FORMATION OF WELD MORPHOLOGY

By far, most efforts in solving the as-welded toughness problem has been concentrated on the microstructural improvement. As known, the formation of the as-deposited microstructure of steel welds frequently experiences a series of complicated phase transformations, and many factors can influence these transformations. Obviously, substantial microstructural improvement is unlikely to be made without paying careful attention to formation mechanisms. Therefore, a better understanding of the formation of the various constituents in the weld metal should be beneficial in designing measures for microstructural improvements.

1. SOLIDIFICATION STRUCTURE OF WELD METAL

The understanding of the fundamental aspects of the solidification of cast metals has increased substantially. However, it was not directed at the study of weld pool solidification until the last 20 year and only a few systematic studies on the solidification structures of steel welds have been reported.

The fact that no nucleation event is necessary to initiate weld pool solidification was first recognized by Savage and his coworkers[30, 31]. They concluded from the continuity of grains across the fusion boundary that solidification began by the 'epitaxial' growth on the parent plate, and confirmed that grains generated in the weld metal had the same crystallographic orientation as the immediately continuous parent-plate grains across the fusion boundary. Then, Savage et al. [31], Matsuda et al.[32], and Lop et al.[33] indicated that the width of weld metal grain at the fusion boundary was determined by the width of that grain in the HAZ acting as the growth substrate. The initial growth of partially melted grains in the base metal was followed by a period of columnar grain development. Each individual columnar grain exhibited a substructure consisting of a parallel array of dendrites or cells. However, for mild steel weld metals, this was masked by the austenite to ferrite transformation.

It was also found that the stability of the solidification front was controlled by both the alloying level and the extent of constitutional supercooling ahead of the advancing interface [34]. Savage extended a few other researchers' work and schematically expressed this relationship as Figure 4, where R is the growth rate and G is

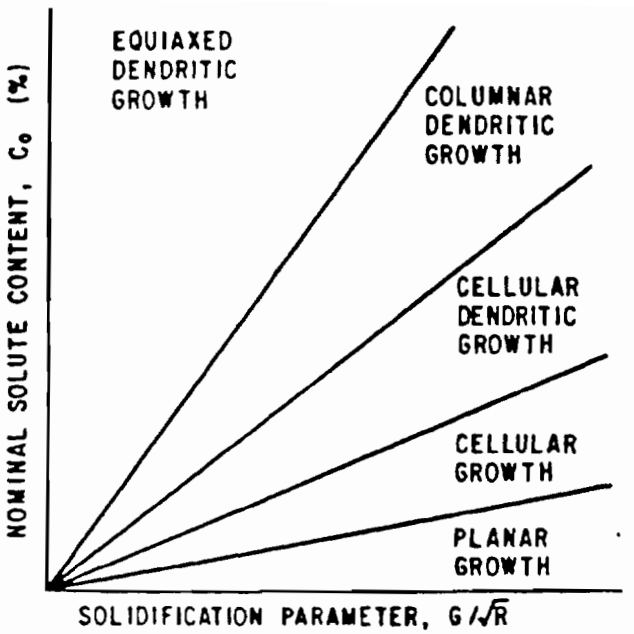

Fig. 4 Variation of solidification mode in weld metal [31]

the thermal gradient in the weld pool, and G/R is called 'the solidification parameter' representing the degree of constitutional supercooling [31]. With distance from the fusion line, the solidification substructure varies from cellular dendritic to columnar dendritic, since the temperature gradient in the growth direction decreases, and the growth rate increases [35,36]. The rapid solidification rate in most fusion welds results in a fine scale of solidification substructures. Brown [37, 38] predicted theoretically the relationship between the dendrite arm spacing and the arc energy or heat input per unit length of weld

$$L \propto (q/V)^{1/2} \qquad ---(1)$$

where q is the arc power and V is the arc travel speed.

As pointed out by Davies et al.[39], natural transition from columnar dendritic to equiaxed dendritic growth is comparatively rare in SAW or GMAW (but not applicable to ESW) during normal weld-pool solidifications. The thermal condition in the melt is so severe, during welding, that the nuclei survival is very limited unless either the mechanisms promoting the nuclei generation are particular effective, which is normally only the case when steps are specially taken to obtain the equiaxed growth, or the welding condition is such as to produce a high level of undercooling in the pool.

A progressive decrease in the dendrite arm spacing between the fusion boundary and the weld centerline can be observed in individual welds. It has been suggested [40] that this might be due to the increased solute segregation at the centerline reducing the rate of dendrite coarsening. The effect of solute content upon the dendrite

arm spacing is not clearly defined in the technical literature yet. As mentioned by Davis et al. [39], "little quantitative information is available on the form which solute segregation may take in a weld, probably because of the very fine nature of the solidification substructure which often precludes meaningful electron probe microanalysis".

Nevertheless, some researchers [41, 42] found that the basic mechanism of solute segregation in the weld solidification appeared to be the same as in ingot solidification except for epitaxial growth. Microsegregation was more pronounced in the inter-dendritic regions than in the cell boundaries. The increase of cooling rate by decreasing the energy input reduced the interdendritic solute segregation, while at the same time, raised the solute content at the center of the dendrite arms [43]. In addition, segregation at grain boundaries was also identified [41, 42] to be greater than that encountered within the substructure composing the grains. Thus, the solidification mode does control both the solidified grain development and the associated segregation. It is likely not only an important factor influencing the consequent transformation products, but also a significant factor influencing the deposit properties and behaviors, for example the hot cracking problem.

2. AUSTENITE DECOMPOSITION PRODUCTS IN THE WELD METAL

During the austenite decomposition at temperature below the Ac_3 line of Fe-C phase diagram, a variety of microstructures can be developed in mild and low-alloy steel weld metals. Several systems have been introduced throughout the years for the classification of those

austenite decomposition products, with each system reflecting individual researcher's views and discretions. This controversy in terminology sometimes causes confusion. Using the most recent IIW recommendation, which is based on the scheme originally proposed by Abson and Dolby [44], the products of austenite decomposition include:

(i) grain boundary ferrite,

(ii) polygonal ferrite,

(iii) Widmanstatten ferrite side-plate,

(iv) acicular ferrite,

(v) upper bainite, and

(vi) lower bainite and martensite.

The above constituents are basically arranged in a decreasing order of transformation temperature. In the case of mild steel weld metal, upper bainite is often bainitic ferrite and usually neither lower bainite nor martensite are formed.

Below the Ac_3 temperature, ferrite will initially nucleate at those sites providing the lowest energy barriers, such as austenite grain corners and boundaries. Then, ferrite grows with parabolic kinetics into austenite behind a planar incoherent front [45], leading to the formation of grain boundary ferrite in the temperature range between 1000°C to 700°C [46]. The diffusion of carbon atoms governs the growth of grain boundary ferrite.

With an increasing degree of undercooling, the re-distribution of carbon is insufficient to maintain a planar growth front. The further growth of ferrite can only take place by a lateral movement of ledges along low energy interfaces [47]. This implies a Kurdjumov-Sachs

orientation relationship [48] between austenite and ferrite, i.e. $(111)_\gamma$ parallel with $(110)_\alpha$ and $[011]_\gamma$ parallel to $[111]_\alpha$, which is a characteristic feature of Widmanstatten ferrite structure [49]. The formation of Widmanstatten ferrite is also accompanied by some change in the shape of the transformed region; the shape change resulting from a single wedge of side-plate consists of two adjacent and opposing invariant-plane strain deformations [50]. Those ferrite side-plates, once nucleated, grow very rapidly under the prevailing condition, since those interstitial carbon atoms could be redistributed to the sides of the advancing interface without affecting the shape change or the displacive character of the transformation [50]. The formation temperature of ferrite side-plates is about 650 to 750°C [46].

Simultaneously with or immediately after the formation of ferrite side-plates at the austenitic grain boundaries, acicular ferrite may start to nucleate intragranularly at inclusions [49]. Acicular ferrite consists of relatively fine grained and spindle-like ferrite plates. These individual ferrite plates are separated by high angle grain boundaries [51]. The formation of acicular ferrite involves a lot of factors, such as the oxygen content and the alloy level in the weld metal, and the cooling rate of weldments. The exact mechanism by which acicular ferrite forms within austenite has not been fully elucidated.

Over the last ten years most investigations have pointed out that the inclusions in the weld metal play a very important part in the formation of acicular ferrite. Inclusions commonly found in weldments are either exogenous or indigenous, depending on their origin. The first type mainly arises from the entrapment of welding slags, while

indigenous inclusions result from deoxidation reactions. As the temperature falls and oxygen becomes less soluble in steels, the reaction between oxygen and deoxidants inside the weld pool form some globules of immiscible liquid or solid which thereby becoming trapped in the solidified weld metals [51].

The volume fraction as well as the total number of inclusions in steel weld metals is considerably higher than for normal cast steel products. Also, the inclusions are significantly smaller in dimension and more finely dispersed [49]. The role of non-metallic inclusions in the nucleation of acicular ferrite was first demonstrated by Abson [52] and Cochrane [53] and has been observed and confirmed by other workers. Due to the large difference in the thermal expansion coefficient between the austenite matrix and inclusions, a textural (or tessellated) stress field arises around inclusions, and fine inclusions inside the undercooled austenitic grain can become energetically-favorable nucleation sites for acicular ferrite. Calculations by R. Rick et. al [54] provided theoretical support for this phenomenon. The magnitude of difference in the thermal expansion coefficient can be over one order [55], which, during cooling, might aid the acicular ferrite nucleation by forming sufficient dislocations [49, 56]. Observations [54] also confirmed that inclusions could act as multiple nucleation sites for some acicular ferrite laths which, in turn, sympathetically nucleated more laths. A certain range of weld metal oxygen content, 200 to 400 ppm, has been found to promote the formation of acicular ferrite [56]. In low oxygen (< 150 ppm) deposits, there are too few inclusions to provide energetically favorable sites for the intragranular ferritic

nucleation. While, in high oxygen (~600 ppm) deposits, more inclusions lodge near austenite grain boundaries, which encourage the early ferrite nucleation in these regions and thereby discouraging the formation of acicular ferrite [56]. Studies have revealed that the acicular ferrite nucleation begin at 600 to 650°C [46]. Since the acicular ferrite laths normally grow until impingement occurs on neighboring laths, the final size of these laths will largely depend on the average spacing between the inclusions inside austenite grains.

In low carbon steel welds, as temperature continuously falls, carbon will further enrich the remaining austenite, resulting in the formation of bainitic ferrite. Bainitic ferrite occurs at a more severe undercooling relative to Widmanstatten ferrite and acicular ferrite, and consists of much finer platelets of ferrite.

Few studies have contributed to the nucleation of bainitic ferrite in weld deposits, but this nucleation is thought to be isothermal and should involve the partitioning of carbon during the nucleation event. Some evidence leads to the suggestion that the activation energy for bainitic ferrite nucleation is directly proportional to the chemical free energy change accompanying nucleation. This could be interpreted to imply that the bainitic nucleation is displacive in character [50].

3. MORPHOLOGY OF ELECTROSLAG WELD METAL

The morphology of steel weld metals deposited with ESW was first summarized and classified by Paton [10]. He classified four types of grain structures for electroslag weldments, as shown in Fig. 5:

* Type I. There are an outer zone of coarse columnar crystals and an interior zone of thin, elongated columnar crystals.

* Type II. There is, in addition to the coarse and fine columnar crystals of Type I, a zone of coarse equiaxed crystals in the very center of the weld.

* Type III. The weld structure consists of only coarse columnar crystals throughout the cross section.

* Type IV. The weld structure consists of only fine columnar crystals.

During this DOT-sponsored project, a new classification of ES weld metal structures has been developed. At first, the classification was based on four cases of mild steel weld metal structure which resulted from alterations in welding parameters such as the welding current, voltage and heat input, as shown in Fig.6 [27]. Later, it was further developed as a five-type system, taking into considering the effect of alloy and oxygen content as well [57]. The new classification more clearly and logically demonstrates morphological changes in macrostructure, solidification substructure and as-deposited microstructure, and their inter-relation.

Type 1

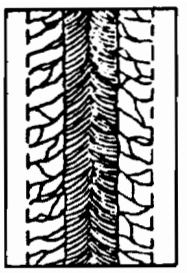

Type 2

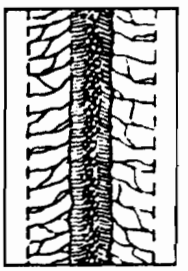

Type 3

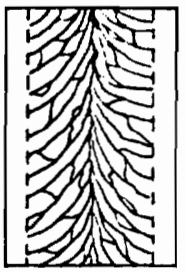

Type 4

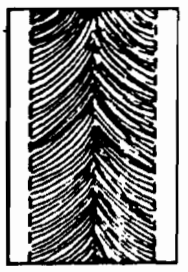

Fig. 5. Four types of grain morphologies of steel ES welds classified by Paton [10]

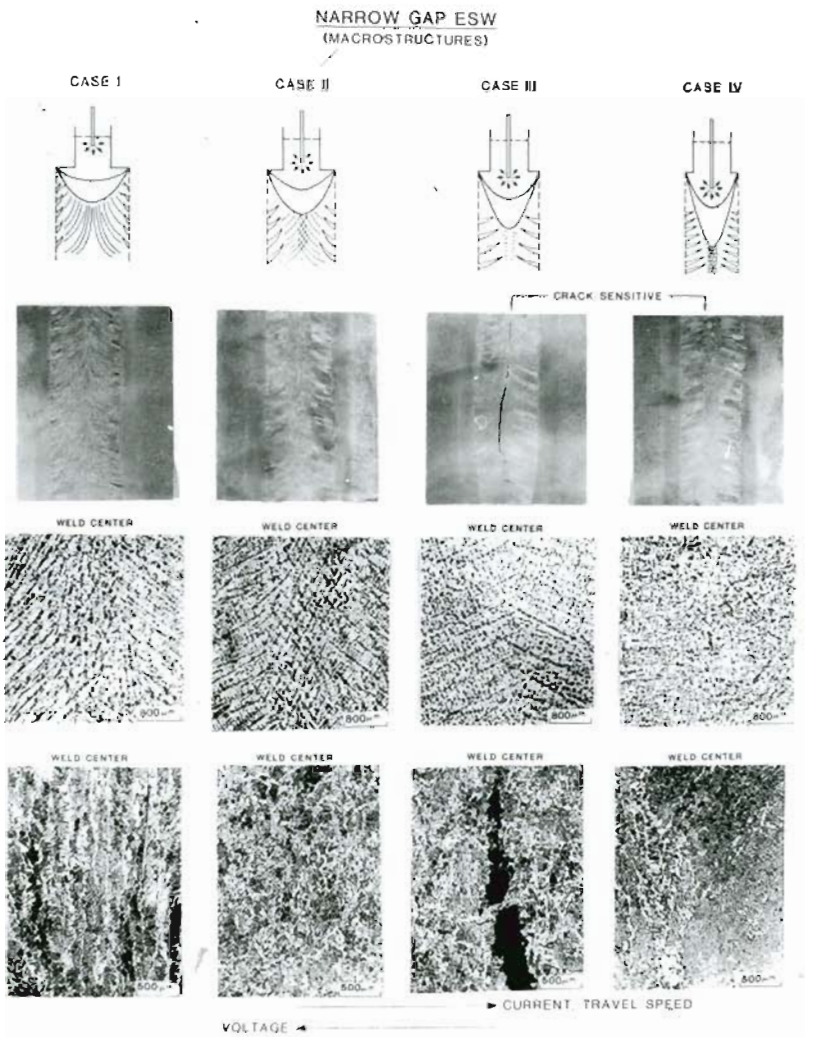

Fig. 6 Classification of ES weld metal morphology for mild steels [6]

C. INFLUENCE OF ALLOYING ADDITIONS ON MICROSTRUCTURE AND PROPERTIES

In fabricating heavy steel structures, those large heat input welding processes such as submerged arc welding, electroslag welding are frequently employed for increased efficiency. Weldment toughness is of great practical importance from the viewpoint of structure safety, because the as-welded fusion zone can often be very brittle.

In order to improve toughness in the fusion zone, two methods were used. One was to produce a lower bainitic structure in the fusion zone by adding such alloying elements as C, Mn, Cr and Mo, which had a strong tendency to increase hardenability [58]. However, if this was applied to mild steels, the susceptibility to cracking under high heat input conditions increased[59]. The second method consisted of stimulating the ferrite transformations and developing a fine ferrite-pearlite structure [60]. Later, the acicular ferrite structure became the first choice for improving the toughness of mild steel weld metals, due to its high cleavage resistance [61].

During the past ten years, alloying the weld metal has prevailed in many different welding processes. The addition of alloying elements usually serve two purposes: (1) to raise the strength level by solid solution or precipitation strengthening, and (2) to control the microstructure through modifications of the nucleation and growth rate of proeutectoid ferrite.

Alloying elements can be added into the weld metal by several means. In the Soviet Union, additional filler wires, chopped wires,

lump filler metals have been tried [5, 28]. But, problems such as macrochemical heterogeneity and incomplete fusion limited these approaches. In West Germany, Eichhorn reported a successful method: in addition to the current-bearing wire electrode, some alloyed metal powder was supplied without current [4]. In the U.S., Reynolds also claimed the use of supplemental metal powder additions [62]. But, an additional magnetic device was required for those cases. Thus, the easiest way to obtain the required alloying elements in the weld metal is to introduce them delibrately through the filler wire with a designed chemical composition.

The effects of alloying elements on weld microstructures and properties have been studied by many researchers. Here, only the influence of C, Mn, Ni, Cr, Mo and Si will be stressed. Although most references involved only common fusion welding processes other than ESW, their general principles are still applicable to this study.

CARBON

In general, carbon increases the strength and decreases the notch toughness of weld metals with equivalent microstructures. A number of investigators have found that the Charpy impact toughness decreased as the carbon content increased from 0.05 to 0.10% [63] and 0.1 to 0.2% [64] in submerged arc deposits. But, low toughness has also been found at low carbon contents too and attributed to the coarsening of the microstructure. Kotecki [64] reported that the optimum carbon content is 0.07 to 0.08%, and Devillers [55] claimed 0.08 to 0.10% (depending on the toughness criterion used) for their submerged

arc welds. Therefore, as a Charpy impact toughness concern, it seems beneficial to maintain the carbon level at least as low as 0.10%, or possibly lower. However, another problem has to be recognized. The use of low carbon electrodes might, in the highly diluted regions, result in carbon levels below those of the parent metals. Thus, difference in carbon content between the low and high dilution regions certainly increases the complexity of the task of obtaining high toughness in both regions [56].

MANGANESE

Mn increases the yield/tensile strengths and elongation when added to a weld metal containing 0.1 to 0.2% carbon [66]. Mn has no effect on the toughness of pure iron weld metal [66]. But this result was academic since Mn generally had a beneficial influence on low strength weld metals containing carbon. In the weld metal containing 0.1% carbon, Mn, up to 2.2%, decreased the ductile-brittle transition temperature, as claimed by Moll and Stout [66]. Widgery also reported that Mn helped to promote an acicular microstructure having good cleavage resistance in low strength weld metals [67, 68].

Mn lowers the transformation temperature of austenite to ferrite. Balanced additions of Mn are normally also found to improve toughness, because of the increased proportions of acicular ferrite in the weld deposit in combination with a general refinement of the microstructure [68]. Mn makes other contributions as well. It deoxidizes the weld pool, reduces the number of inclusions if increased by greater amounts than the Si content, and ties up S to aid crack resistance [69,

70].

The optimum Mn levels for the Charpy and the CTOD toughness of shield metal arc deposits were reported to be about 1.4% [12, 14] and 1.7% [71, 72]. These results were often influenced by the applied alloying and deoxidation practices. Broadly similar efforts to improve toughness and microstructure have been achieved in submerged arc deposits and gas shield deposits.

SILICON

It has been well established that high levels of silicon (> 5%) are generally detrimental to the weld metal toughness. However, a continuous lowering of silicon does not necessarily give a continuous improvement in toughness. For commercial electrodes, the optimum weld metal Si content usually lays in the range of 0.3 to 0.5%, with low levels of Si being detrimental both to the Charpy toughness and to the operating characteristics of the electrode [73]. Since the primary function of Si in weld metal is the deoxidation of the weld pool, the Si content has to be considered carefully to keep a certain amount of oxide inclusions which are thought to favor the acicular ferrite transformation formation. Unfortunately, the effects of Si on the formation of martensite and/or austenite microphases in combination with a general increase in the weld strength level, often over-shadows the apparent beneficial effects of Si on the development of an acicular ferrite microstructure [74, 75, 76]. The practical optimum Si content in weld metals, depending on the Mn%, could be 0.15%to 0.35% for submerged arc welds [77, 78].

CHROMIUM

In general, Cr kinetically suppresses and delays the austenite decomposition transformation [79]. And, it is also claimed that the precipitation of Cr-carbides could restrict the formation of proeutectoid ferrite at the prior austenite grain boundaries by either pinning or dragging effects [80].

Cr has a moderate strengthening effect on low strength steels, as evidenced by weld hardness measurements [76, 81]. The influence of Cr on weld metal toughness is not straight forward. Cr additions up to 0.4% in SMA weld metals increased the Charpy transition temperature according to Sakaki's report [74]. Beyond 0.4% Cr, the transition temperature decreased. Ohwa [82] found that Cr increased the transition temperature for the covered electrode weld metals. A similar trend was shown by other investigators for submerged arc weld metals and gas metal arc deposits. Sagan and Compbell reported the transition temperature of SMA deposits to increase with combined additions of Cr and Mo [83].

For the weld metal of pressure vessel steel joints, Cr is a moderate strengthener too. The Cr content in those welds can reach 0.5%, or in some cases, up to 1.0%, without seriously impairing as-deposited toughness. But, if greater than 1.0% Cr, significant reductions in toughness result. Of course, changes in toughness with Cr additions also depend on the other elements presented in welds and factors such as welding conditions [68].

NICKEL

Ni has a mild strengthening effect when being added to low strength weld metals. Henschkel estimated a yield strength increase in weld metals, at the rate of about 21 to 25 MPa for one percent Ni addition, depending upon the amount of the other elements in the weld metal [84]. Sakaki found that Ni decreased the transition temperature when added to weld metals in amounts up to 15% [74]. A slight decrease in the transition temperature was also claimed for the submerged arc weld metal when Ni was added up to 2.4% [81]. Ohwa [82] and Sagan [83] reported the beneficial effect of Ni in increasing the toughness of SMA weld metals. Some data presented by Morigaki indicated that Ni reduced the scattering in the Charpy data of weld metals [85]. Bosward [86] showed a comparison of the Charpy toughness of AWS E8018-c1, E8016 -c2, and E8018-c2 deposits at different arc energy levels, which illustrated the beneficial effect of Ni content especially at the temperatures of -50 and -70°C. The increase in toughness was attributed to the formation of a great proportion of acicular ferrite. But, one report [85] also showed that there was a strong interaction between Mn and Ni, and the optimum Ni content must ensure that the gamma to alpha transformation occurred within a certain restricted range of temperature.

MOLYBDENUM

In low strength weld metals, Mo suppresses the fraction of proeutectoid ferrite, but increases the amount of carbides. Thus, it might be the interaction of these two factors which produces changes in toughness of weld metals. From a practical viewpoint, the advantage

of Mo should lie in its ability to strengthen the weld metal without significant reductions in the notch toughness.

Sakaki [74] showed that up to 0.2% Mo in the weld metal lowered the transition temperature. Judson and Mckeown [88] found 0.1% Mo to be the optimum for the Charpy toughness in the range of -15 to -50°C. Hill and Levine found that an addition of 0.18% Mo reduced the proportion of grain boundary ferrite and increased the Charpy toughness, including the upper shelf toughness. And, with higher levels in welds, Mo had a deleterious effect on the microstructure [89]. Undoubtedly, the optimum Mo level is also influenced by the flux type, input energy and other elements present, and this was certainly true with respect to Ti [77]. Vankataramen [29] reported that the elemental Mo addition in the A588 ES weld metal eliminated the formation of proeutectoid ferrite film bordering the prior austenite grain boundaries. But, both excessive hardness increase and severe alloy segregation were observed. He also claimed that the Cr-Mo addition created a bainitic ferrite morphology, and the mid-thickness weld centerline and the coarse columnar grain zone showed 22 and 26J (17 and 19 ft-lb) Charpy energy respectively with a high current/narrow-gap/winged guide technique.

The references given above provided a solid base for the study of alloying additions on the weld metal structure formed during ESW of mild steels. However, it should be borne in mind that the influence of each individual element on the resulting microstructure and toughness is often very difficult to assess because of a number of interacting and complex factors involved.

III. EXPERIMENTAL PROCEDURES

A. MATERIALS

1. BASE MATERIALS AND FILLER METALS

This welding study was conducted on ASTM A36 and A588 steel plates having thickness of 50 mm (2 in) and 76 mm (3 in). A36 is a typical low carbon structural steel, while A588, containing small amounts of Cr and Ni, belongs to the low carbon HSLA (high strength/ low alloy) steel category. All the 50mm-thick materials were supplied by the Oregon Steel Mill (a division of Gilmore Steel), while all the 76mm-thick materials were supplied by U.S. Steel.

Various filler metals, including the solid and tubular filler metals, were all supplied in the form of 2.4 mm (3/32 in) diameter wires. The commercial electrode HP-25 wire has a composition matching that of A36 steel, and the Linde WS wire matching A588 steel. Low alloyed filler metals, Page AS521 and Airco AX-90, are also commercial steel electrodes which are alloyed with small amounts of Cr-Mo-Mn and Ni-Mo-Mn elements respectively. These four filler metals are all solid wires. During this study, a new filler metal was designed to improve the microstructure and mechanical properties of low carbon steel ES weldments. It was fabricated by Stoody Company and designated as: TW8544. The TW8544 filler metal is distinguishable by its metal powder cored tubular feature. The powder/shell ratio is about 3:7. Both the inner powder and the outside shell share an identical low Ni-Mo-Mn alloyed steel composition. Fig.7 is a photograph of the cross section of this tubular wire.

The consumable guides used in this study, including tubes

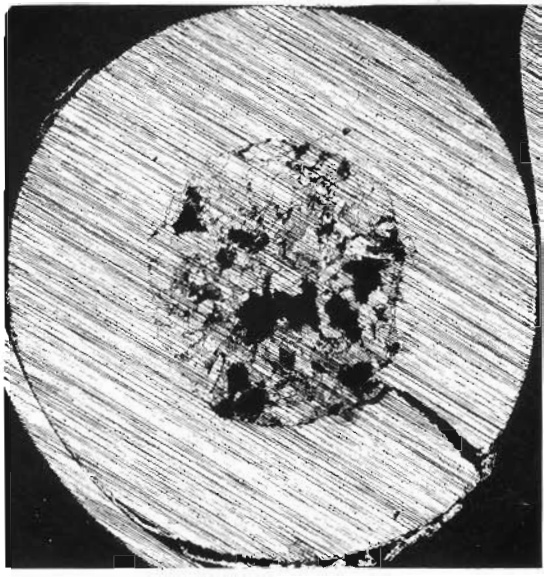

Fig. 7 Cross-sectional photograph of TW8544 filler metal

and welded rectangular plates, were made out of 1010 mild steel.

Table 1 summarizes the chemical compositions of the above materials.

Table 1 The Chemical Compositions of Materials (wt%)

Material	C	Mn	Si	Cr	Ni	Mo	Cu	S	P	Ti	Al
A36	0.17	0.92	0.20	0.02	0.10	--	0.20	0.02	0.01	--	0.024
A588	0.18	1.20	0.37	0.56	0.16	--	0.32	0.02	0.01	--	0.009
Hobart-25p	0.11	1.12	0.50	--	--	--	0.32	0.02	0.02	--	0.004
Linde-WS	0.09	0.50	0.30	0.55	0.50	--	0.30	0.03	0.02	--	0.011
Airco-AX90	0.08	1.40	0.46	0.06	2.10	0.40	--	0.02	0.02	0.007	0.003
TW8544 *	0.03	1.20	0.45	--	2.40	0.45	--	0.02	0.02	0.011	0.007
1010	0.10	0.45	--	--	--	--	--	0.05	0.04	--	0.030
	[Balance: Fe}							(max)	(max)		

* Designed by authors and manufactured by Stoody Company

2. FLUX

All welds were made with a neutral Hobart 201 commercial flux. Hobart 201 is generally used as a running flux for the electroslag welding process, but, in this investigation, it was used for both starting and running. The composition and basicity index of the 201 flux is given in Table 2.

Table 2. Composition And Basicity Index of Hobart 201 Flux

Compond	Amount (wt%)
CaO	12.20
MnO	22.46
SiO_2	33.95
CaF_2	8.62
Al_2O_3	8.32
TiO_2	8.02
Basicity Index	0.9

B. WELDING PROCESS

1. EQUIPMENT

Two direct current-constant voltage (DC-CV) power supplies (Fig.8) were connected in parallel to deliver 1300A at 100% duty cycle. The welding process was conducted in the direct current/reverse polarity mode. Voltage could be directly adjusted in the power supply or the control box. The current, being an indirect parameter, was controlled by the adjustment of the electrode feeding rate. The feeding system (Fig. 9) could smoothly supply wires into the weld pool with a single wire or dual wires, matching the winged or webbed guide plate design. Both run-in and run-off blocks were arc-welded onto the base metal prior to ESW, and cut off after the welds were completed. Those blocks assured the real joint to be free of starting defects and the final slag entrapment. A few strongbacks were also pre-welded on the

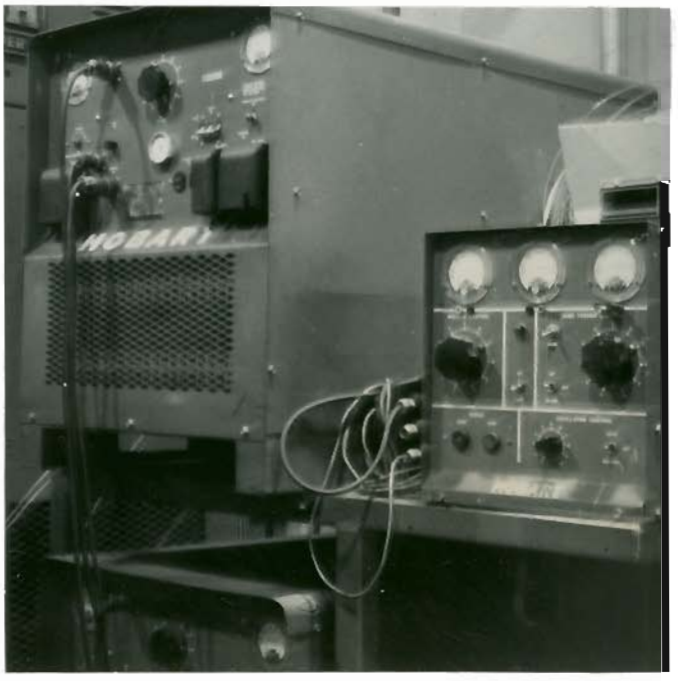

Fig. 8 Power supply of ES welding

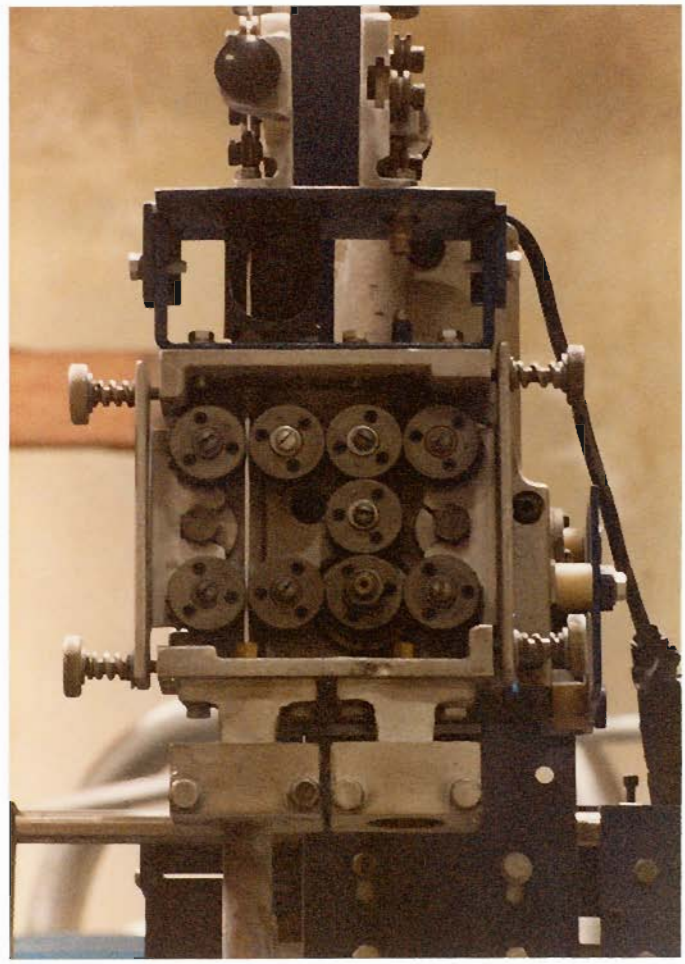

Fig. 9 Wire feeding device used for ESW

base metal to keep a desired joint gap from distortion and hold the cooling shoes in position.

At the very beginning of weld initiation, a certain amount of flux was put into the joint gap manually, assuring a rapid setting of the electroslag heating mode. Flux should be pre-baked to extract moisture off. Considering the normal slag depletion due to freezing between the cooling shoe and the weld metal, a flux continuous feeder (made by the TAPCO International) was attached to the welding head, and used to add flux into the molten slag pool at controllable rates to compensate for the slag loss.

Tap water-cooled copper shoes (Fig.10) were used to dam the weld pool and extract heat. The permanent shoe assembly consisted of an aluminum box for water circulation that was sandwiched between copper and aluminum backing plates. Cooling shoes, with a weld reinforcement depression machined on their copper surfaces, confined the weld contour. During welding, the shoes were wedged in place between the strongbacks.

2. GUIDE PLATE DESIGN

The guide tube/plate is an integral part for successful ESW. From previous experience, the standard 12 mm (1/2 in) or 16 mm (5/8 in) round guide tubes limited the current-carry capacities and tended to generate excessive heat in the middle of the weld pool at the expense of the edge heating near the cooling shoes, thus, causing lack of fusion and undercut problems. A far more efficient way to distribute

Fig. 10 Copper cooling shoes for ESW

the heat across the slag bath and to reduce the amount of filler metal deposted, while greatly increasing the current carrying capacity,employs a plate consumable guide configuration. In this project, both the winged and webbed guide plates were designed and used. Welds purposely made by the standard guide tubes were only for comparison. Fig. 11 shows both the configuration and dimension of standard guide tube, winged and webbed guide plates, in which the winged one was designed for joining 50mm thick base metals, while the two types of webbed guide plates were designed for joining 50 mm and 76 mm-thick base metals.

3. NARROW GAP TECHNIQUE

In this investigation, the 19mm (3/4 inch) gap ESW process was specified as the "narrow-gap technique", referring to the standard ES process with 31 mm (5/4 inch) joint gap. This narrow-gap technique has proved rather successful in reducing the total heat input of weldments in the previous DOT project (contract FH-11-9612). Thus, in most cases of this study, weld joint gaps were maintained at 19 mm. A few welds were made with the standard 31 mm (1.25 in) gap for comparison. All welds were deposited vertically with sufficient run-in and run-out blocks.

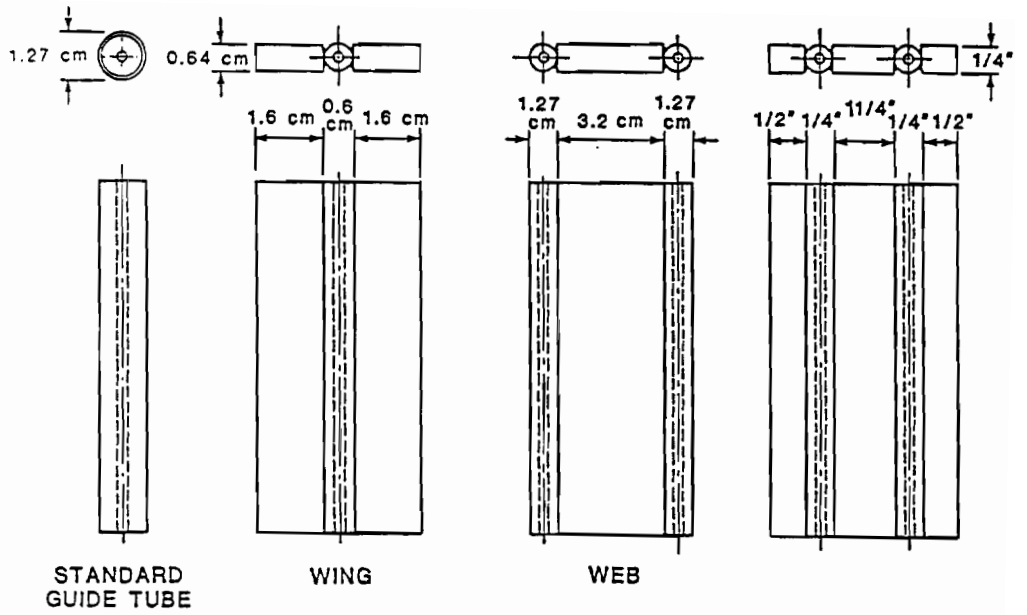

Fig.11 Configuration and size of consumable guide plates

C. EVALUATIONS

1. METALLOGRAPHY

Longitudinal and transverse specimens were cut from most weldments to examine their weld soundness and macrostructure. After being surface ground, a 10% Nital solution was used for macro-etching. Surfaces etched clearly demonstrated the shape of both weld metal zone and related HAZ. Solute bands revealed the contour of weld pool. Solidification substructures were revealed by Stead's reagent (mixed 10g $CuCl_2$, 40g $MgCl_2$, 20ml HCl and 1000ml methanol) and the solid phase transformation microstructures by 1% Nital solution. Optical metallographic observations and photographic work were carried out on in a Carl Zeiss microscope. A JEOL (JSM-35) scanning electronic microscope was also used to examine the fractographic features of weldments.

2. CHEMICAL ANALYSIS

A variety of typical weld metals were selected to analyze their as-deposited chemical compositions (including the oxygen and nitrogen contents). All samples were sent to the Metallurgy Laboratory of ESCO Company (Portland) and tested in a spectrographic analyzer.

3. HARDNESS

The B scale 1.5mm (1/16 in) diameter spherical steel indentor /100 kg major load) Rockwell hardness test was used for the weld metal as well as the HAZ. Three or more measurements were made at each region of interest and an average value was determined.

4. CHARPY V-NOTCH TOUGHNESS

The standard ASTM E23 Charpy V-notch impact specimens were cut from as-deposited joints. All specimen notches were perpendicular to the welding direction. Those notches were respectively located at the positions of 1) mid-thickness/weld center, 2) quarter-thickness/weld center, and 3) coarse grain HAZ-1 close to the fusion line. In order to obtain the ductile-brittle transition temperature curves of welds, The CVN impact toughness tests were conducted in the temperature range of -73 to +65°C (-100 to +150°F) in a 352 J (264 ft-lb) Tinius Olsen (pendulum type) impact testing machine. The instrumented testing system was connected to a modified APPLE computer to record the test data.

5. PLANE STRAIN FRACTURE TOUGHNESS

The compact tension K_{IC} specimens, in accordance with ASTM E-399, were 76 mm (3 inch)-thick (full weld thickness), and were tested with an intermediate loading rate (about 2 to 3 seconds to failure at -18°C (0°F) and other lower or higher temperature required to obtain valid testing curves. Thir chevron-shaped notches and extended fatigue pre-cracks were parallel to the welding direction and were located in the 1) weld centerline and 2) HAZ-1 respectively. Due to the geometrical shape of the weld metal and HAZ microstructures, it was impossible to produce a full section sample which could only test a single grain zone. For example, the notch of a weld centerline sample often covered a small amount of CCG zone near the surface edges of the crack, while the notch of a HAZ-1 sample always partially crossed the fine HAZ-2 and unaffected parent metal due to the curvature of fusion boundaries.

Both the pre-cracking operation and K_{Ic} testing were conducted in a MTS 810 mechanical testing machine. Before testing, specimens were immersed in an alcohol/dry ice mixed cooling chamber or an water heating bath to reach the temperature required.

D. SUMMARY OF WELD EXPERIMENT

During the whole of the project associated with contract DTFH61-83-R-0062, more than seventy welds were made. These were used in several different but parallel research subjects. Table 3 summarizes only those welds of interest to this investigation.

Table 3

Summary of Welds Related to This Study

Weld ID.	base metal	thickness (mm)	filler metal	gap (mm)	current(A) /Voltage(V)	heat input (KJ/mm)
1B-1	A36	50	25P	19	800/31	67
1B-2	A36	50	25P	19	800/44	70
2A-1	A36	50	25P	19	600/40	68
2A-2	A36	50	25P	19	1000/40	63
2B-1	A36	50	25P	19	1150/40	62
5B-1	A36	76	25P	19	1200/33	116
5B-2	A36	76	25P	19	1200/39	126
9C-1	A588	50	WS	19	1000/41	67
9B-1	A588	50	WS	19	1000/38	63
13A-1	A588	76	WS	19	950/32	103
13A-2	A588	76	WS	19	950/44	142
13B-1	A588	76	WS	19	950/38	123
14A-1	A588	76	WS	19	950/40	135
14A-2	A588	76	WS	19	1250/40	125
33A	A36	50	AS521 + 25P	19	1000/38	
33B-1	A36	50	AS521	32	1000/38	
33B-2	A36	50	AS521 + 25P	32	1000/38	
34	A588	50	AS521	19	1000/38	
35	A36	50	AS521	19	1000/38	
36A	A588	50	AS521	19	1000/38	
36B	A588	50	AS521 + WS	19	1000/38	
37	A36	50	AS521	19	1000/38	
38A	A588	50	AS521	32	1000/38	
38B	A588	50	AS521 + WS	32	1000/38	
40	A36	50	AX90	19	1000/38	62
41	A36	50	AX90	32	800/40	
42	A36	50	AX90	19	1000/38	60
43-1	A588	50	AX90	19	800/40	
43-2	A588	50	AX90	19	1000/38	58
44	A36	50	AX90 + 25P	19	1000/38	
45	A588	50	AX90 + WS	19	1000/38	
52	A36	50	8544	19	1000/38	
53	A36	50	8544	19	1000/38	
53	A36	50	8544	19	1000/35	

Table 3 (continue)

Weld ID.	base metal	thickness (mm)	filler metal	gap (mm)	current(A) /voltage(V)	heat input (KJ/mm)
54-1	A588	50	8544	19	1000/35	43.7
54-2	A588	50	8544	19	1000/32	37.3
55-1	A36	50	8544	19	1000/35	42.7
55-2	A36	50	8544	19	1000/32	35.6
56-1	A588	76	8544	19	1300/38	80
56-2	A588	76	8544	19	1300/35	74
56-3	A588	76	8544	19	1500/38	73
57-1	A36	76	8544	19	1300/35	74
57-2	A36	76	8544	19	1300/38	78
M150/A	A588	76	WS	32	850/38	151
M151/B	A36	76	25P	32	850/38	135
M152/C	A588	76	WS	32	850/38	143
M153/D	A36	50	25P	32	600/42	78.1
M154/E	A588	50	WS	32	600/42	100.5
M155/F	A36	76	25P	19	1000/40	90.2
M156/G	A36	76	25P	19	1100/40	86.6
M157/H	A588	76	WS	19	1000/38	86
M159/J	A36	76	8544	19	1000/38	84.5
M160/K	A36	76	8544	19	1000/38	83.5
M161/L	A588	76	8544	19	1000/38	84
M163/N	A36	76	25P	32	850/38	125
M164/O	A588	76	WS	32	850/38	135
M165/P	A36	50	25P	19	1000/38	63
M166/Q	A588	50	WS	19	1000/38	64
M167/R	A36	50	8544	19	800/38	65
M168/S	A588	50	8544	19	800/38	63
M171/V	A588	76	8544	19	1300/35	74
M172/W	A588	76	8544	19	1300/35	66
M173/Y	A36	50	8544	19	1000/35	41
M174	A36	76	8544	19	1300/35	72

IV. RESULTS

A. CHEMICAL COMPOSITION OF WELD METALS

Different combinations of base metal and filler metal resulted in a series of weld metal compositions. Variation of weld parameters, to a certain degree, also altered the weld metal compositions. Table 4 gives a number of typical data.

Table 4. Main Compositions of Some Typical Weld Metals (wt%)

plate/ thickness	filler metal	gap (mm)	heat input (KJ/mm)	C	Mn	Si	Ni	Mo	O (ppm)
A36/50mm	25p	19	63	0.18	1.10	0.40	--	--	240
	Ax90+25p	19	61	0.16	1.10	0.36	0.50	0.10	227
	Ax90	19	60	0.17	1.10	0.36	0.91	0.15	230
	TW8544	19	36	0.11	1.24	0.30	1.20	0.22	286
A36/76mm	25p	19	126	0.19	1.09	0.39	--	--	233
	TW8544	19	71	0.16	1.01	0,27	0.90	0.14	292
A588/50mm	WS	19	63	0.18	1.05	0.35	0.36	--	230
	AX90	19	62	0.13	1.20	0.36	0.94	0.16	260
	TW8544	19	37	0.11	1.21	0.35	1.47	0.25	289
A588/76mm	WS	19	125	0.19	1.11	0.37	0.32	--	221
	TW8544	19	74	0.11	1.15	0.41	1.25	0.15	294

Balance: Fe

B. MORPHOLOGICAL CHARACTERISTICS OF WELD METAL

1. VARIATION OF SOLIDIFICATION AND FERRITIC SUBSTRUCTURES

According to the OGC classification for the morphology of steel ES weldments, four characteristic cases of grain structure were clearly observed in the narrow-gap ES weld metal of low carbon steels, as shown in Fig. 6. Here, the four case system rather than the five type system [57] is introduced, because the oxygen content was approximately constant in most weld metals. In all cases, cellular dendrites grew epitaxially from the fusion boundaries towards the weld center and gradually transformed into columnar dendrites. This transition was defined as the occurrence of protrusions of noticeable secondary arms, as illustrated in Fig. 12.

The growth of both cellular dendrites and columnar dendrites followed the direction opposite to the maximum thermal gradient vector which was normal to the contour of the weld pool. The dendritic growth was strongly crystallographic. The growth of the arms was always parallel to the preferred crystallographic directions (<100> in both fcc and bcc structures). Thus, the local orientation of dendrites was in those <100> which were quite close to the direction of maximum thermal gradient [30]. In ESW, the direction of maximum thermal gradient gradually changed from nearly vertical to the weld axis at the weld interface to almost parallel at the weld center. A distinct feature of the dendritic structures was that, at different locations, they had different inclination angles, as shown in Figures 13 and 14.

It must be pointed out that dendrites, in general, always grew

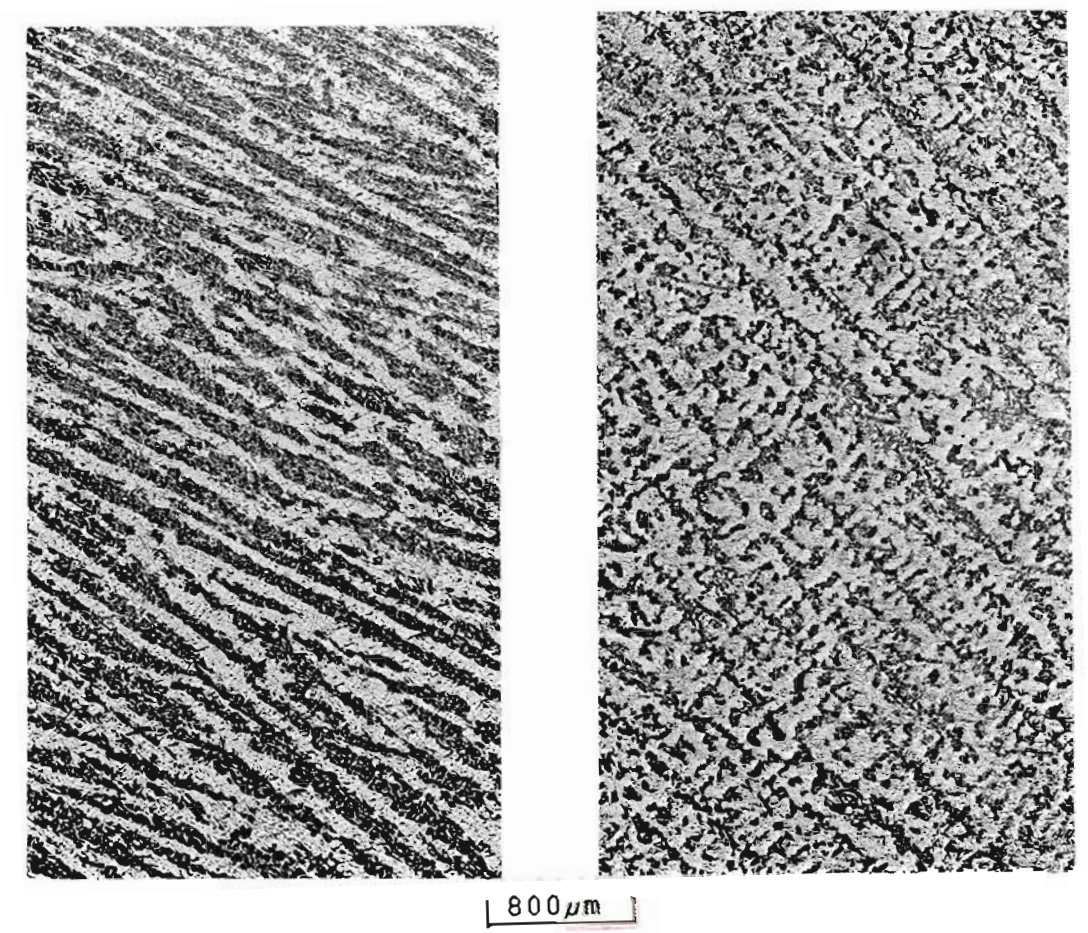

A. B.

Fig. 12 Typical dendritic structures defined in this study: A) Cellular Dendrites (minimum side arm development), and B) columnar dendrites (noticeable side arm protrusion). (Weld# 9C)

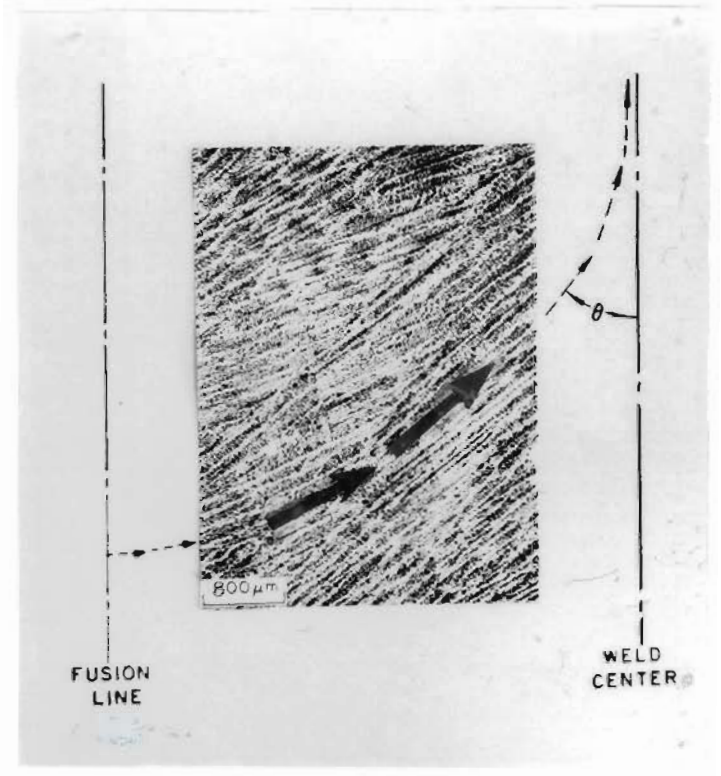

Fig. 13 Typical Renucleation Events in the Solidification Structure For Case 1 ESW of A36 steels (50mm Thick). (Weld# 1B-2)

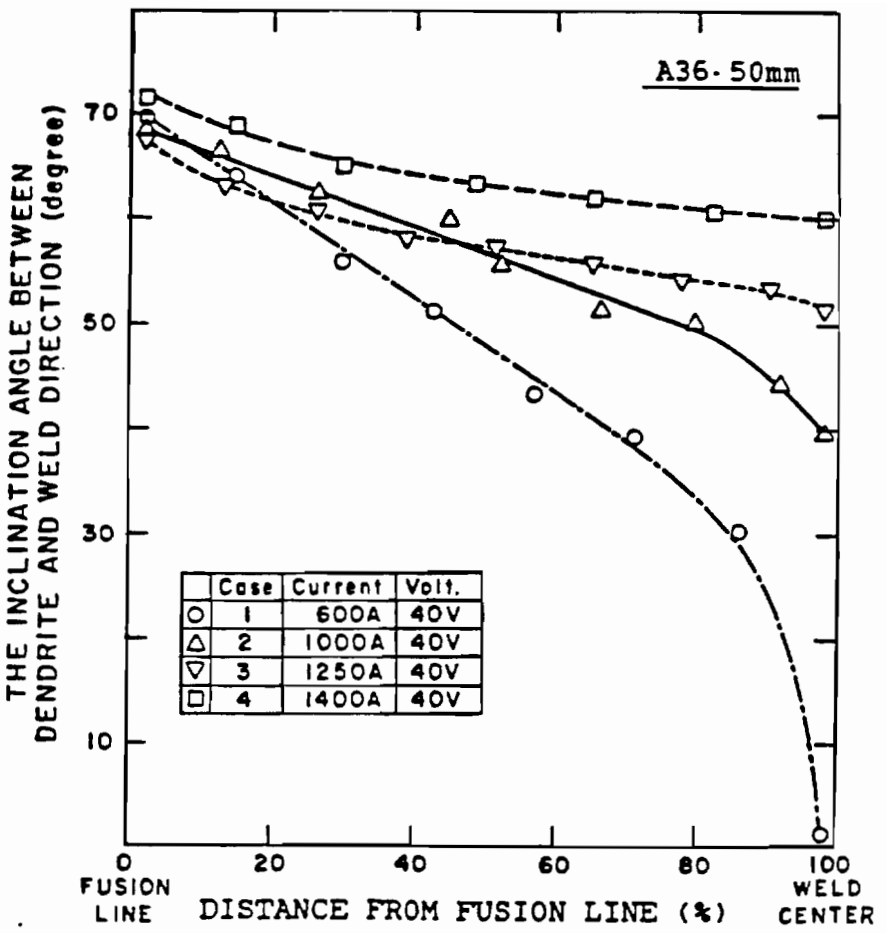

Fig. 14 Variation of dendrite inclination angle as a function of distance from the fusion line for each weld case

straight and did not bend. Thus, the necessary angular adjustment caused by the variation of the thermal gradient vector had to be accomplished by some mechanism involving dendrite re-nucleation and solute banding.

In case 1, ignoring the small planar zone at the start of solidification, the transition from cellular dendrites to columnar dendrites occurred at a short distance from the fusionline. Frequent re-nucleation events took place, due to the large variation of the grain inclination angle (see Fig.14). Near the central portion, dendrites became almost fully parallel to the direction of welding. In the corresponding solid state microstructure, a very small percentage of acicular ferrite-rich coarse columnar grains occupied the portion near the fusion lines, and a large area of weld metal consisted of a mixture dominated by grain-boundary ferrite and side-plate ferrite.

In case 2, the cellular dendritic-columnar dendritic transition occurred farther from the fusion line than case 1. The renucleation events were less frequent than the case 1 due to the reduced inclination angle (see Fig. 14). Near the center of welds, dendrites met with an larger angle. In the corresponding solid state microstructure, a certain amount of acicular ferrite-rich coarse columnar grains existed on both sides of the weld center, while the center part of the weld metal was composed of thin columnar grains.

In case 3, the cellular dendritic-columnar dendritic transition occurred close to the weld center, compared with cases 1 and 2. The change of grain inclination angle was only around ten degrees. Renucleation events were substantially less. And dendrites met at the

weld centerline at an obtuse angle to the weld axis. The as-deposited microstructure contained a great amount of acicular ferrite-rich coarse columnar grains and a minor amount of thin columnar grains. However, the case 3 weld exhibited high sensitivity to the centerline hot cracking as well.

In case 4, the growth of dendrites was similar to that of case 3. The cellular dendritic-columnar dendritic transition was close to the centerline. However, at the weld center, short columnar dendrites became entirely random and showed the feature of equiaxed dendrites. In the as-deposited microstructure, there were some central islands of equiaxed grains and a large area of coarse columnar grains. Both were acicular ferrite-rich. The presence of an equiaxed zone at the weld center effectively prevented from hot cracking there. Instead, radial hot cracks were found outside the equiaxed grain region, which always propagated along the interfaces of columnar grains exhibiting some kind of "herring-bone" appearance (being discussed later).

In comparing the primary solidification structure and the as-welded solid state microstructure of all welds, an interesting phenomenon was found. In spite of the differences between the alloy chemistry, the weld parameters, and the morphological cases, the percentage of cellular dendrites was always similar to the percentage of coarse columnar grains. The percentage of columnar dendrites was similar to the percentage of thin columnar grains as well, as illustrated in Table 5 and Figures 15 and 16. No doubt, there must be a certain correlation between the two structures.

TABLE 5

Correlation Between Percentage of Cellular Dendrites

and Coarse Columnar Grains in Weld Metals Deposited By ESW

base metal	current /voltage	number of feeding wire	heat input (KJ/mm^2)	form factor /weld case	morphology detail (%)	
					cellular dendrites	coarse columnar grains
50mm A36	600A /40V	1	1.29	2.2 /1	32%	34%
50mm A36	800A /44V	1	1.52	2.2 /1	33%	31%
76mm A36	1200A /40V	2	1.26	1.7 /2	53%	55%
50mm A588	1000A /40V	2	1.38	1.5 /2	33%	34%
50mm A36	1150A /40V	1	1.19	1.4 /2	42%	40%
50mm A588	1000A /38V	2	1.04	1.2 /3	68%	69%
50mm A36	800A /31V	1	0.96	1.2 /3	60%	60%
76mm A36	1200A /38V	2	1.18	1.0 /4	79%	78%

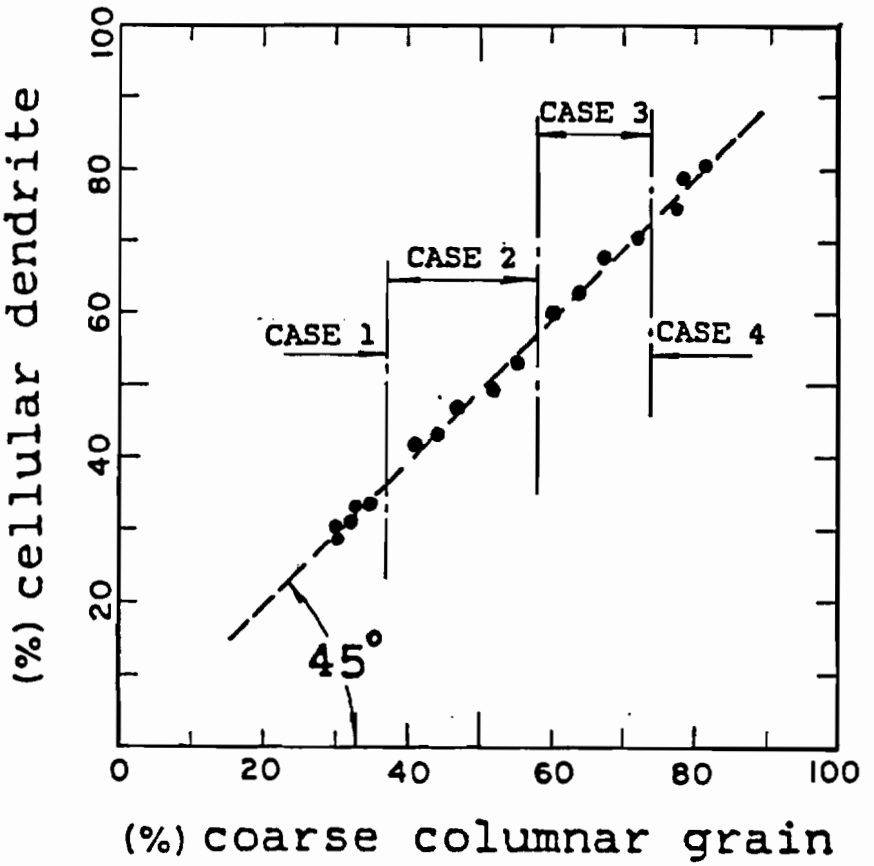

Fig. 15 Correlation between the amount of cellular dendrites (%) and the extent of the coarse columnar grain zone (%) in a series of steel ES weld metals

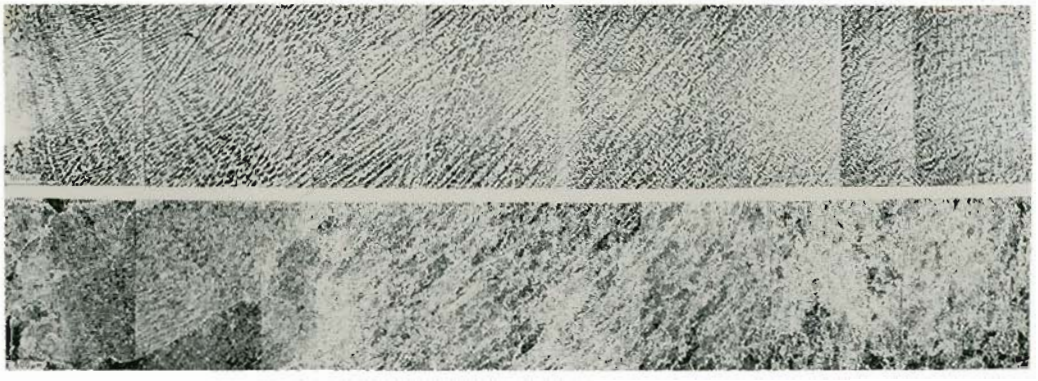

Fig. 16 Comparison between solidification structure and solid state microstructure in two 50mm thick A36 weld metals having different form factors. (Weld# 1B-2 and 2B-1)

2. MEASUREMENT OF DENDRITE ARM SPACING

As is well-known, there is an inverse relationship between the dendrite spacing (d) and the local cooling rate (GR) in the form of

$$d=A/(GR)^m \quad [90] \qquad --(2)$$

(where A and m are material constants). Thus, the dendrite arm spacing accurately reflects the local cooling situation. The data of primary dendrite spacing measurements is shown in a series of figures. Fig.17 is the comparison of spacing variation at different welding speeds. Fig.18 is the comparison of spacing variation for different heat input values. Then, Fig.19 shows the comparison of different weld cases. Fig. 20 shows the comparison of two case 4 welds with different base metals and different heat input levels.

These figures demonstrated that:

1) In spite of the variation of power input and weld speed, at the fusion line, the starting cell spacing for all welds remained quite similar. No correlation was observed between the coarsened HAZ grain size and the epitaxially nucleated cell spacing.

2) An identical trend of increasing dendrite arm spacing from the fusion line to the weld center was found regardless of welding parameters.

3) The variation of welding speed did not have a severe effect on dendrite arm spacing when heat input was held constant.

4) The increased heat input always increased the dendrite arm spacing except near the fusion line.

5) In case 4 welds, during the transition from the columnar dendritic to the equiaxed dendritic growth, the dendrite arm spacing around the weld center often increased abruptly.

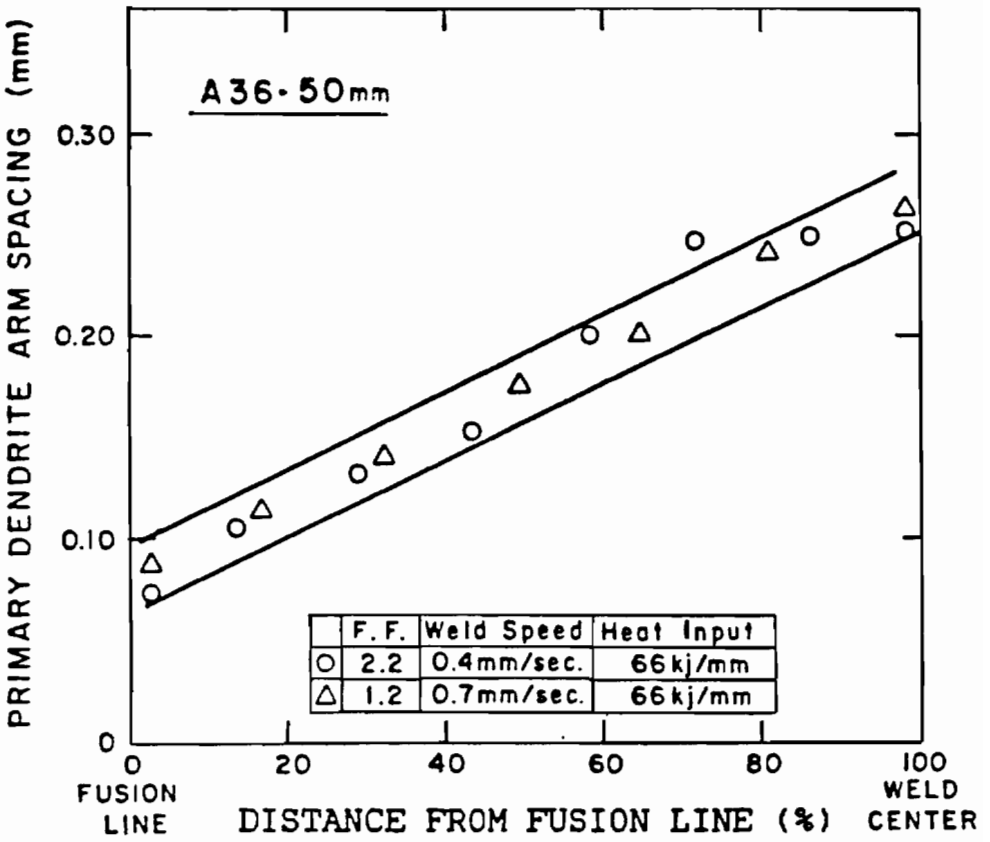

Fig. 17 Primary dendrite arm spacing as a function of distance from fusion line of weld metal deposited on 50mm thick A36 steel

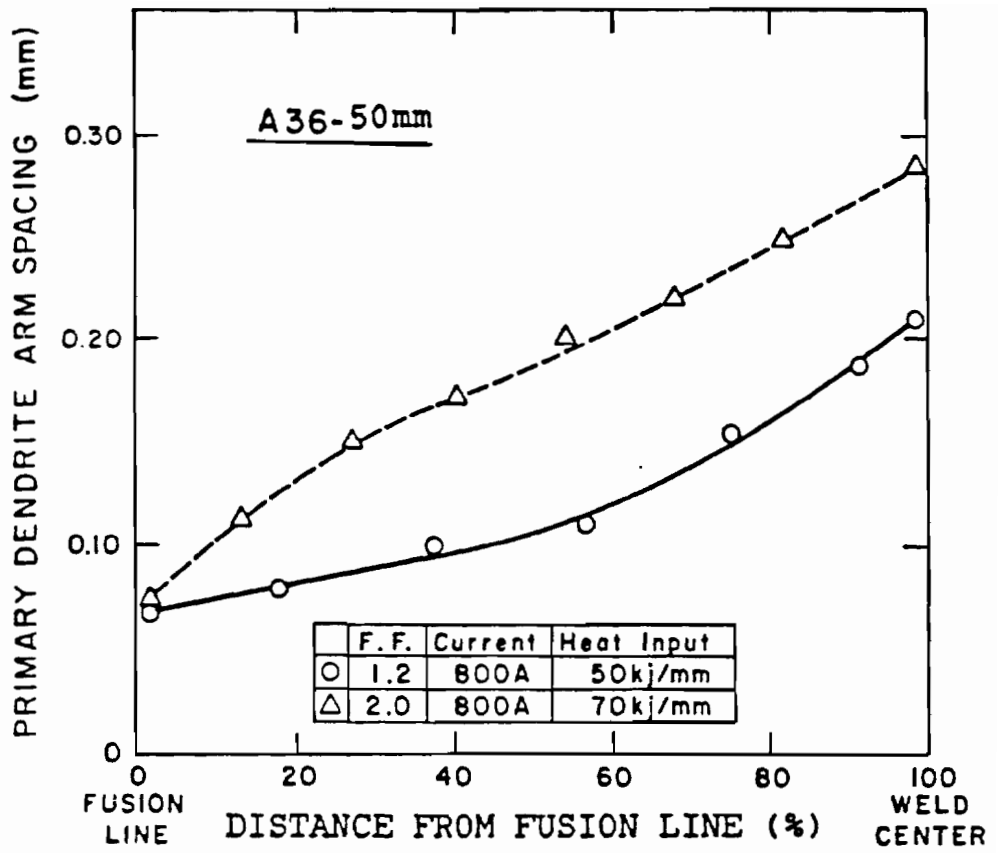

Fig. 18 Primary dendrite arm spacing as a function of distance from the fusion line of weld metal deposited on 50mm thick A36 steel

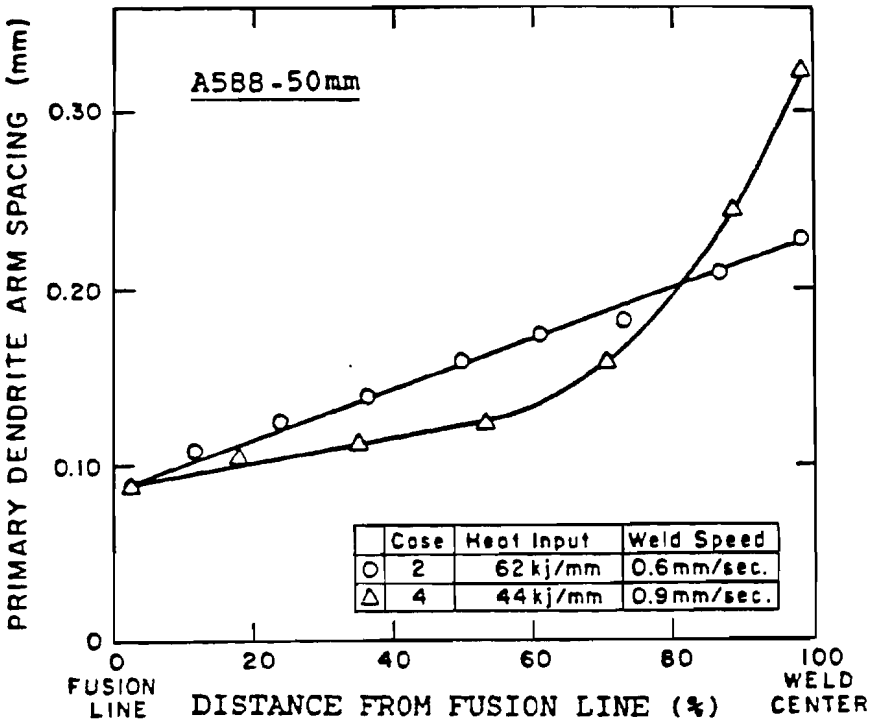

FiG. 19 The effect of welding speed on the primary dendrite arm spacing as a function of weld metal deposited on 50mm thick A588 steel

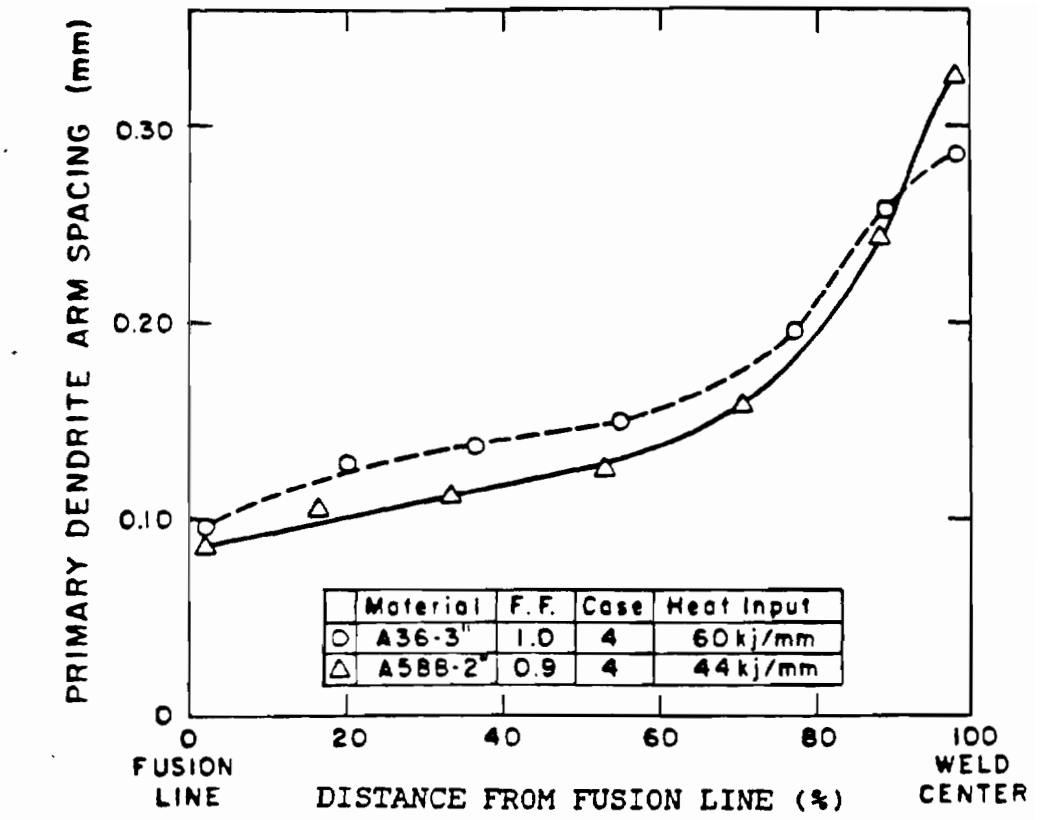

Fig. 20 Primary dendrite arm spacings for case 4 ES weld metals deposited on 76mm thick A36 and 50mm thick A588 steels

3. WELD POOL FORM FACTOR

The form factor is the ratio of the width of weld pool to the depth of weld pool. Weld parameters controlled the magnitude of the form factor. Two important parameters controlling the form factor were the electrode feed rate which changed the depth of the weld pool, and the weld voltage which varied the sidewall penetration of the weld pool. The electrode feed rate, in practice, was often considered as a direct function of weld current. However, for the same welding current setting, a dual-wire feeding weld had a shallower weld pool depth than a single-wire feeding one, thereby, resulting in a higher form factor.

The variation from case 1 to case 4 was found to be dependent upon the form factor (Figure 21). A high form factor (>2.0) resulted in a small percentage of coarse columnar grains, which corresponded to the case 1 morphology. When the value of form factor dropped from 2 to 1.2 (case 2), the percentage of coarse columnar grains increased greatly. When it became below 1.2, the weld metal showed the appearance of case 3, and below 1.0, case 4 was developed. Although the percentage of coarse columnar grains was quite high in both cases 3 and 4, severe hot cracking resulted. Therefore, the recommended optimum condition for the narrow-gap ESW without hot cracking was case 2, since the form factor values was about 1.2 to 1.6. The relationship between the form factor and the relative amounts of various substructures is illustrated in Fig. 22.

From a practical point of view, a more direct correlation may be set between the weld parameters and the width of coarse columnar grains zone (see Fig. 23 and 24). Increasing the current required an

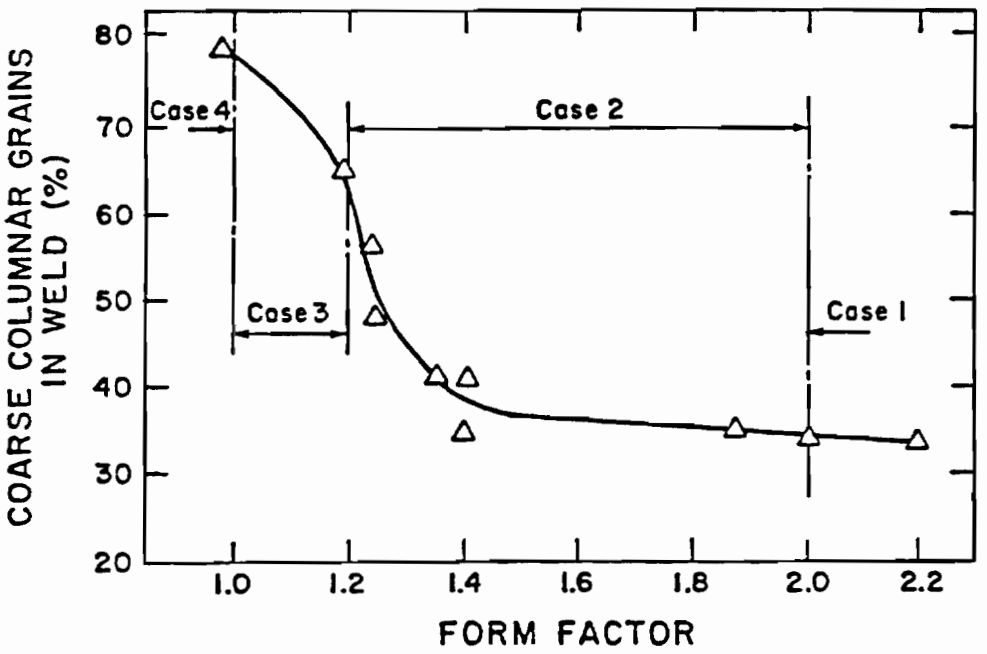

Fig. 21 Correlation between form factor and the amount of coarse columnar grains in 50mm thick A36 electroslag welds.

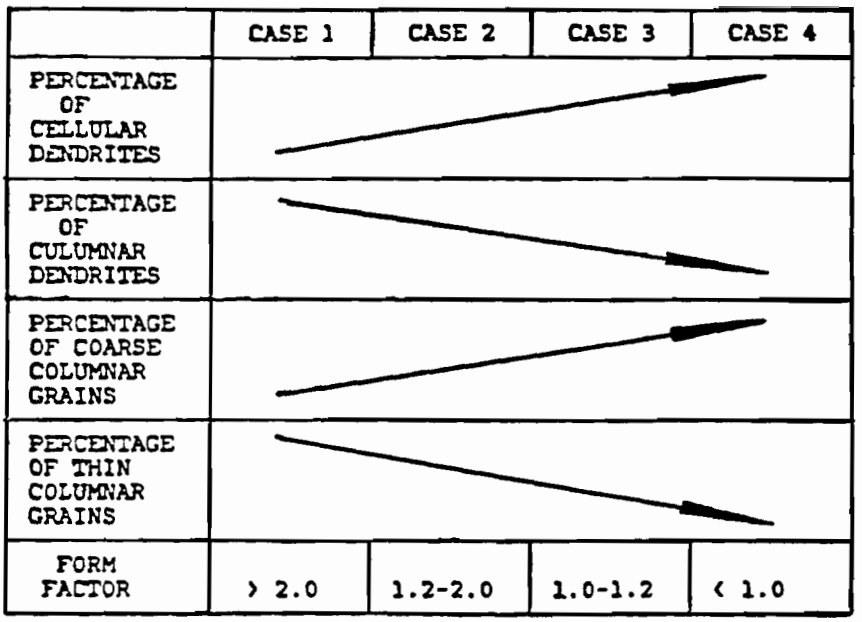

Fig. 22 Schematic expression of relationship between weld case, form factor, macro- and microstructures.

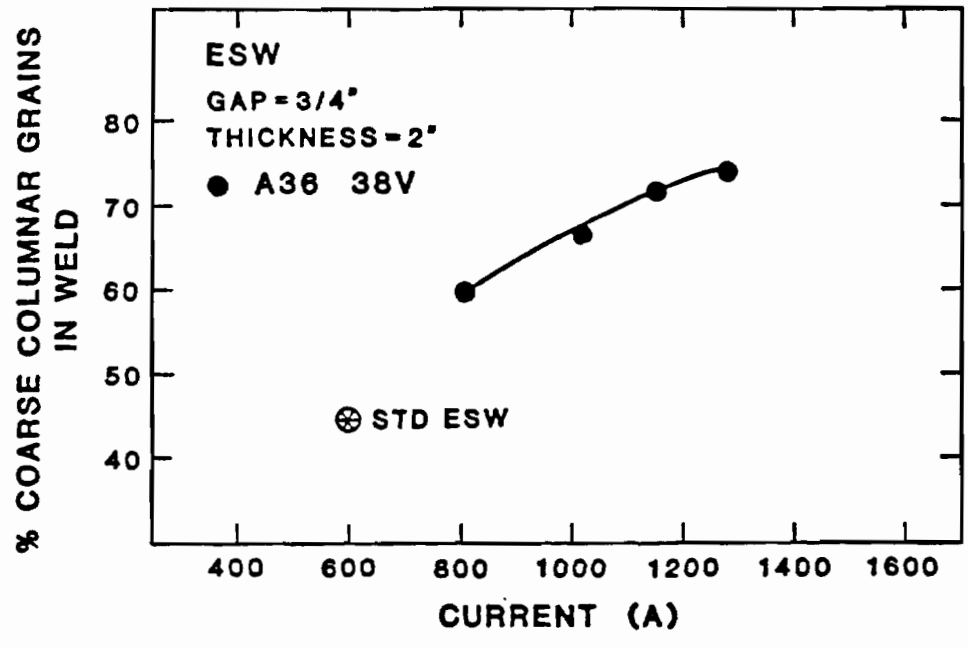

Fig. 23 Correlation between weld current and coarse columnar grains

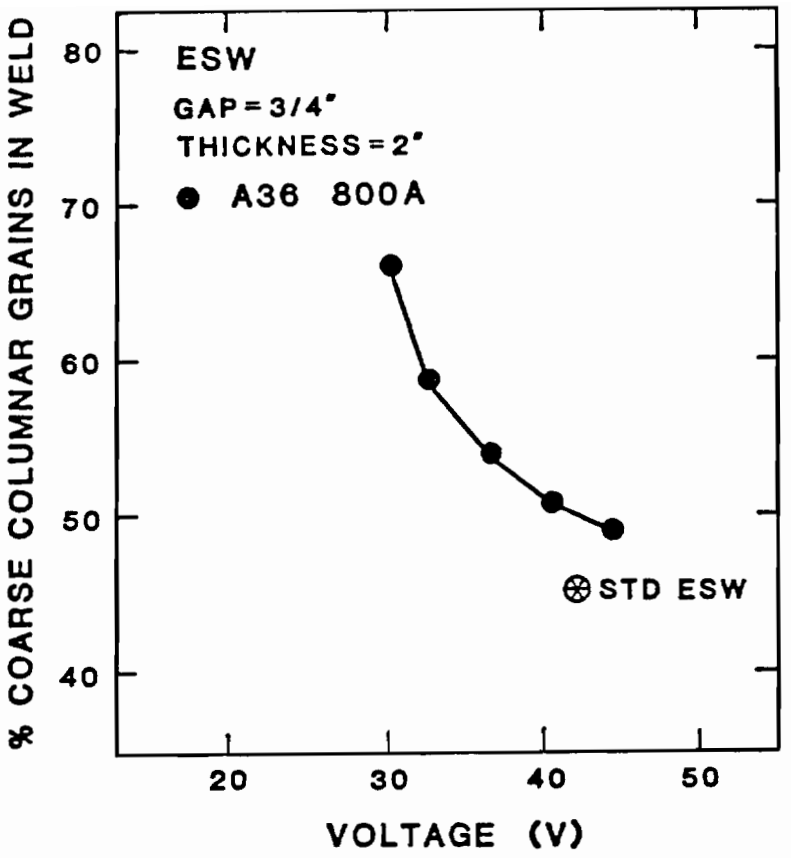

Fig. 24 Correlation between welding voltage and coarse columnar grains

increased electrode feed rate which deepened the weld pool and reduced the form factor. As a result, it enhanced the size of the coarse columnar grain zone. The increase of voltage promoted (a) an increase in the heat input and penetration, (b) an increase in the form factor, and (c) a reduction in the size of the coarse columnar grain zone.

4. SOLIDIFICATION HOT CRACKING

Two kinds of solidification defects, the centerline cracking and the radial cracking (see Figures 25 and 26), were observed depending upon the welding conditions as summarized in Table 5. The centerline hot cracking, appearing in case 3, was caused by the formation of a plane of weakness at the weld center, where solidification fronts from two opposite sides of the weld impinged at an obtuse meeting angle caused by high welding speeds. The radial hot cracking, appearing in case 4 was strongly related to the cracking resistance of the equiaxed zone near the center of the deep weld pool.

Both kinds of hot cracking had a high probability of occurrence and caused a severe disparity of toughness distribution across the weld metal. Alloying the weld metal could eliminate those hot cracks, while still developing the central equiaxed grains at the weld center in a moderate deep weld pool. This will be discussed later.

Fig. 25. Centerline hot cracking in case 3 ES Weld (A36/76mm thick, Weld# 5B-2): a) dendritic structure, b) solid state microstructure.

a)

500μm

b)

Fig. 26 Radial hot cracking in case 4 ES weld (A36/ 75mm thick Weld# 5B-1): a) dendritic structure, and b) solid state microstructure.

TABLE 6

SOLIDIFICATION DEFECTS IN

NARROW-GAP ES WELD METAL

	WELD CASE 3	WELD CASE 4
LOCATION	centerline	interfaces of thin columnar grains and columnar dendrite
TYPE OF DEFECT	hot cracking	hot cracking
LENGTH	10-80mm	1-10mm
TYPICAL CONDITION:		
current	1100-1300A.	1200-1550A
voltage	36-40V	36-40V
FORM FACTOR	1.0-1.2	<1.0

5. DISTRIBUTION OF INCLUSIONS

As mentioned previously, inclusions in weld metals were the result of chemical reactions taking place in the melt as the weld pool cooled. As the temperature fell and oxygen became less soluble in the molten steel, the reaction between oxygen and deoxidants inside the weld pool exceeded the solubility limit. Globules of immiscible scible liquid or solid formed, which then were entrapped in the solidified weld metal.

Normally, both polishing and etching inevitably remove some inclusions so that few micrographs published clearly demonstrated the real inclusion population and distribution. But, Figures 27, 28 and 29 very successfully reveals the distribution of inclusions in the solidification substructure of an A36 steel electroslag weld metal, which contained 320ppm oxygen. (Fig.27, 28 and 29 respectively display three continuous portions of a metallograph of Weld# 43-2.) In those micrographs, the following features were observed:

(1) the inclusion population in the weld metal was much higher than in the base metal (Fig. 27);

(2) near the fusion boundaries, where cells grew epitaxially, fine inclusions (0.2-0.35m) were densely populated (Fig. 27);

(3) Fine inclusions (0.2-055m) almost continuously decorated all the inter-dendritic boundaries over the whole weld (Fig. 27, 28, 29);

(4) most of the coarse inclusions (>0.55m, especially around 1-35m) seemed to be pushed to the the central region of weld metal.

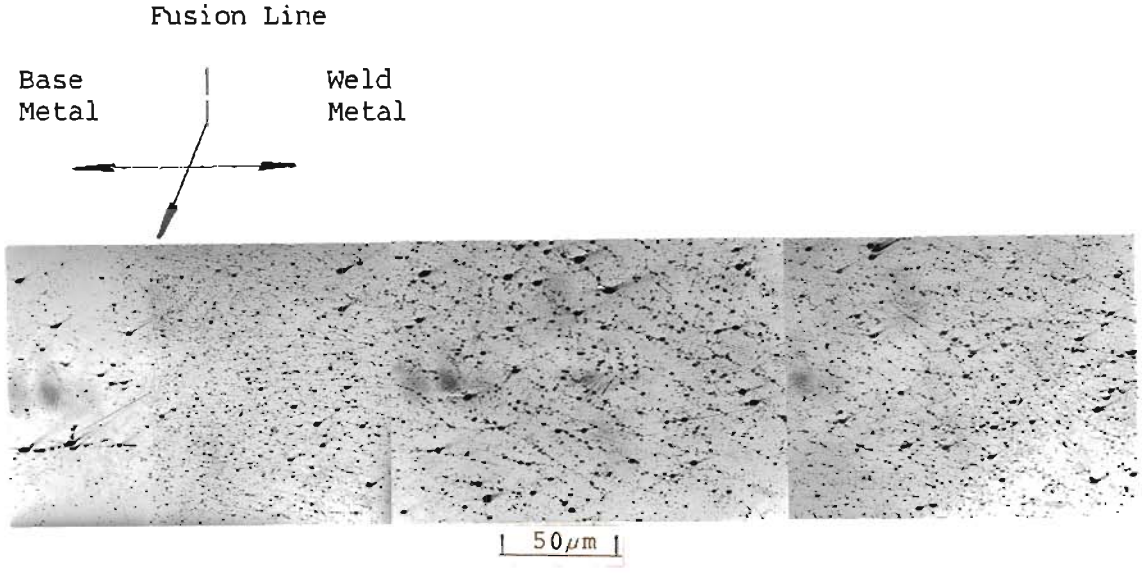

Fig. 27 Distribution of inclusions in the primary solidification structure near the fusion boundary of Weld #43-2

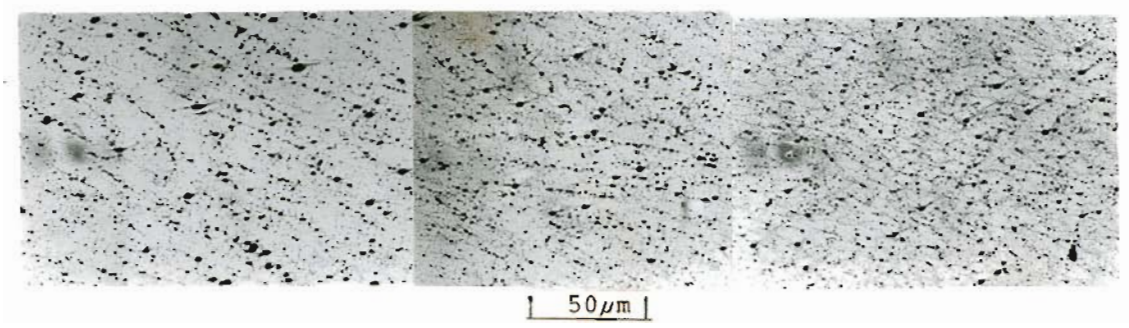

Fig. 28 Distribution of inclusions in the primary solidification structure of the columnar dendrite region of Weld # 43-2

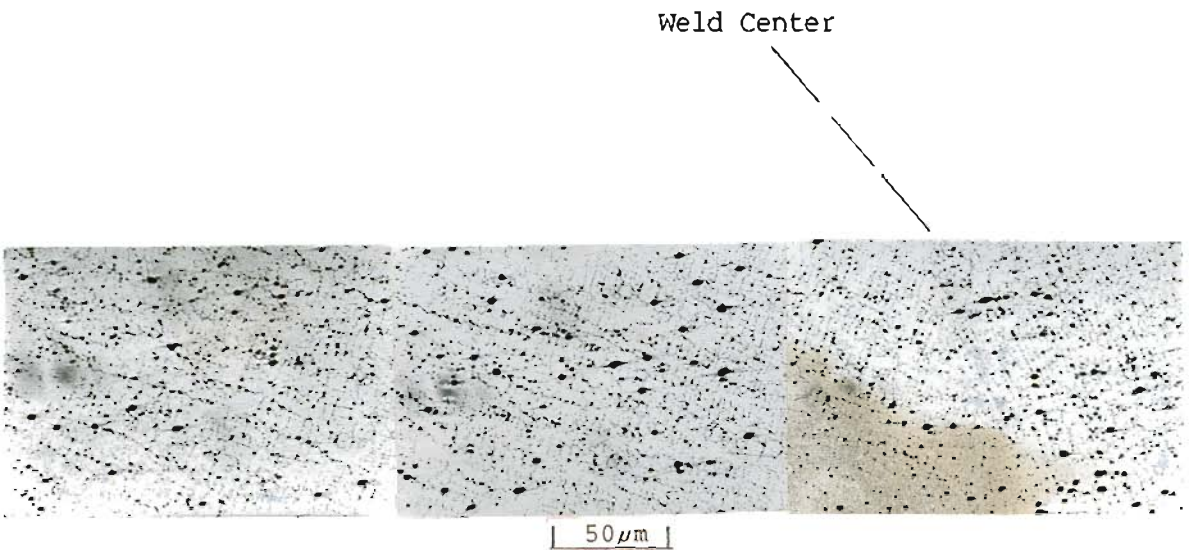

Fig. 29 Distribution of inclusions in the primary solidification structure near the weld center of Weld # 43-2

C. EFFECTS OF ALLOYING ADDITIONS ON MICROSTRUCTURE

1. ALLOYING-INDUCED EQUIAXED DENDRITES

Small amounts of Cr, Ni and Mo added to the A36 and A588 weld metals (which already contained about 1% Mn from the Mn content of the base steels) produced a major change in the solidification mode (from columnar dendritic to equiaxed dendritic) at the weld center. With a form factor value about 1.2-1.4, a mild steel filler typically produced columnar dendrites at the weld center (Fig. 30-a). But, a low Cr-Mo or Ni-Mo filler metal (AS521, AX90 or TW8544) brought about a substantial equiaxed dendrite region in the weld center (Figures 30-b and 30-c), through the strong effect of constitutional supercooling.

2. Cr-Mn-Mo ALLOYING

In addition to their effects on the solidification structure, alloy additions displayed more clear influences on the ferritic transformation products which directly affected the mechanical behaviors of weld metals.

When weld metal cools down below the Ac3 temperature, austenite decomposition occurs. The essential constituents in the low carbon steel weld metal could include: grain boundary ferrite (and linked alotriomorph), side-plate ferrite, acicular ferrite as well as bainitic ferrite, in approximately decreasing order of transformation temperature. The additions of Cr and Mo significantly governed the ferrite morphology of weld metal. Fig. 31 indicates that the volume fractions of micro-constituents constituents varied with the increase of alloy content in both A36 and A588 weld metals. Data in the extreme left of

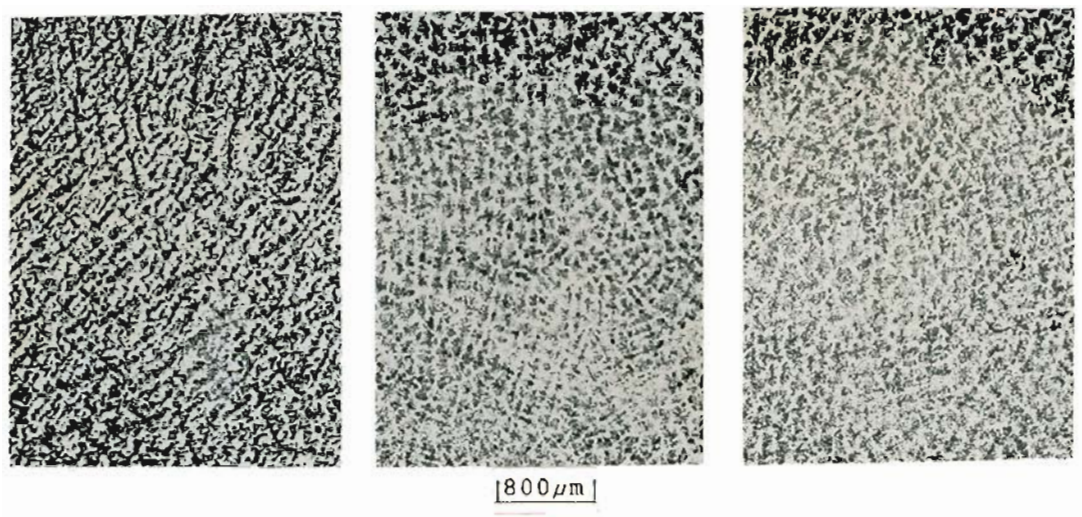

A. B. C.

Fig. 30 Dendritic Structures in the Weld center of 50mm A36 ES weldments using the filler metals of a) 25p (Weld #2A-2), b) AS251 (Weld #37), and c) Ax90 (Weld #42).

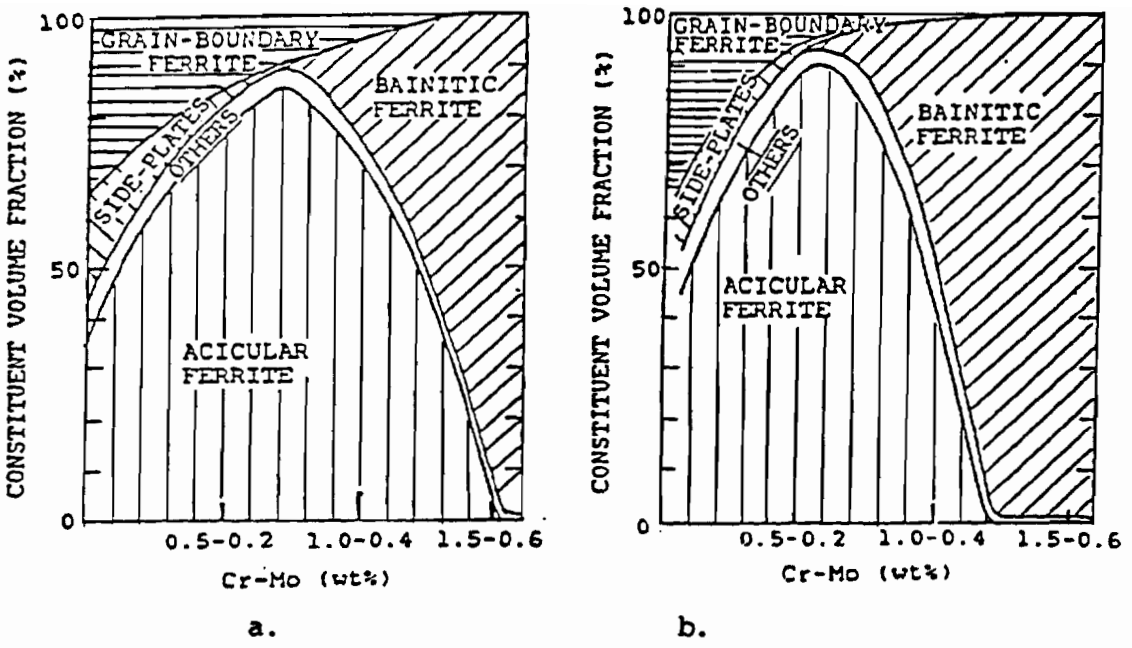

Fig. 31 Effect of Cr-Mo additions on the constituent volume fractions in weld metal deposited by ESW on 50mm-thick a) A36, and b) A588 steel

each diagram in Fig. 31 represents the case of mild steel filler.

With a constant Mn content of about 1.0% to 1.2%, Cr-Mo additions effectively reduced grain-boundary ferrite and side-plate ferrite, and increased acicular ferrite as long as the alloy content was below 0.7% Cr-0.3% Mo (Fig 32). When the Cr-Mo content exceeded those values, the volume fraction of acicular ferrite decreased, while bainitic ferrite increased. Further increasing the alloy content above 1.1%Cr and 0.4%Mo resulted in a fully bainitic microstructure (Fig.33 and 34).

3. Ni-Mn-Mo ALLOYING

With a constant Mn content of about 1.0% to 1.2%, Ni-Mo additions, within the limit of this investigation (1.5%Ni-0.3%Mo), not only sharply reduced both grain-boundary ferrite and side-plate ferrite, but also substantially promoted the formation of acicular ferrite. With the increase of Ni and Mo contents, the prior austenite grain boundaries were no longer decorated by proeutectoid ferrite. The volume fraction of acicular ferrite steadily increased and reached 90% or more when the weld metal contained 1.0% Ni, 0.2% Mo and 1.0% Mn, as shown in Fig. 35. The acicular ferrite plate size became finer with the increase in alloying content as shown in Figures 36 and 37. Using the TW8544 wire, the highest Ni, Mo and Mn contents in the diluted weld metal reached 1.5%, 0.3% and 1.2% respectively, with no bainitic ferrite or martensite present. Therefore, in such Ni-Mo alloyed A36 and A588 steel welds, acicular ferrite became the major constituent throughout the weld metal, regardless of the difference in the prior austenite

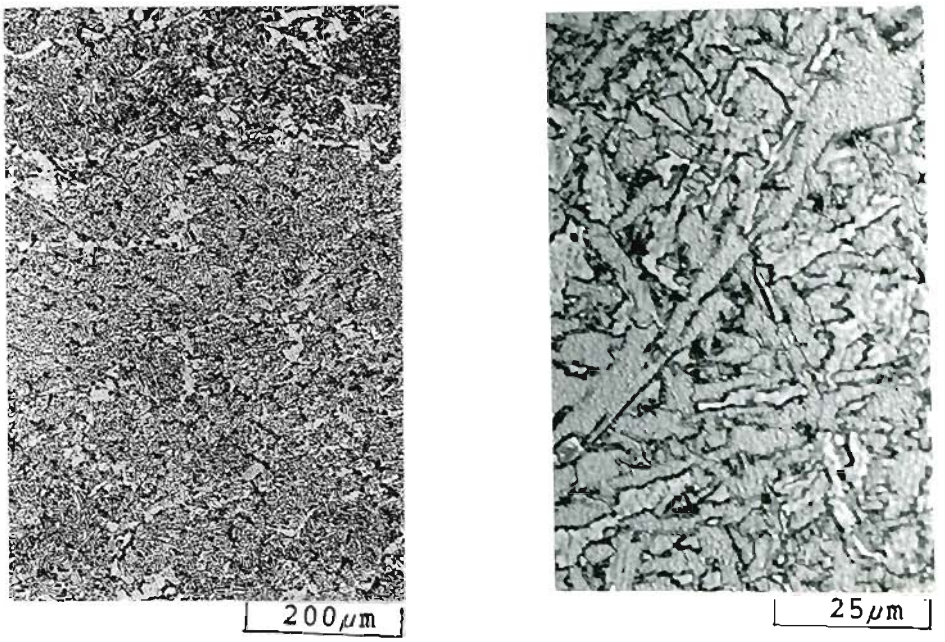

Fig. 32 Weld center microstructure of A36/50mm thick weld deposited with both AS521 and 25P filler metals and containing 0.67% Cr and 0.24% Mo. (Weld #33B-2)

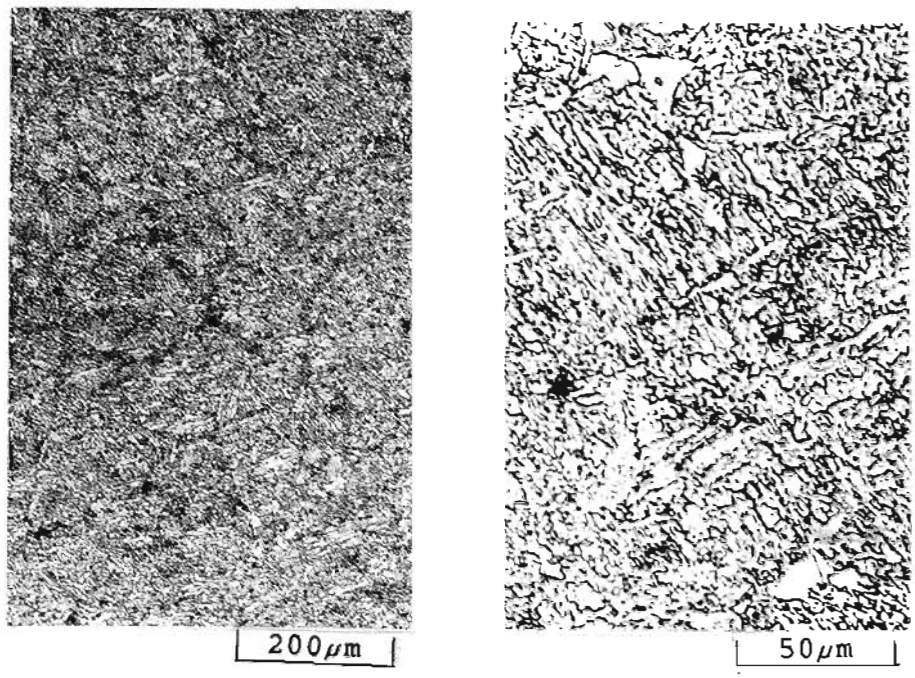

Fig.33 Weld center microstructure of A36/50mm thick weld deposited With AS521 filler metal and containing 1.20%Cr and 0.40% Mo. (Weld #36B)

Fig. 34 Bainitic ferrite in A588/50mm thick weld metal deposited with AS521 filler metal and containing 1.20% Cr and 0.40% Mo. (Weld #36B)

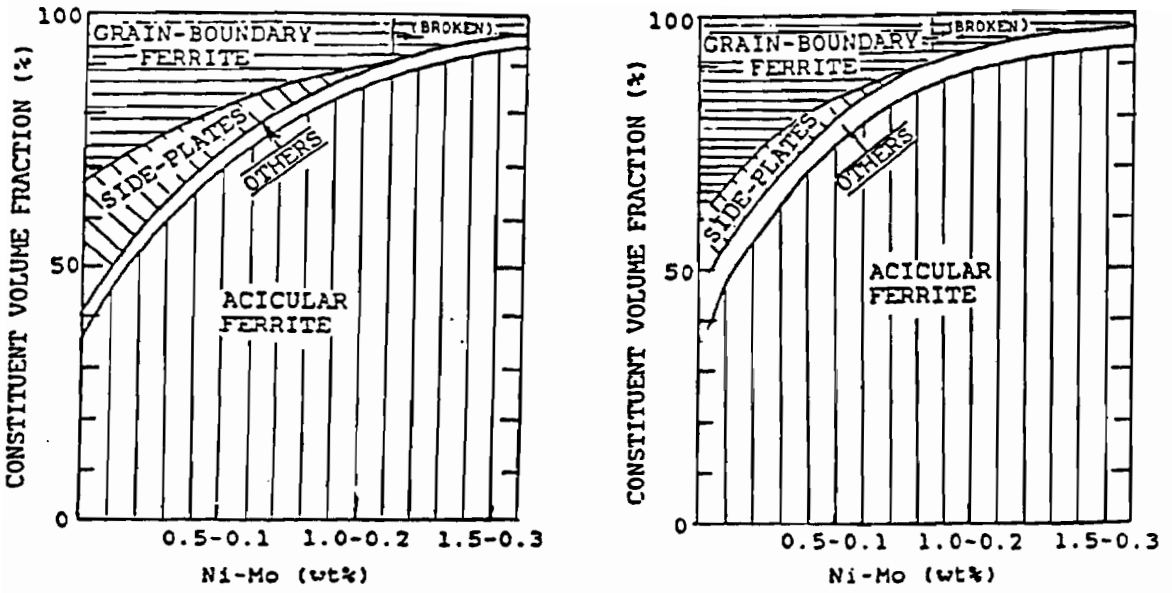

Fig.35. Effect of Ni-Mo additions on the constituent volume fractions of a) A36 and b) A588 [50mm thick] ES weld metal.

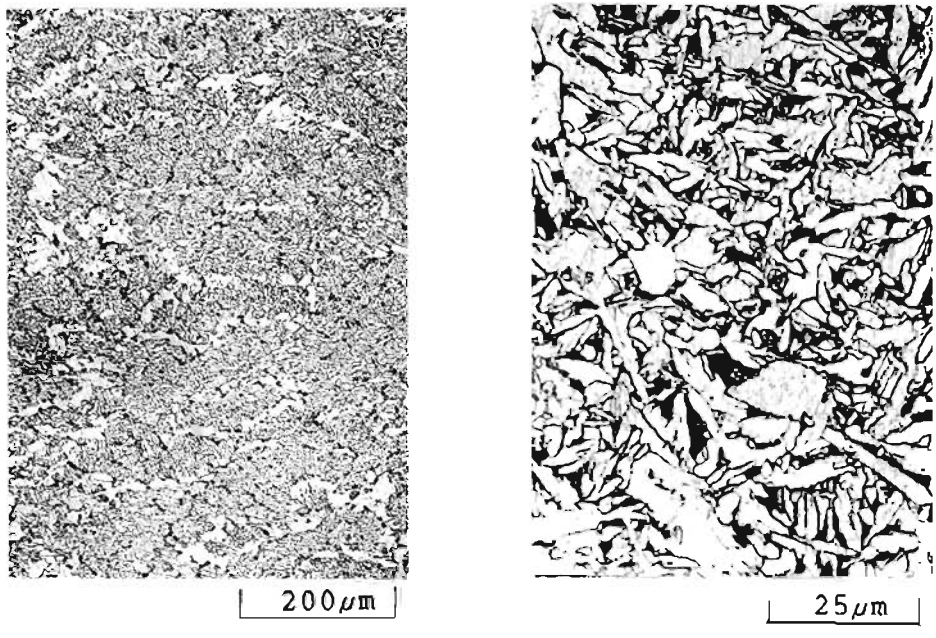

Fig.36 Weld center microstructure of A36/50mm thick ES weld deposited with both AX90 and 25P filler metals and containing 0.50% Ni and 0.10% Mo. (Weld #44)

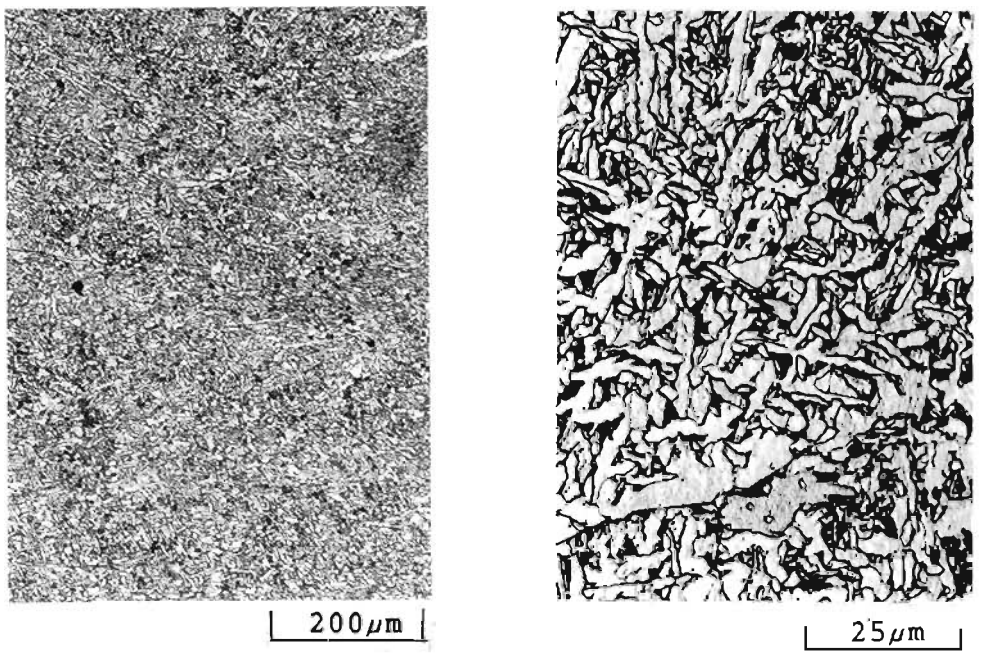

Fig.37 Weld center microstructure of A36/50mm thick ES weld deposited with TW8544 filler metal and containing 1.20% Ni and 0.22% Mo. (Weld #55)

grain size and location within the weld.

To emphasize the great morphological difference between the unalloyed and alloyed steel weld metals, Fig. 38 presents a few typical microstructures of A36 weld metals deposited with a) the conventional mild steel filler metal, 25P; b) the Cr-Mo alloyed filler metal, AS521; and c) the Ni-Mo alloyed filler metal, TW8544.

D. TUBULAR VS. SOLID FILLER METAL

Metal powder-cored tubular filler metals demonstrated several advantages in this investigation. These were as follows:

1) At a given current, voltage, joint-gap and guide-plate configration, welds deposited with a tubular filler metal exhibited significantly decreased heat input as seen in Fig. 39. Using solid wires, the minimum heat input values to make sound narrow-gap ES weldments were about 65 kJ/mm for 50mm thick welds and 90 kJ/mm for 76mm thick welds. This represented a substantial reduction in heat input in comparison with conventional gap welds, 80kJ/mm and 120kJ/mm. However, the heat input of tubular wire depositions could be easily reduced to about 40 kJ/mm for 50mm-thick welds and 70 kJ/mm for 76mm-thick welds.

2) For a given current, tubular filler metals increased the deposition rate of consumable guide ESW. For example, 1200mm-long by 50mm-thick steel plates required 23 minutes with tubular wire deposition, while a solid wire deposition required at least 30 minutes.

3) Tubular filler metal also decreased the base metal dilution, i.e. reduced the weld penetration. Fig.40 shows a clear trend that at the

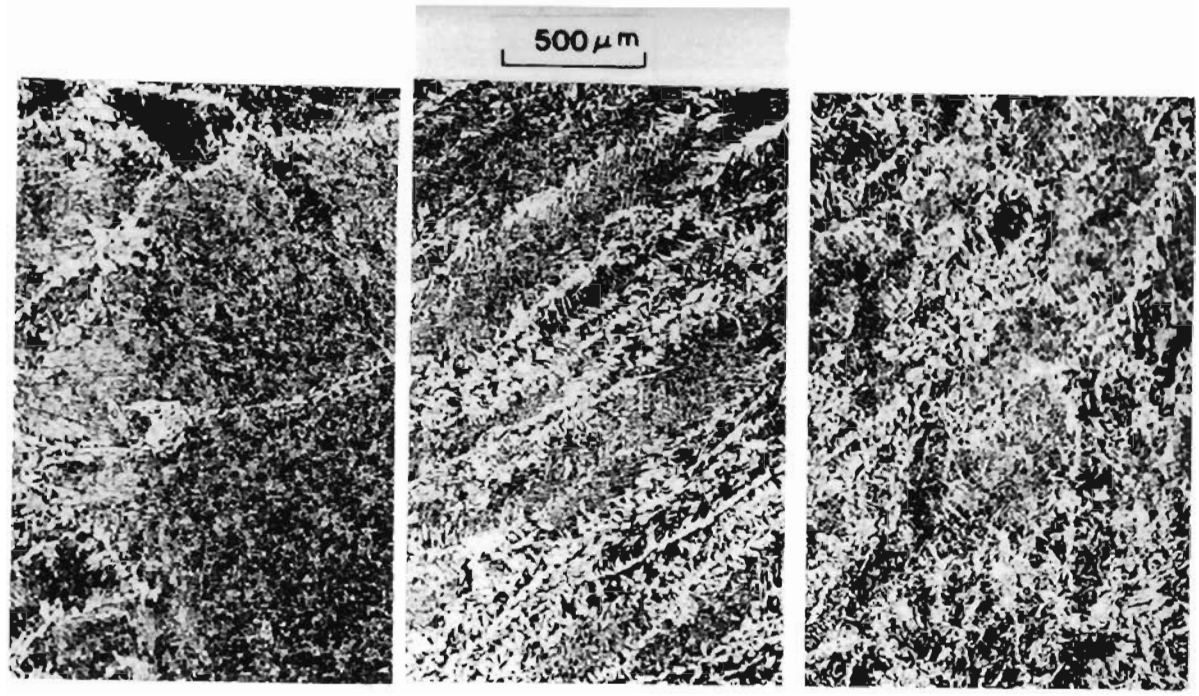

A. B. C.

Fig.38-a Typical microstructure of A36/50mm thick ES weld metal deposited by 25p mild steel wire: at A) fusion line, B) 1/4 width of weld metal, and C) centerline of weld #2A-2.

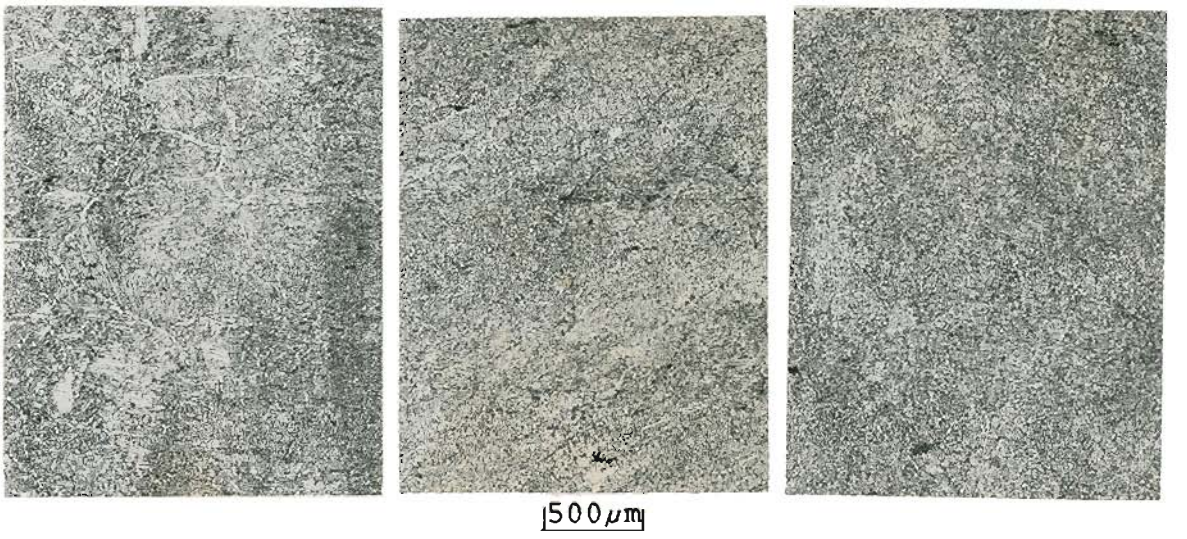

A. B. C.

Fig. 38-b Typical microstructure of A36/50mm thick ES weld metal deposited by AS 521 Cr-Mo alloyed wire :at A) fusion line, B) 1/4 width of weld metal, and C) centerline of Weld #33B-1.

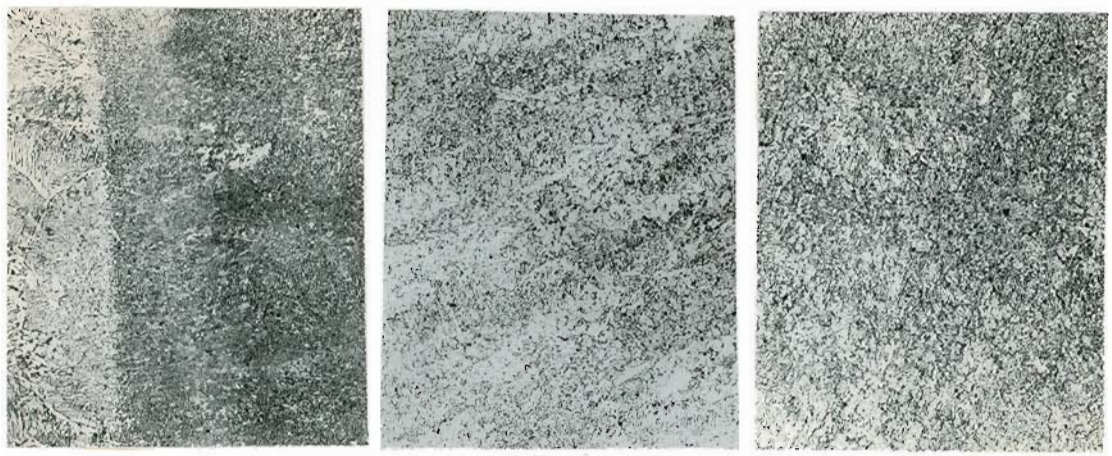

A. B. C.

Fig. 38-c Typical microstructure of A36/50mm thick ES weld metal deposited by TW8544 Ni-Mo alloyed wire at A) fusion line, B) 1/4 width of weld metal, and C) centerline of weld #53.

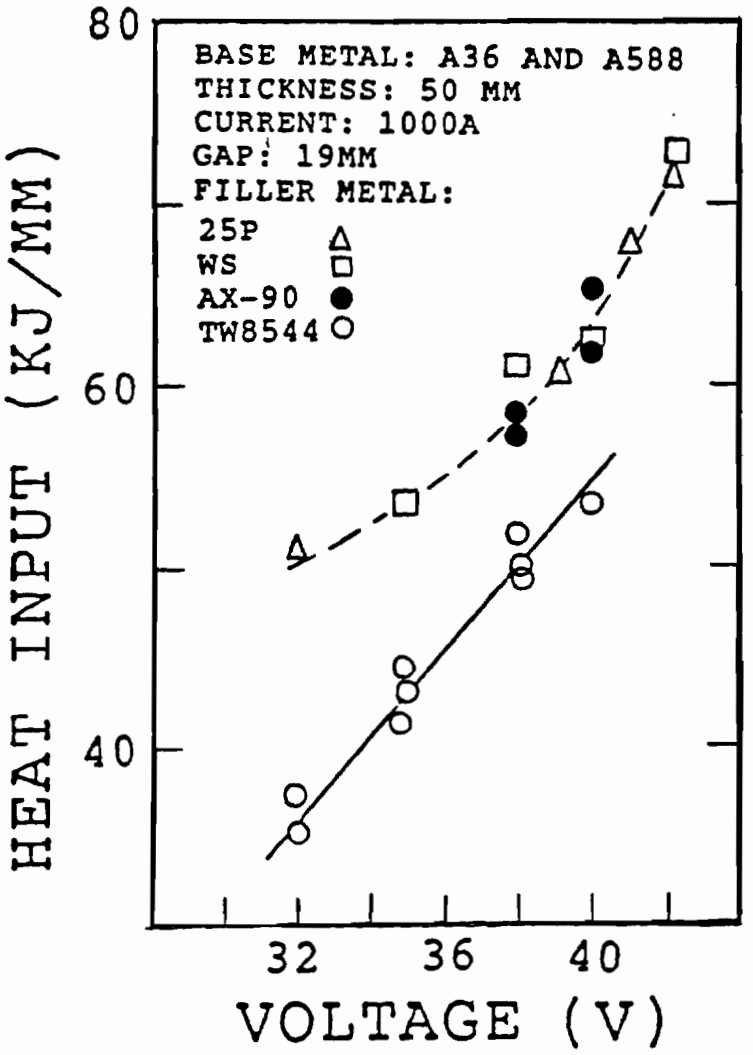

Fig. 39 Comparison of tubular (TW8544) and solid (25P, WS, AX90) filler metals on heat input of steel ES weldments.

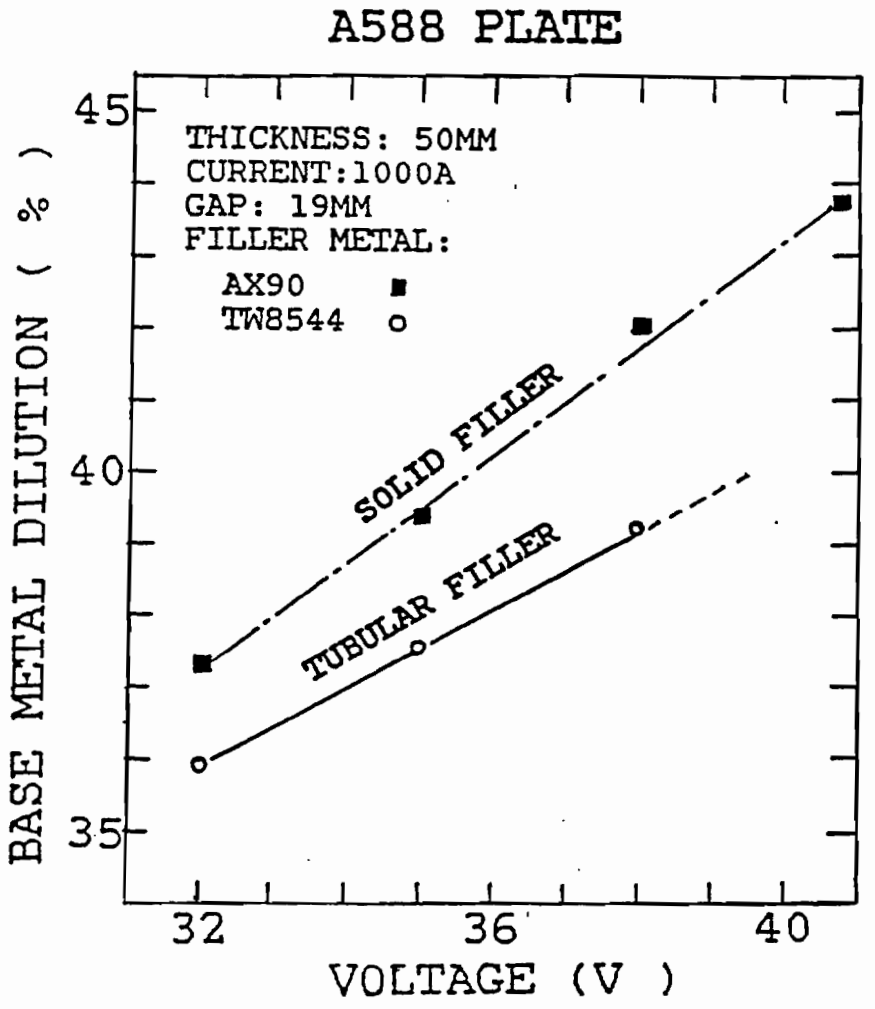

Fig. 40 Effect of tubular filler metal on base metal dilution of ES welds deposited on A588 plates

same current/voltage settings, the tubular wire deposition prevented excessive base metal dilution. This is rather important for alloying additions, because a higher content of alloying elements can be retained in the weld metal.

4) With identical welding parameter settings, the tubular filler metal weld resulted in a higher form factor (Fig. 41). This ensured that the welding speed could be increased without risk of hot cracking. Hence, in the narrow-gap ESW of A36 and A588 steels deposited by the metal powder-cored tubular wire, the recommended optimum current and voltage were 1100A/35V for 50mm welds and 1300A/35V for 76mm welds,(instead of 1000A/38V and 1100A/40V in the solid wire narrow-gap ESW).

E. HAZ APPEARANCE

A large HAZ was a typical feature of the electroslag weldments (Fig. 42). The HAZ includes the HAZ-1 and HAZ-2, where the former is the grain growth region and the latter is the grain refined region. Strictly speaking, the exact demarcation between these two regions was often not clearly definited. However, for a given base metal, the ratio of HAZ-1 and HAZ-2 can be considered always same regardless the difference in the thermal history experienced. Therefore, the measurement of full HAZ size was used in this investigation to study the thermal history of welding cycle.

The data on the HAZ size measured from a variety of 50mm and 76mm thick welds are plotted in Figures 43 and 44 respectively. Surprisingly, in these plots,little trend could be found to support the well-

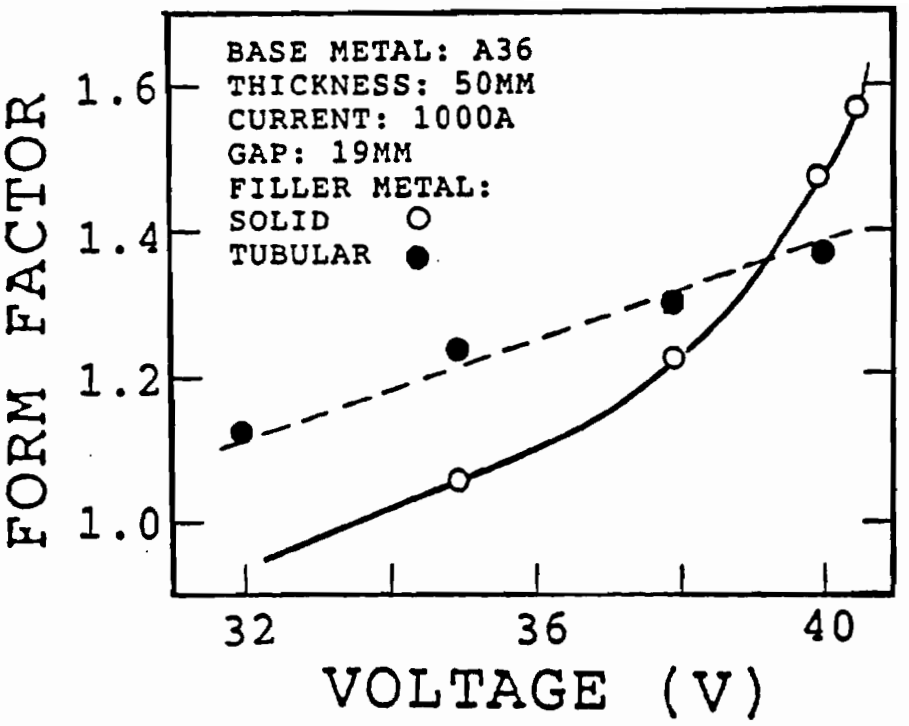

Fig. 41 Effect of tubular filler metal on the form factor of A36 ES welds

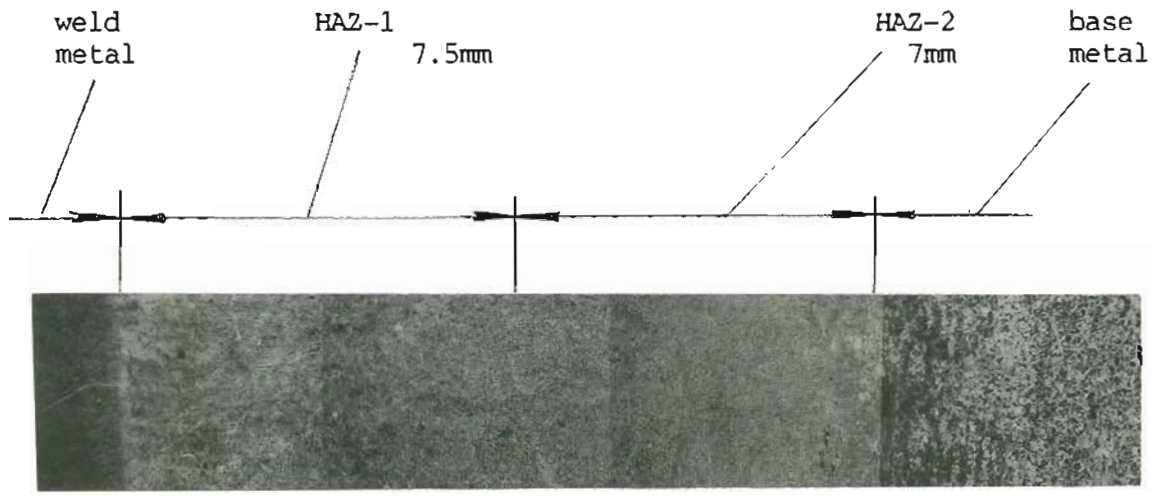

Fig. 42 Typical HAZ morphology of A36 ES welds deposited With 25p filler metal. (Weld # 5B-2)

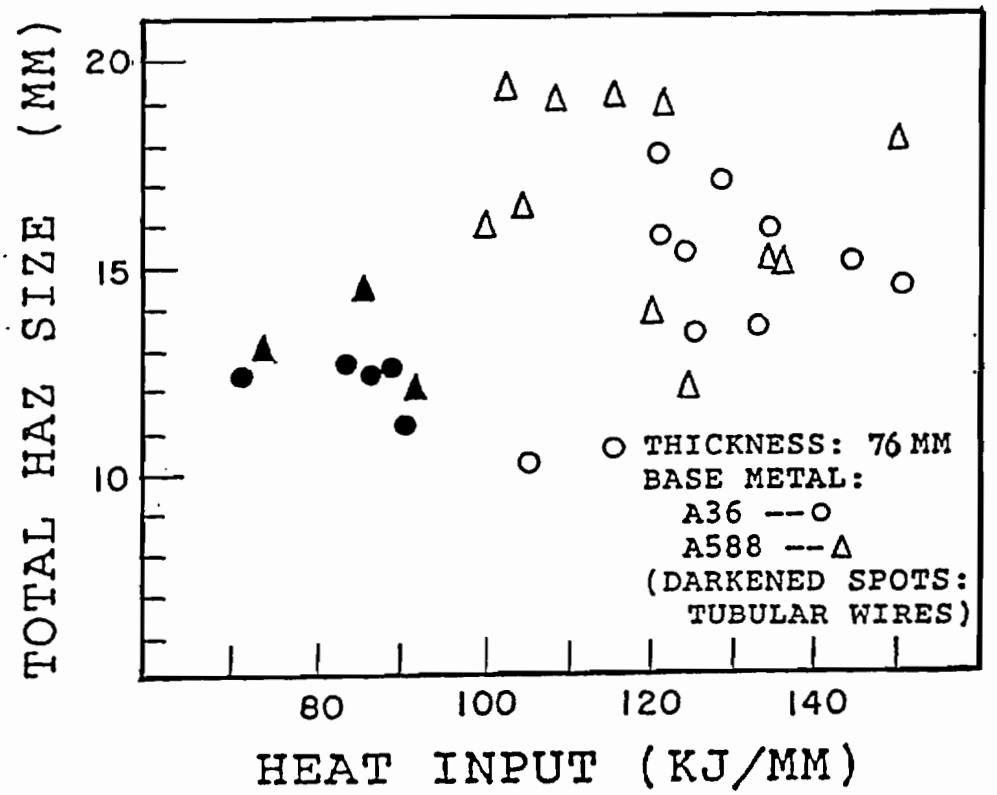

Fig.43 The HAZ size of various 50mm A36 and A588 ES welds made with different heat inputs.

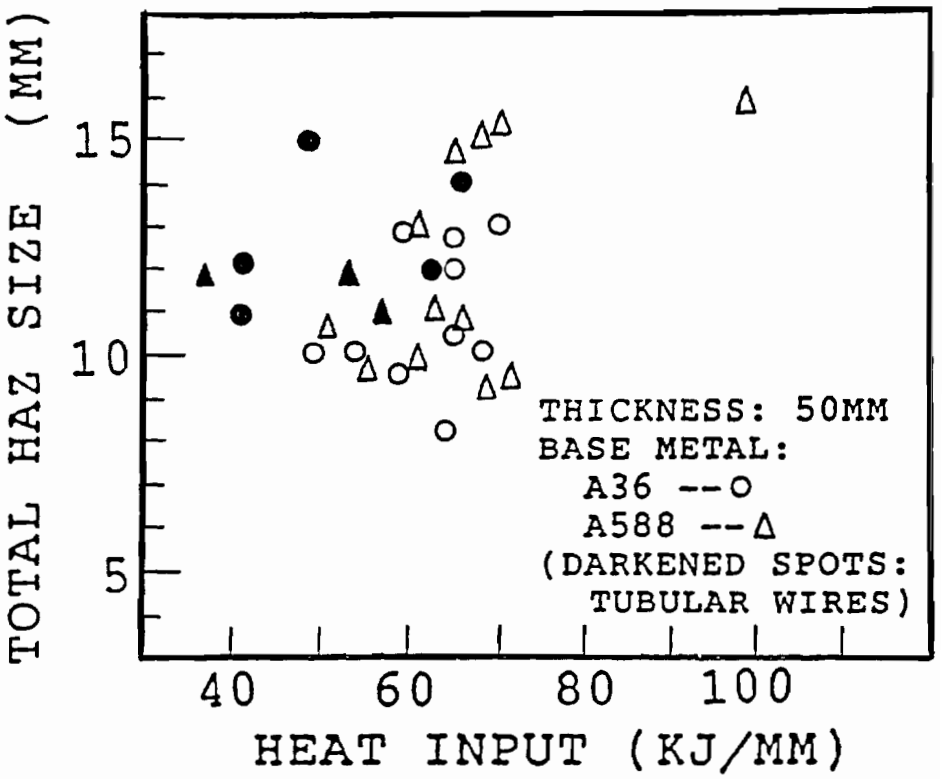

Fig. 44 The HAZ size of various 76mm A36 and A588 ES welds made with different heat inputs

known assumption between the HAZ size and the heat input of welding process. Even at the same heat input level, great scattering in the HAZ size was not a rare case at all. Obviously, those data left a tough question to be pondered.

F. MECHANICAL PROPERTIES

HARDNESS LEVEL

Weldments deposited with 25P and WS solid wires whose chemical compositions matched those of A36 and A588 base metals respectively, displayed quite close hardness levels in both the weld and base metals, as typically shown in Fig. 45. In general, excessively overmatched hardness in the weld metal was not desired, because a great disparity of strength level between the weld and base metals could make the fusion line sensitive to failure.

Regarding alloying additions to the weld metal, obtaining high CVN toughness rather than strength was surely the major concern. In comparison with the hardness of the base metal, the Cr-Mo addition, due to its great hardenability, raised the weld metal hardness for more than the Ni-Mo addition (see Fig. 46, 47). Using TW8544 filler metal, the maximum hardness values of A36 and A588 weld metals were HRB 90 and 95 respectively, which were still close to those of base metals (HRB 84 and 90) and considered acceptable.

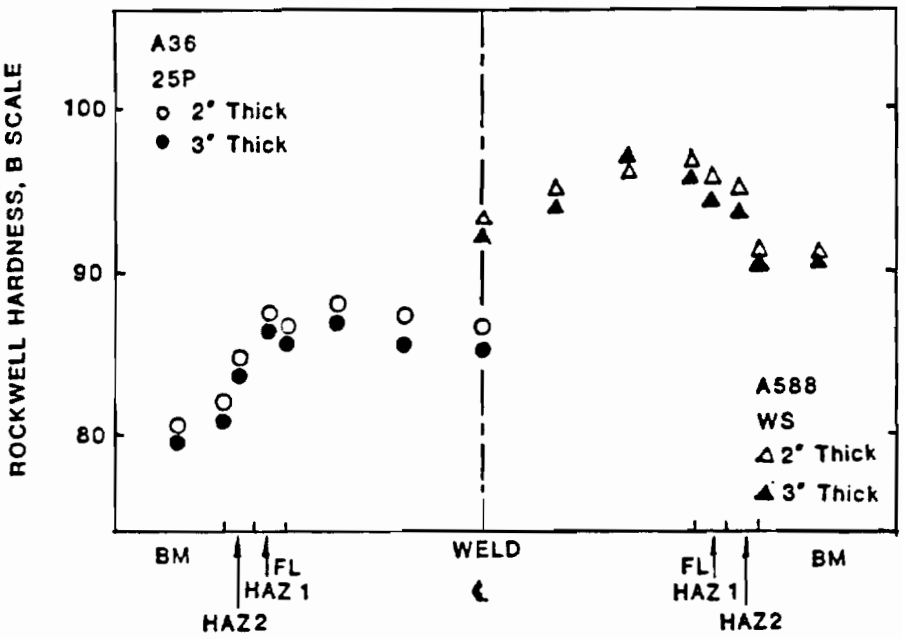

Fig. 45 Hardness traverse across A36 and A588 steel ES welds deposited by mild steel wires.

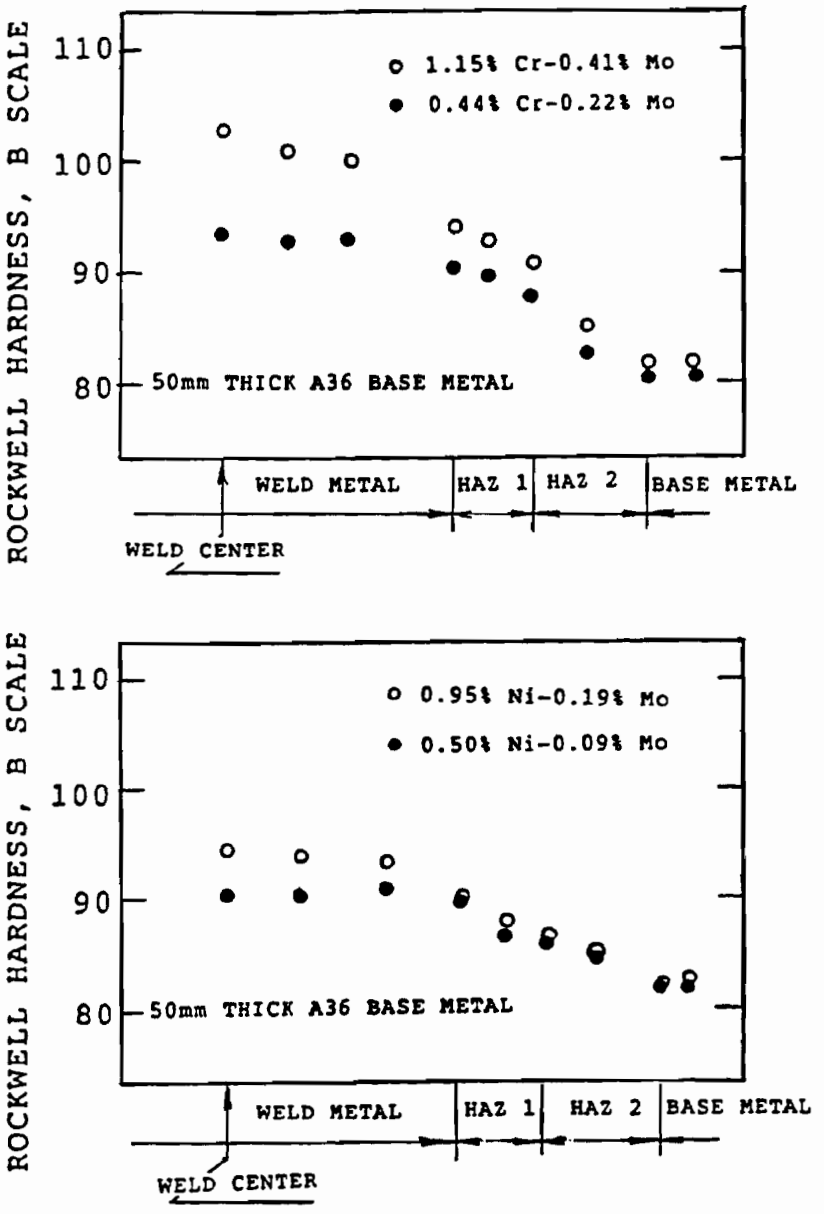

Fig. 46 Hardness traverse across A36/ 50mm ES welds deposited by a) Cr-Mo alloyed wires, and b) Ni-Mo alloyed wires.

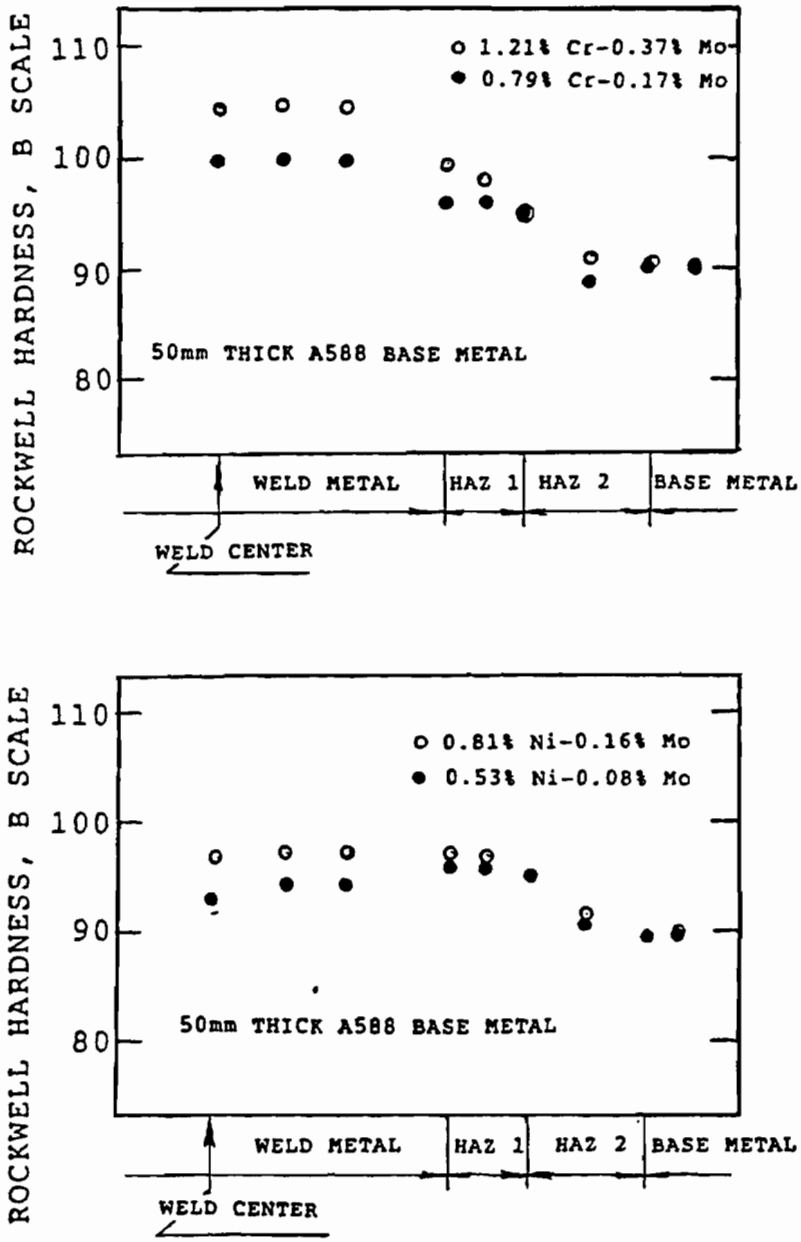

Fig. 47 Hardness traverse across A588/ 50mm Es welds deposited by a) Cr-Mo alloyed wire, and b) Ni-Mo alloyed wire.

2. CHARPY V-NOTCH TOUGHNESS

The experimental data of CVN impact energy clearly demonstrated the contribution of different filler metals. Fig. 48 shows that the Cr-Mn-Mo alloyed weld metal had very disappointing toughness, while the Ni-Mn-Mo alloyed weld metal exhibited greatly improved toughness. Based on the difference in weld morphology, it follows that the deterioration in toughness of the weld metal which contained more than 1.1%Cr and 0.4%Mo was attributed to the bainitic matrix. A substantial improvement in the weld metal containing more than 0.9%Ni and 0.2%Mo was brought about by the increase in the fine and interlaced acicular ferrite substructure. Fig. 49 and 50 display the improvement of CVN toughness corresponding to the increase in the weld metal Ni-Mo contents in 50mm thick A36 and A588 welds. In these plots, the data in the far left came from the welds deposited by the mild steel electrodes, Hobart 25p, and Linde WS. Welds deposited with the Ni-Mn-Mo alloyed tubular wire (TW8544) had the best weld metal CVN toughness by virtue of acicular ferrite predominant microstructures.

AWS code D1.1 set a minimum CVN toughness for ES weldments of 20J at -180C (15 ft-lb at 00F). Usually, with the narrow gap technique, 50mm-thick mild steel welds could just meet this qualification level, while 76mm mild steel welds failed. But, the corresponding CVN toughness for Ni-Mn-Mo alloyed (using TW8544 filler) weld metal ranged between 30 to 50J, which was superior to that of both A36 and A588 base metals.

A series of typical CVN toughness transition curves are presentedin Fig. 51 to 56. In those plots, the representations of weld

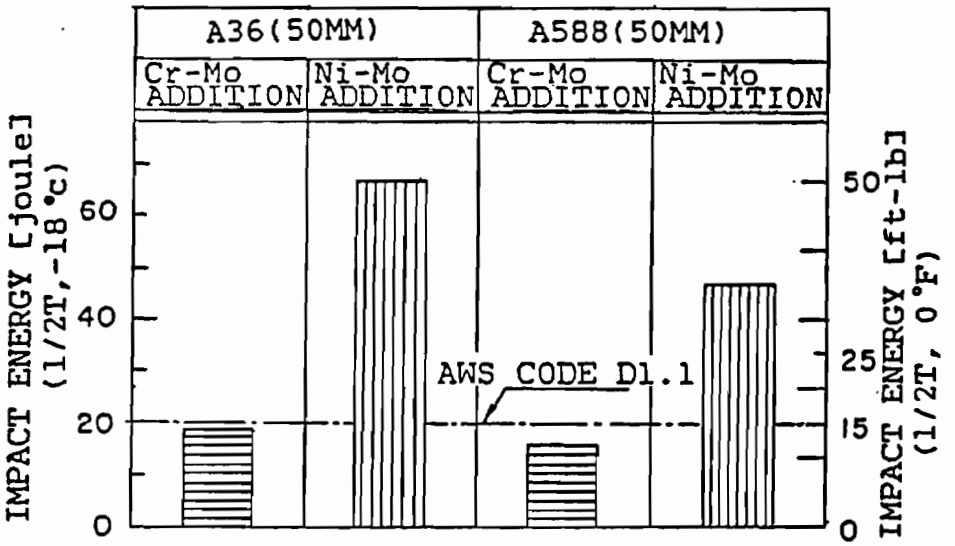

Fig. 48 Comparison of CVN toughness between weld metal containing Cr-Mo and Ni-Mo steel filler metal.

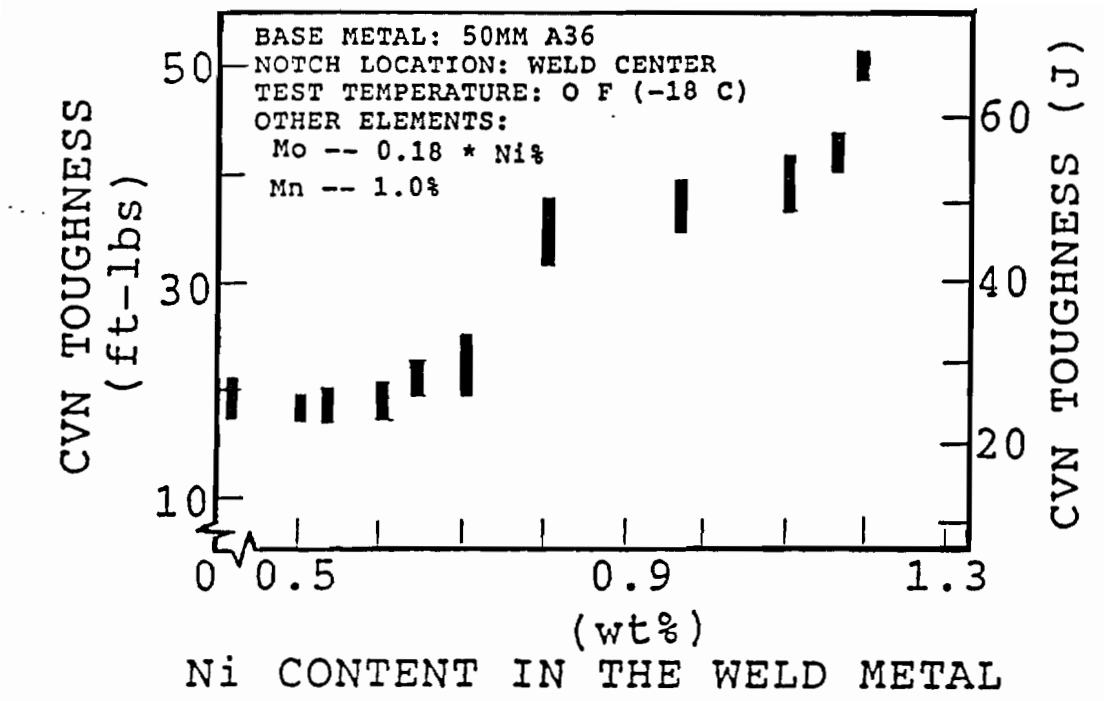

Fig.49 CVN toughness of ES Welds Deposited on 50mm Thick A36 Steel as a Function of Ni Content.

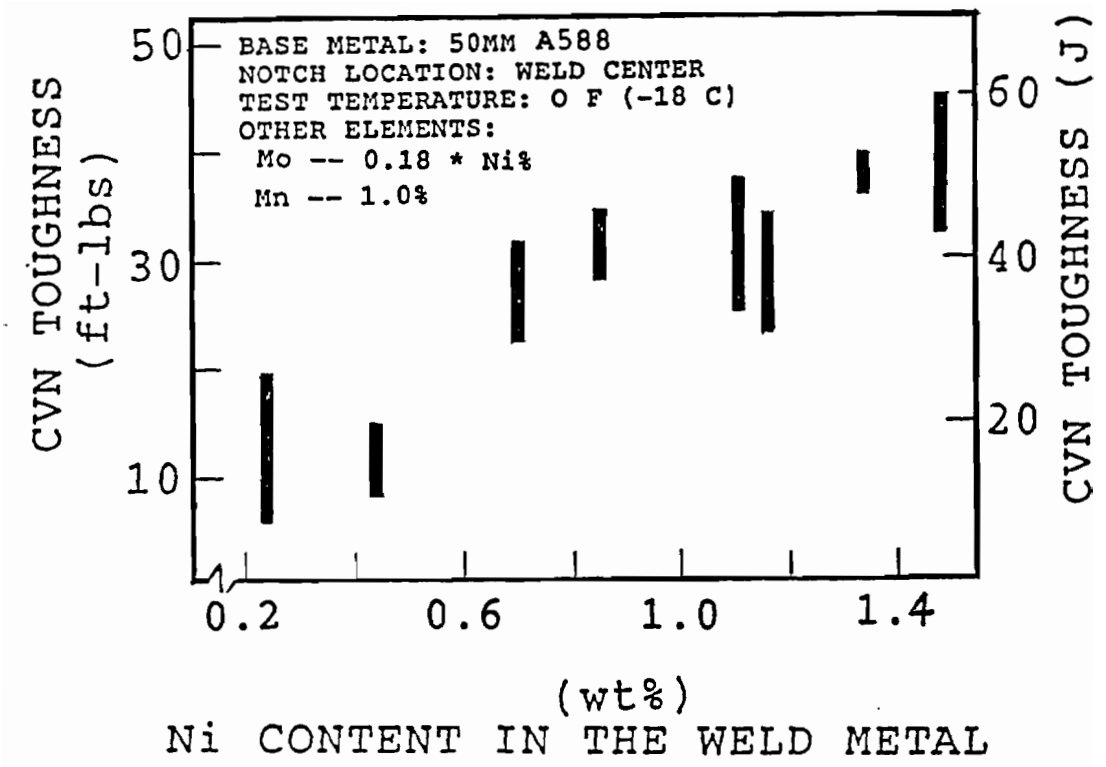

Fig. 50 CVN toughness of ES welds Deposited on 50mm Thick A588 Steel As a Function of Ni Content

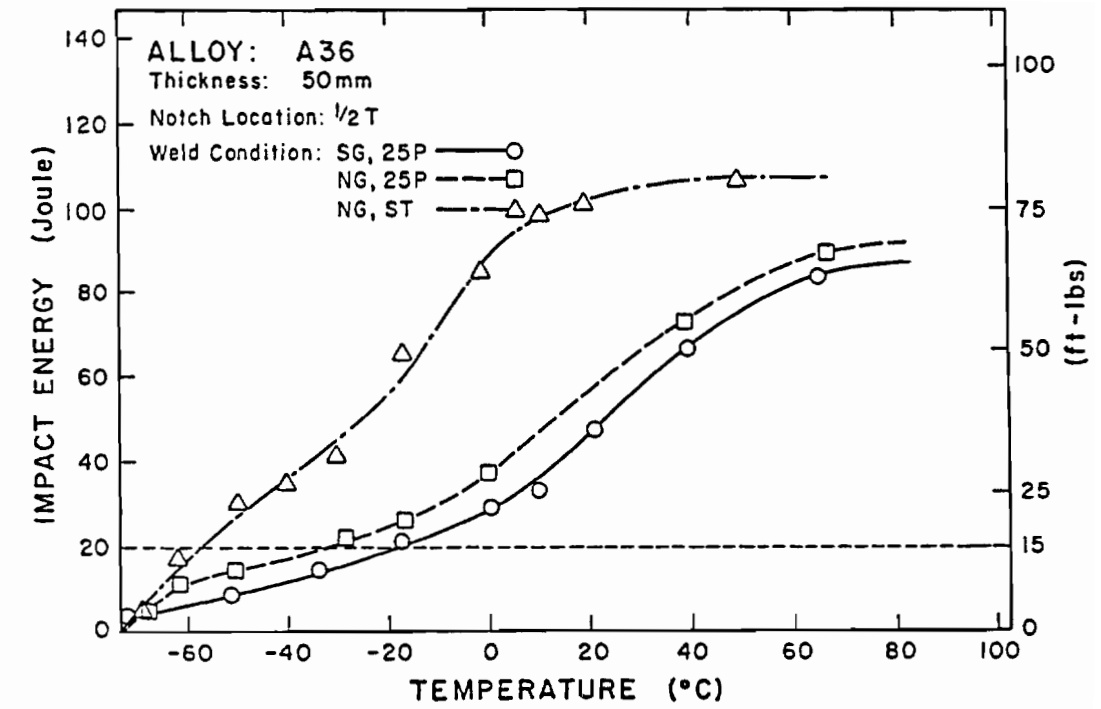

Fig. 51 CVN transition curves for 50mm thick A36 ES wled metals using different welding conditions (notched at 1/2 thickness location of weld center)

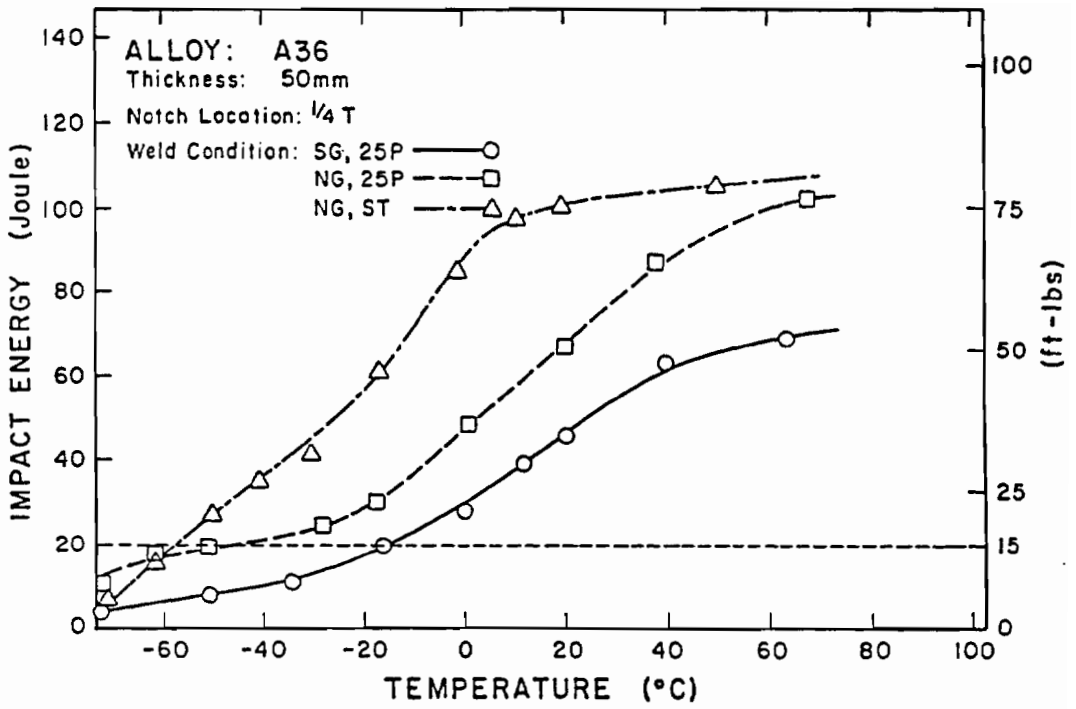

Fig. 52 CVN transition curves for 50mm thick A36 ES weld metals using different welding conditions. (notched at 1/4 thickness of weld center)

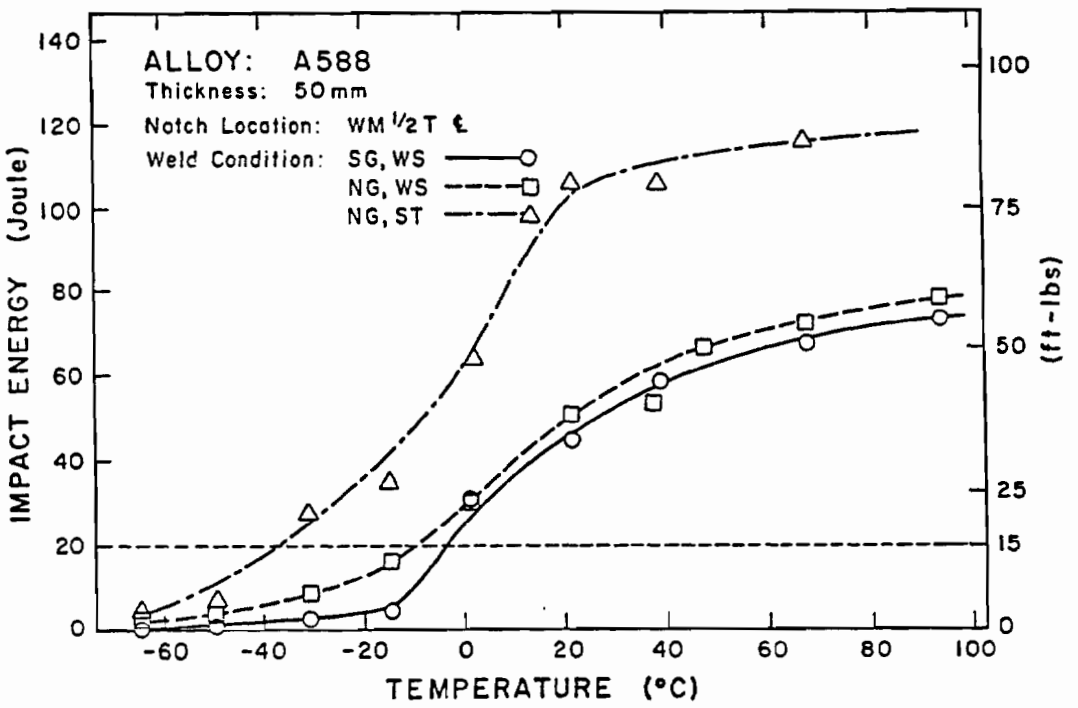

Fig. 53 CVN transition curves for 50mm thick A588 ES weld metals using different welding conditions. (notched at 1/2 thickness of weld center)

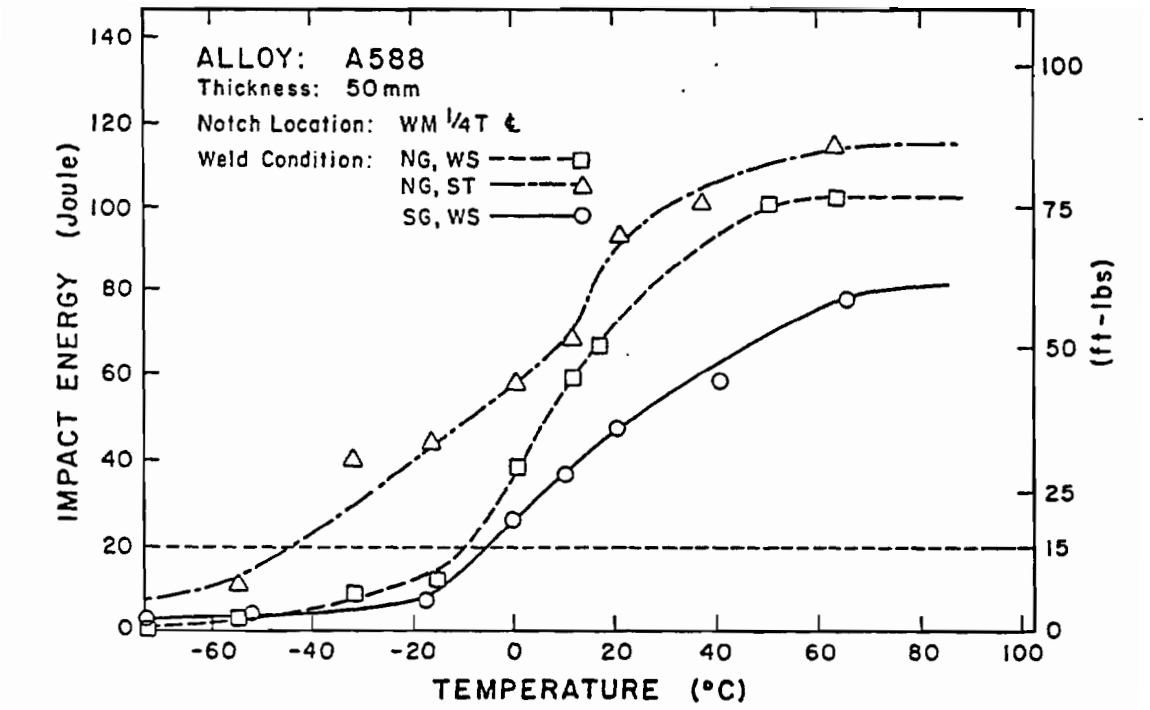

Fig. 54 CVN transition curves for 50mm thick A588 weld metals using different welding conditions. (notches at 1/4 thickness of weld center)

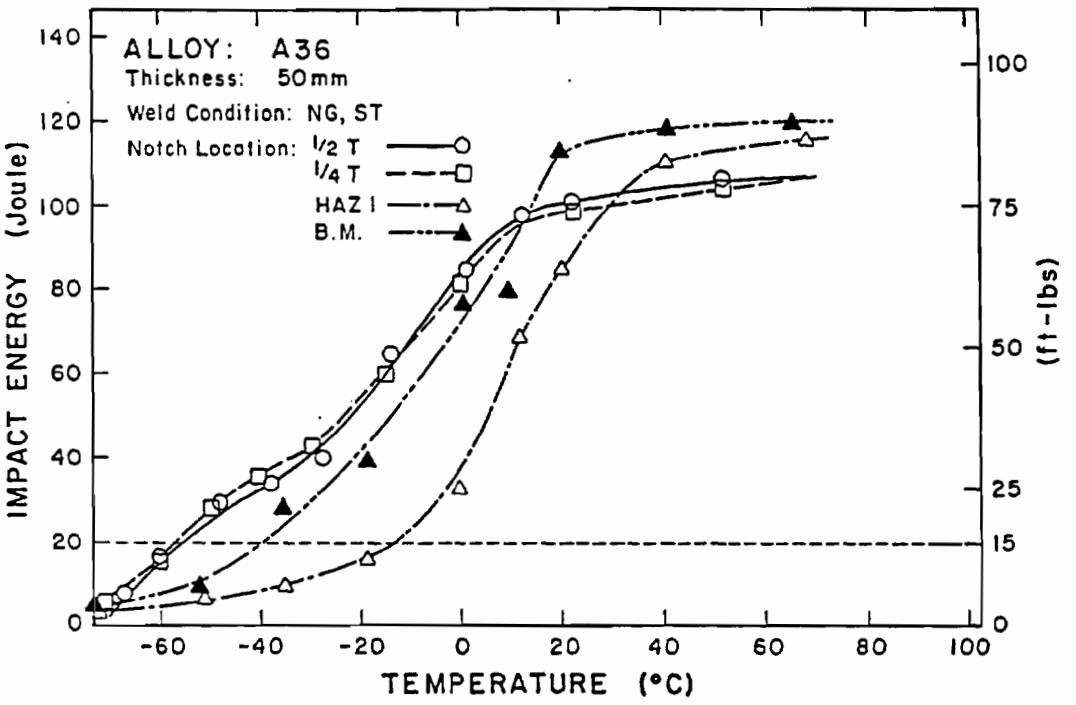

Fig.55 CVN transition curves for different notch locations of 50mm thick A36 ES welds deposited by TW8544 wire.

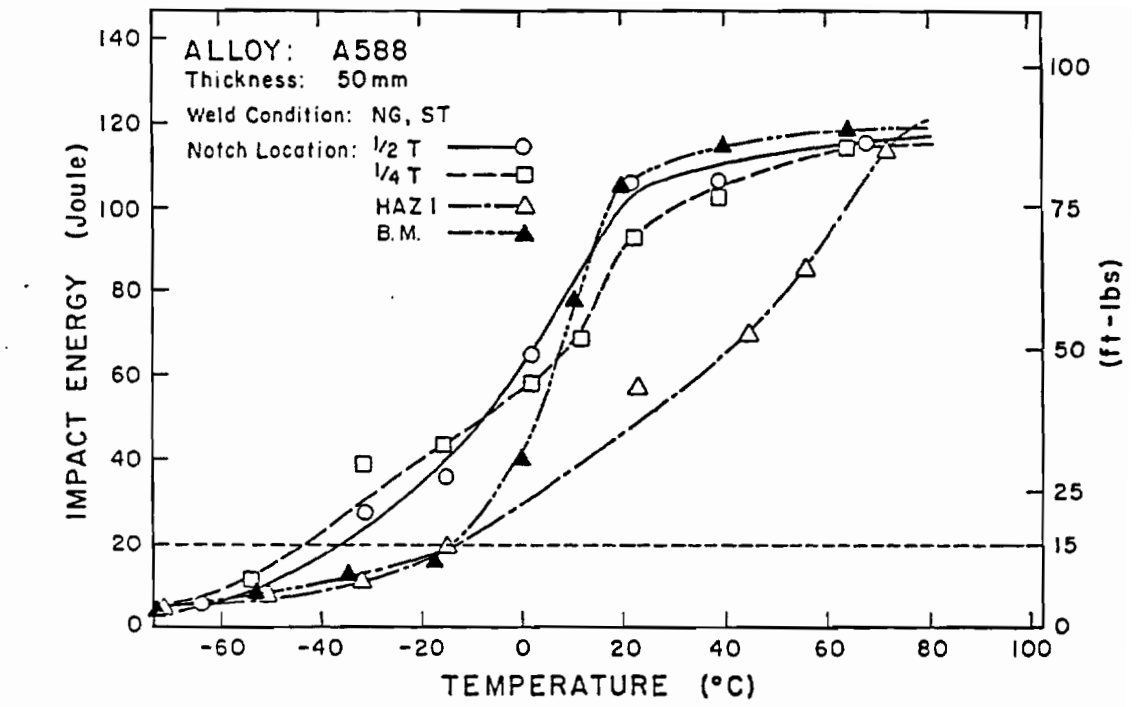

Fig. 56 CVN transition curves for different notch locations of 50mm thick A588 ES welds deposited by TW8544 wire

conditions were simplified as following: SG--31mm joint gap, NG--19mm joint gap, 25p--deposition with Hobart 25p wire, WS--deposition with Linde WS wire and ST--deposition with TW8544 wire. Upon comparing the fractographs (Fig 57-a and 57-b) and the CVN transition curves, the Ni-Mo-Mn alloyed weld metals not only exhibited good resistance to low temperature cleavage, but also displayed acceptable upper shelf CVN energy. For the mild steel ES weld metal, toughness at the half-thickness(centerline) location was usually much worse than for the quater thickness (centerline). Ni-Mo additions significantly made both the hardness and CVN toughness values of the entire weld more uniform. Figures 55 and 56 demonstrate that the transition curves for CVN toughness tests of both halfthickness and quater-thickness locations in the Ni-Mo containing weld metal overlapped. Practically, considering the reliability of electroslag weldments in different geographical climate zones, Figure 58 displays the test temperature range at which the welds failed to be qualified to 20J.

CVN toughness data from HAZ-1, while improved by reduced heat input was not equivalent to the weld metal. This phenomenon was related to the thermal transfer pattern in ES weldments as well as the location of the Charpy V-notch in the HAZ specimens. Both will be discussed later. Generally speaking, the reduction in welding heat input brought about by the tubular wire deposition was beneficial to the improvement of HAZ toughness, if allother factors remained constant.

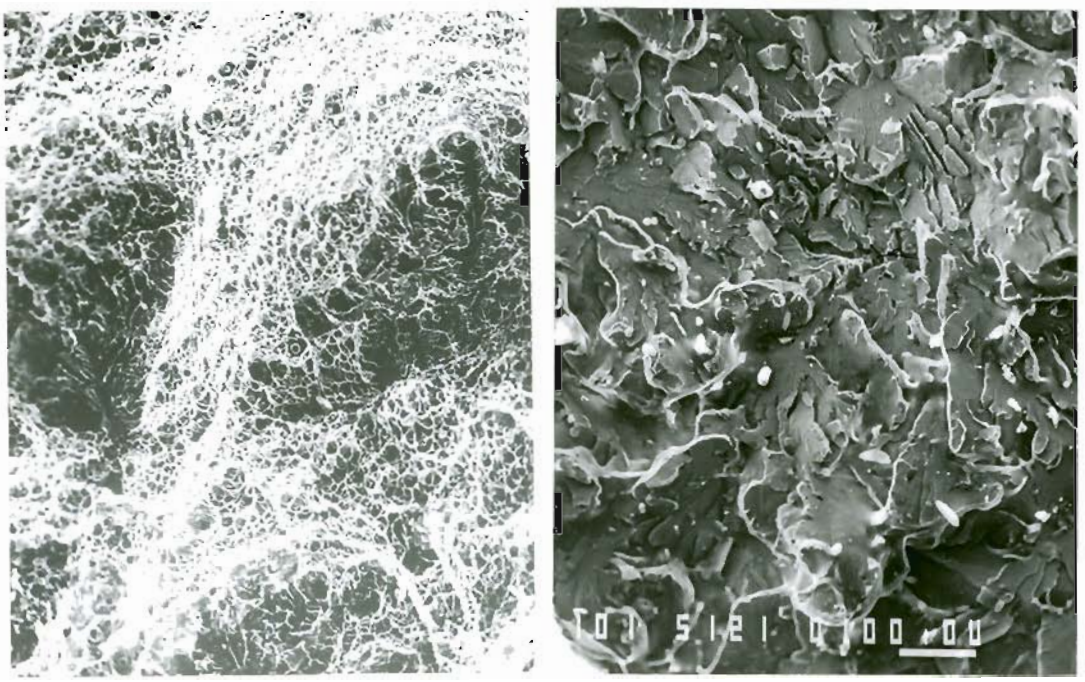

a. b.

Fig. 57 CVN fracture surfaces of 50mm thick A588 ES weld metals deposited with a) TW8544 filler metal (Weld #M168), and b) mild steel filler metal (Weld #M154).
[Specimens were tested at -18 C (0 F)]

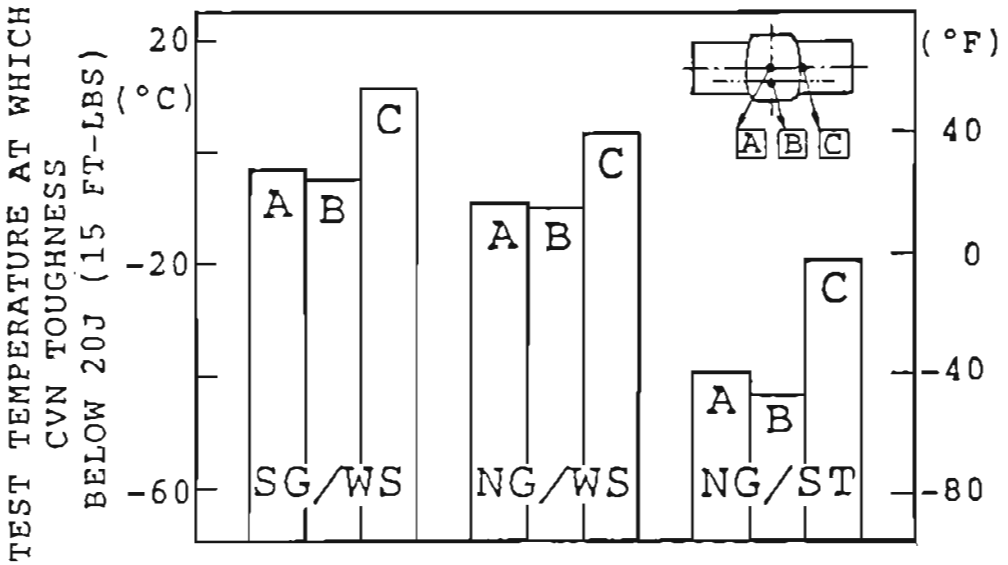

Fig. 58 Minimum test temperatures at wich the CVN toughness of 50mm A588 ES weldments is 20J (15 ft-lb).

3. PLANE STRAIN FRACTURE TOUGHNESS

In this study, most tests of the A36 specimens failed to meet the criteria of E-399 due to their low yield stress, high ductility and limited thickness. However, some tests of A588 specimens were valid. In view of the similarity of microstructures obtained in A36 and A588 welds, a similar trend for the K1c toughness of A36 welds could be inferred from those of the A588 welds.

Results indicated that, for A588 base material, the K1c toughness values of mild steel weld metals were only 55 to 60 MPa-$m^{\frac{1}{2}}$, which was far below that of the base metal, 80 MPa-$m^{\frac{1}{2}}$, while the K1c toughness of Ni-Mn-Mo alloyed weld metals (with TW8544 filler) reached 87MPa-$m^{\frac{1}{2}}$. In fact, the weld metal K1c toughness data showed a similarity to the CVN impact toughness data as shown in Fig.59. If more valid K1c data were available, a rough derivation for the empirical formula between CVN and K1c toughness of ES weld metal would be possible.

The superior fracture resistance of Ni-Mo alloyed A588 weld metal was also demonstrated by the following phenomenon. During both fatigue precracking and subsequent testing, specimens cut from mild steel welds frequently suffered intermittent low load crack propagations, which were usually considered as an unwanted brittle characteristic. But, in alloyed weld specimens, this phenomenon did not occur.

In this investigation, the precracks of HAZ-1 specimens inevitably covered certain portions of HAZ-2, since the fusion boundaries were not perfectly straight through the full thickness. Though, strictly speaking, these K1c values did not reflect the actual behaviors of

HAZ-1 itself, they stood for some situations more close to the real practice of large structural components on bridge structures. An engineering crack often initiates at the weakest site. And, before final failure, it is restrained by surroundings which may be of different toughness levels. Hence, the K1c data obtained from HAZ specimens still provides certain beneficial information qualitatively. For example, in Figure 60, the nominal HAZ-1 K1c toughness data of 76mm thick A588 welds clearly exhibited an increase with a decrease of heat input.

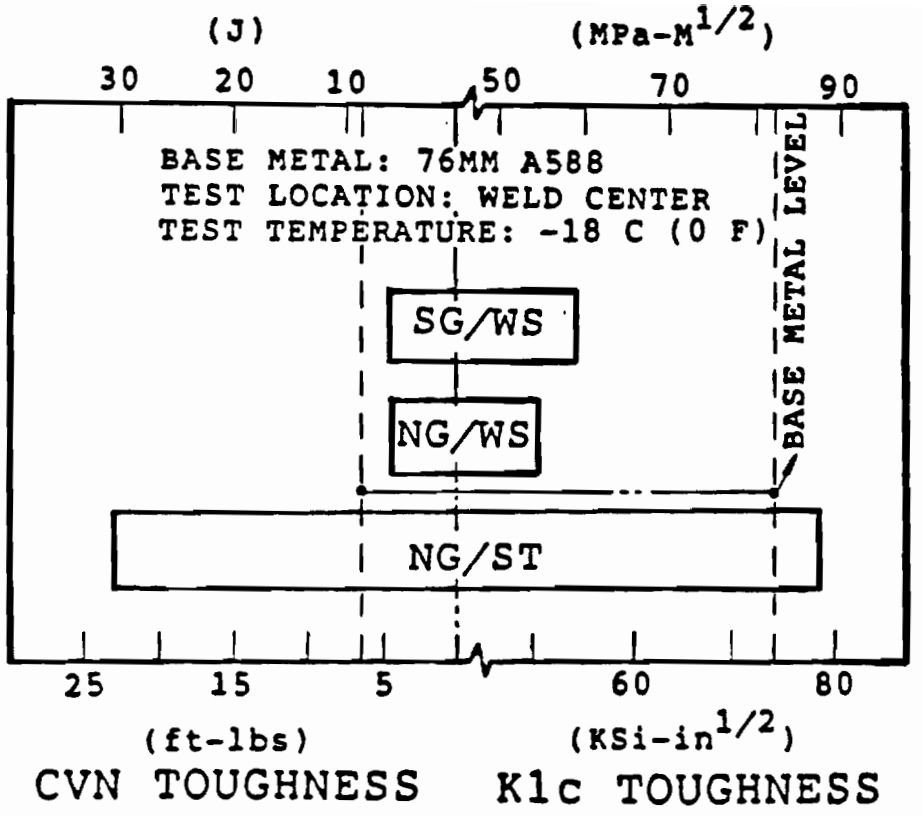

Fig. 59 The CVN and K_{1c} toughness levels of 76mm A588 weld metals at -18°C (0 °F)

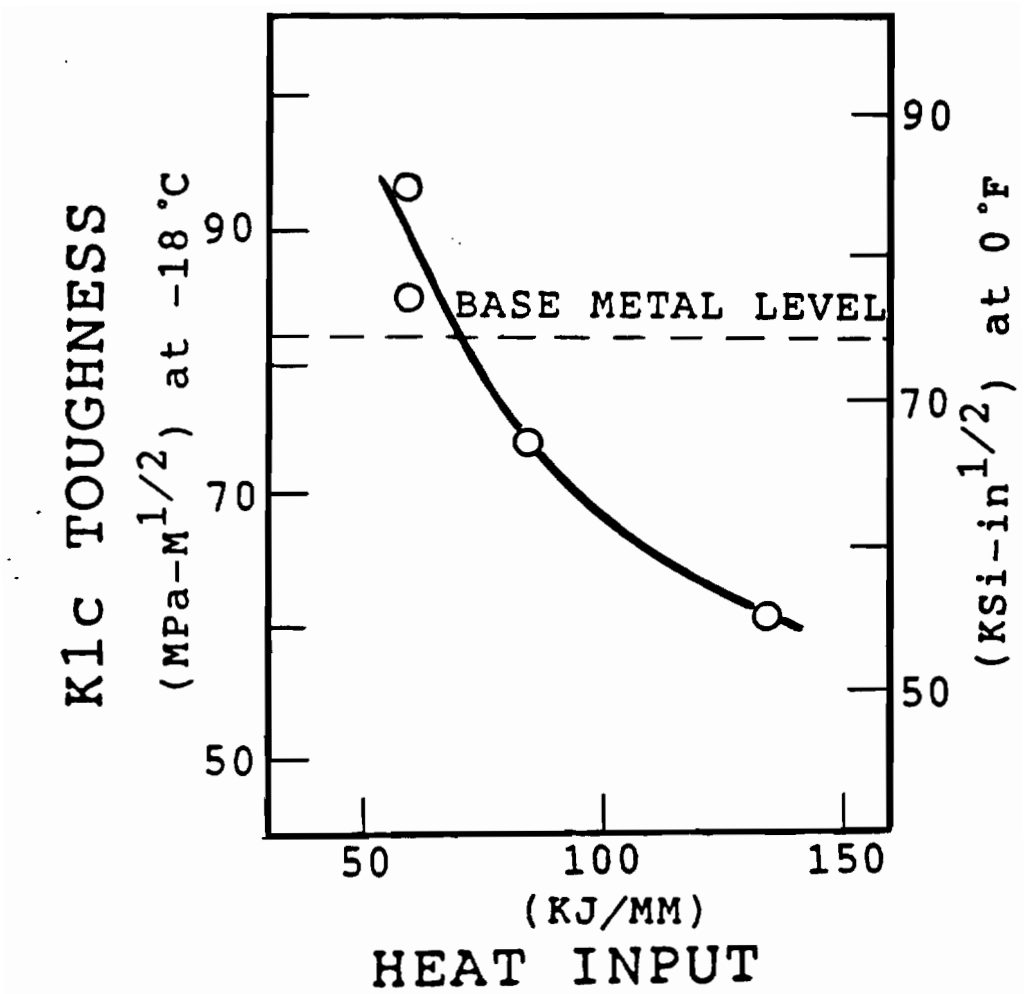

Fig.60 Nominal HAZ-1 K_{1c} toughness of 76mm thick A588 ES welds as a function of heat input.

V. DISCUSSION

A. CORRELATION BETWEEN SOLIDIFICATION SUBSTRUCTURES AND AS WELDED MORPHOLOGIES

1. FORMATION OF SOLIDIFICATION STRUCTURES

The primary solidification mode strongly depended upon the temperature gradient (G), the growth rate (R), the solute content and the crystallographic orientation of the base metal at the weld/ base metal interface, as expressed schematically in Fig. 4 [30]. Attention is directed to the transition from cellular dendritic to columnar dendritic growth. A high form factor resulted in an early transition, while a low form factor made this transition occur closer to the central portion of the weld. To explain this phenomenon, two welds with the same weld travel speed but different form factors were studied. The sketch of the weld pool in Fig. 61 compared the results at the same percentage of weld width. A mathematical derivation explains it more concisely. Because

$$V_{w1} = V_{w2} = V_w,$$
$$(f.f.)_1 > (f.f.)_2$$

where V_w is the weld speed and (f.f.) is the form factor, and from Fig. 61

$$\theta_1 < \theta_2 \qquad \text{—(3)}$$

where d is the dendrite arm spacing, G is the thermal gradient, R is the growth rate, θ is the angle between the maximum thermal gradient and weld direction, and A and m are constants. This also coincided with the result observed in Fig. 14.

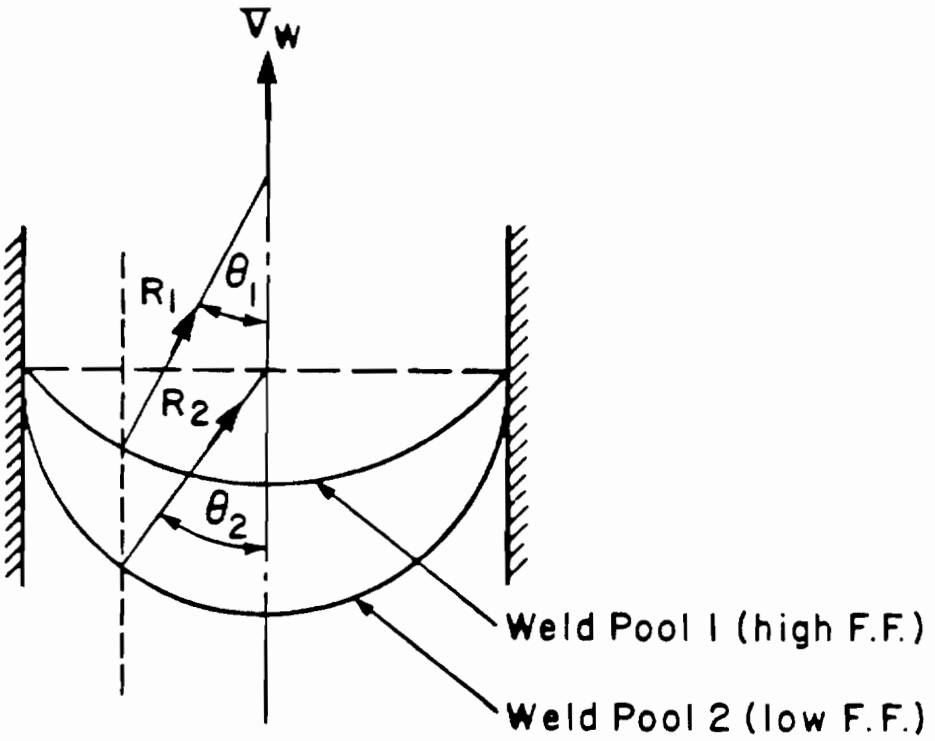

Fig. 61 Variation of weld pool shape with different form factors.

Thus, $R_1=V_w\cos\theta_1$,

$R_2=V_w\cos\theta_2$,

and $R_1>R_2$ ---(4)

From Fig. 18

$d_1>d_2$ ---(5)

and from Eq.(2)

$d=A/(GR)^m$,

then, $A = d_1(G_1R_1)^m=d_2(G_2R_2)^m$ ---(6)

From the above inequality equations (4) and (5),

$G_1<G_2$ --(7)

Therefore,

$G_1/(R_1)^{1/2} < G_2/(R_2)^{1/2}$ --(8)

It is clear, according to the correlation given by Fig. 4 that, at the location corresponding to a given percentage of the weld width, a high form factor was more prone to induce columnar dendritic growth than a low form factor, which means that case 1 had a smaller proportion of cellular dendrites, while cases 2, 3 and 4 in increasing order, had a greater proportion of cellular dendrites. Furthermore, during the solidification of low carbon steels, the peritectic reaction (Fig. 62) is very important. The nominal carbon contents of A36 and A588 steels and the carbon contents of diluted weld metal were all around 0.17%. This means that the initial solid phase, during the primary solidification of these welds, is delta-ferrite, followed by the peritectic reaction:

1) liquid -> delta-ferrite,

2) liquid + delta-ferrite -> austenite.

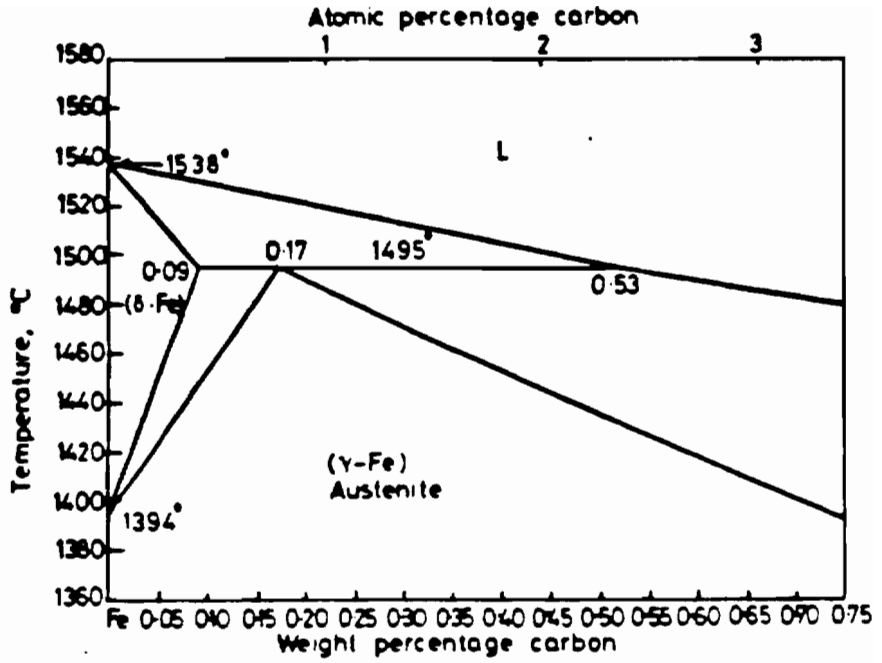

Fig. 62 Left corner of Fe–C phase diagram.

The prior solidified cellular dendrites are deltaferrite and have a lower solute content than the mean value of the weld metal. Most of the extra solutes are rejected to the tips of the cellular dendrites. Towards the interior of the weld, the solidification structure changes to columnar dendrites, composed of delta-ferrite cores and partial austenitic outer layers. Fig.63-a is a sketch of this feature.

Another important phenomenon was the columnar dendritic-equiaxed dendritic transition. As mentioned early, in most arc welding processes, natural transitions from the columnar dendritic to equiaxed dendritic growth are comparatively rare [37], during the primary solidification in welds. Because of the severe thermal condition in steel weld pools, the generation of nuclei and their survival are difficult to achieve. However, in ESW which is associated with a very high heat input, the situation is rather different from the others. As seen in figure 4, the columnar dendritic to equiaxed dendritic transition could only occur under the conditions of 1) low ratio of thermal gradient to solidification rate (G/R), and 2) high percentage of solute (impurities or alloy elements) in molten metal. From Figures 19 and 20, It is seen that there was a substantial increase of primary dendrite arm spacing, d, in the area near the weld center of case 4. This might be caused by changing the thermal flow in the deepened weld pool where the dispersion of heat near the weld center was increasingly difficult. The solidification rate (R) near the weld center became identical to the weld travel speed (V_w). If high weld speeds (case 4) were applied, R became

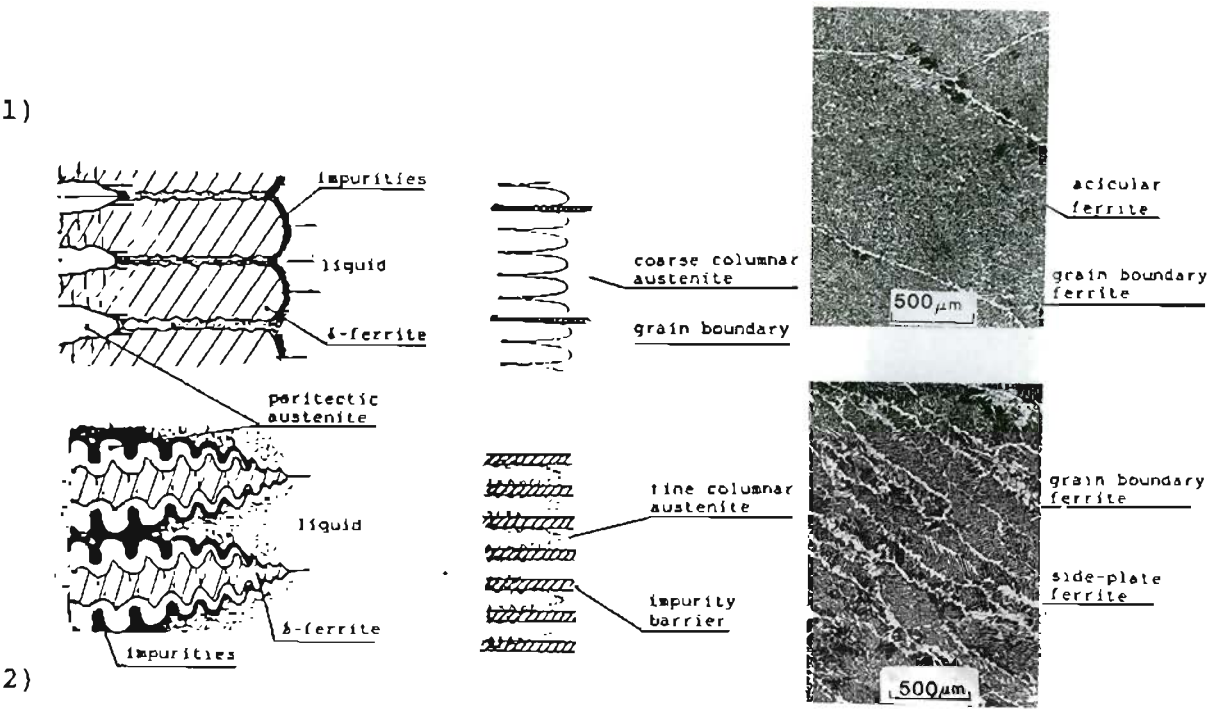

a) b) c)

Fig. 63 Variation of morphology during solidification and subsequent transformation of 1) the cellular dendritic region, and 2) the Columnar dendritic region for

a) primary solidification morphology,

b) austenite grain structure, and

c) room temperature microstructure.

relatively high as well. From Eq. (5), a large d and a high R at the weld center should inevitably lead to low G, because of Eq.(2):

$$d(GR)^m = \text{constant}.$$

Thus, (G/R) was rather small in the center region of a case 4 weld. In addition, the accumulation of segregated solutes around the weld center would also help to shift the growth mode upwards in Fig. 4. All those effects would make the transition from columnar dendrites to equiaxed dendrites possible.

Owing to the appearance of the central equiaxed structure, impurity segregations would be dispersed to a relatively large central area instead of a narrow line. In this case, the last liquid to solidify formed the liquid films that: (1) remained at the interfaces between the equiaxed dendritic region and the columnar dendritic region, and (2) extended to the interfaces of columnar dendrites. Those locations contained a high content of impurities. Due to the relatively low transverse strength of columnar dendrites [91], the contractional strain could cause cracking in those finally-solidified interfacial sites. This is consistent with the radial cracking in case 4 welds. After solidification, the equiaxed dendritic shaped austenite would continue to grow until reaching the interface containing an impurity barrier between the prior equiaxed dendritic and columnar dendritic regions.

If alloying elements were added into the weld metal, the solidification mode could change further. When Ni-Mo-Mn or Cr-Mo-Mn alloyed filler metals were deposited into the weld pool of A36 and

A588 steels, even for the weld with a form factor value which usually corresponded to case 2, an equiaxed dendritic region was found at the weld center. Detail discussions are in the later section of this chapter.

2. FORMATION OF AUSTENITE

On further cooling, delta-ferrite becomes unstable and transforms into austenite. In the cellular dendritic region, austenite nuclei forms at the interfaces between cellular dendrites and the lateral growth of austenite nuclei follows. In the columnar dendritic region, direct boundary migration of existing austenite occurs.

FCC austenite has lower solubilities of S, P, Si and O than BCC delta-ferrite [92]. In the cellular dendritic region, a low concentration of these solutes can be expected [30]. According to the " impurity drag theory " of boundary motion [93], the barriers to austenite growth in this matrix are much less. Thus, in the cellular dendritic zone, after delta-ferrite disappears, austenite can more easily grow laterally in the direction transverse to cellular dendritic interfaces with the motion of grain boundary allotrimorphs [94].

The columnar dendrites have a relatively high concentration of impurities at their interfaces. On peritectic solidification, the growth of austenite, which solidified directly from the liquid, should further reject impurities into the liquid. After the completion of peritectic reaction, austenite in those locations would face substantial impurity barriers. Thus, the lateral growth of austenite could not occur as easily as in the cellular dendritic region, because the resistance to boundary migration is greater. The final configuration of austenite in the former columnar dendritic region, before the proeute-

ctoid ferrite transformation, might still retain a similar morphology to that of columnar dendrite.

It is significant to point out that, on further cooling from the austenitic solidification temperature to proeutectoid temperature, interstitial carbon atoms could diffuse rapidly. However, other impurities, such as S, P, Mn and Si, still retained in their initial distributions, since significant solid state diffusion for them in austenite was unlikely.

Therefore, before the proeutectoid transformation, the morphology of weld metal is suggested as: 1) coarse columnar austenite in the former cellular dendritic region, and 2) fine columnar austenite in the former columnar dendritic region as shown in Fig. 63-b.

3. FERRITIC TRANSFORMATION

Possible weld metal transformation products in low carbon steels include grain boundary ferrite, Widmanstatten sideplate ferrite and acicular ferrite. In general, grain boundary ferrite forms between 750-1000°C by long-range diffusion. Sideplate ferrite forms between 750-600°C by the short-range diffusion. Acicular ferrite forms below 600°C, which is intragranularly nucleated ferrite. The formation of acicular ferrite has been related to the existence of weld inclusions and a large undercooling.

In order of increasing undercooling below the A3 temperature, the factors that determine the final volume fraction of the various transformation products are the nucleation rate, the growth rate, the density and dispersion of nucleation sites, the overlap of the diffu-

sion field from adjacent products and the impingement of adjacent volume and content of alloy elements. Fig. 64 is the schematic CCT diagram of carbon steel. ESW has a slower continuously cooling curve than other welding processes, and is presented as the dark line in Fig. 64.

Near the fusion boundary, the former cellular dendritic region transforms into the coarse columnar austenite grains, as mentioned before. The cellular dendritic boundaries are known to be low angle, having a lower impurity concentration than the columnar dendritic boundaries. Thus, the previous cellular dendrites and their interfaces are not very potential nucleation sites for grain boundary ferrite, when cooling below A_{c3} temperature. This implies that the nucleation of ferrite can be, to a certain degree, suppressed to a large value of undercooling in the former cellular dendritic region, i.e. the interior of columnar austenite grains. Only those boundaries of austenite grains, which were high angle, and non-coherent grain boundaries with high strain energy, are prone to forming grain boundary ferrite. The former columnar dendritic regions, however, contain fine columnar austenite grains. The interfaces of those grains has a comparatively high segregation ratio of impurities. Ferrite easily nucleates at these preferred sites with a small undercooling below A_{c3} temperature and sometimes grow to the interior of austenite grains with the growth of blocky allotriomorphs of ferrite. During this process, the solute gradient into austenite becomes much steeper, and the growing ferrite quickly decorates the austenite boundaries. Also, if the cooling situation reduces

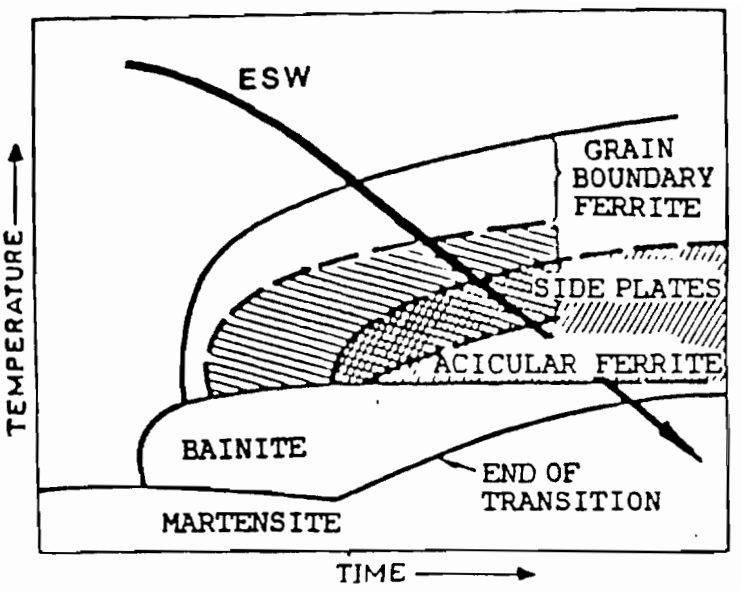

Fig.64 Schematic CCT diagram of low alloy steel weld.

the carbon diffusion rate, Widmanstatten side-plate ferrite will occur.

On further cooling, due to the co-influences of undercooling and weld inclusions, the remaining austenite matrix in both the former cellular dendritic and columnar dendritic regions transforms to acicular ferrite. Figure 63c shows the final solid state microstructure.

In case 4 welds, three dimensional dendritic growth might increase the opportunities of enclosing slag inclusions (oxides) into the gaps of dendrite arms. It would cause more inclusions distributed in the austenite grains at the weld center, as shown in Fig. 27 to 29. This may be the main reason for the formation of acicular ferrite at the weld center.

In addition, the effect of "renucleation" [32, 82, 95] should not be ignored. High form factor welds resulted in a larger variation of inclination angle of dendrite orientation as shown in Fig.14. Due to the non-bending characteristic of both cellular and columnar dendrites. The angular change had to be adjusted by certain mechanisms including the renucleation events. It was frequently observed, as shown in Fig. 13, that the previous group of dendrites stopped at the lateral side of another new group of renucleated dendrites. During the primary solidification, impurities were often rejected ahead of the solid/liquid interface. At those intersections where the renucleation events happened, the impurities would be blocked. Those high energy sites became preferred locations for the nucleation of small undercooling ferrite. Thus, the higher the form factor, the more frequent the renucleation events, the greater the generation of small under-cooling ferrite. It should be pointed out that although there were renucleation

events in the cellular dendritic region, the relatively low interfacial solute concentration did not create enough strain energy for the nucleation of grain boundary ferrite.

4. A MODELLING MORPHOLOGICAL CHANGES

Based on the above studies, a model has been suggested to explain the correlation between the primary dendritic substructure and the as-welded solid microstructure. Here, the transition from cellular dendrites to columnar dendrites and the degree of the lateral austenitic growth are two major factors dominating this correlation. Although the direct experimental evidence has not been obtained, the following model is still based on the well-accepted concept of ferrite formation.

In general, the former cellular dendritic region transforms to an acicular ferrite-rich microstructure, which corresponds to the coarse columnar grain zone. While, the former columnar dendritic region transforms to a grain boundary ferrite and side-plate ferrite-rich microstructure, which corresponds to the thin columnar grain zone. Briefly, the sequence of morphological change could be simplified as a block diagram which is shown as Fig. 65.

In fact, in the early 1950's, Paton already noticed this phenomenon [10]. He simply mentioned that "coarse columnar crystallites comprised a group of dendrites which were devoid of branches and fine columnar crystallites were also dendrites with well developed branches". But, he did not explain the mechanism of this phenomenon. And for two decades, little study has been extended to this issue.

Using this model, most morphological features of low carbon

steel welds could be reasonably explained. A low form factor weld has a deep weld pool which gives rise to less dendrite renucleation events. Thus, it contains a wide cellular dendritic region which mainly transforms into coarse columnar austenite grains, and results in a great percentage of the acicular ferrite-rich coarse columnar grain zone in the weld metal. A high form factor weld has a shallow weld pool which gives rise to more dendrite renucleation events. Thus, it contains a wide columnar dendritic region which transforms to fine columnar austenite grains, and ends up with a large thin columnar grain zone almost full of grain boundary ferrite and side-plate ferrite.

Based on this model, it could also be pointed out that the coarse grain size near the fusion lines in the weld metal of mild steels might not result from the coarsened grain size of HAZ. The traditional view often attributed it to the epitaxial growth from the coarse grains of HAZ. But the solidification structure indicated the opposite, as shown in Fig. 66. Though, in steel ES welds, the starting cells indeed grew epitaxially from the fusion boundaries, no correlation was observed between the fine cellular dendrite arm spacing and coarse grain size of HAZ. The coarse columnar grains should be the products of lateral austenitic growth in the low-impurity cellular dendrite region near the fusion boundaries. In term of austenite growth, situations in the two sides of fusion boundaries were rather different in aspects of their impurity segregation and inclusion distribution. It was also evident from Fig. 66 that the ease of lateral austenitic growth in the cellular dendritic region often made the spacing of coarse columnar grains in the weld metal side double or triple the

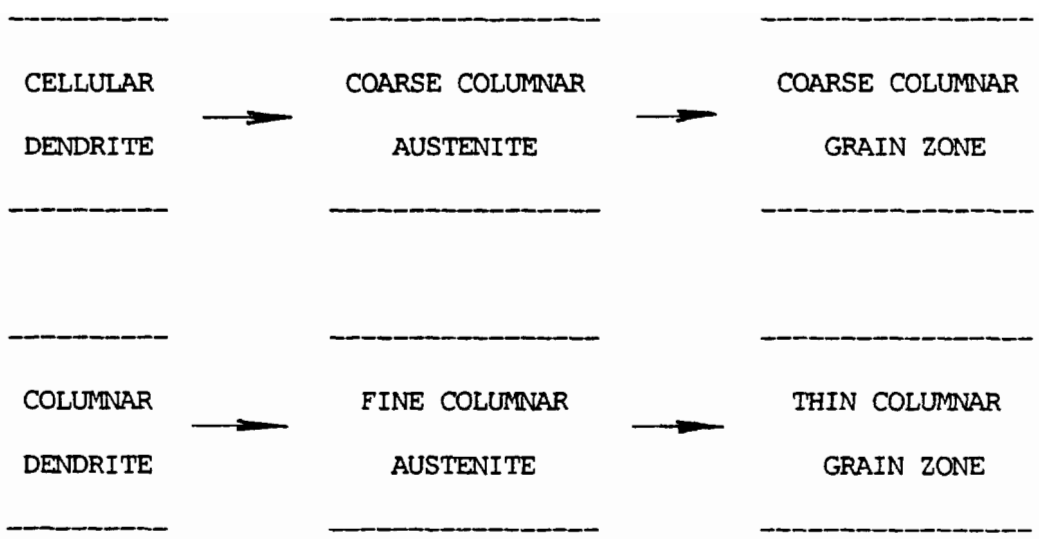

Fig. 65 Sequence of Morphological Change in low carbon steel welds.

coarse grain size in the HAZ side.

All the considerations above are mainly aimed at the weld metal of low carbon steels. But the basic understanding could also be applied to other kinds of steels. Of course, if additional alloying elements are introduced into the weld pool, the situation would become more complicated. Detailed discussions will be given in the following sections.

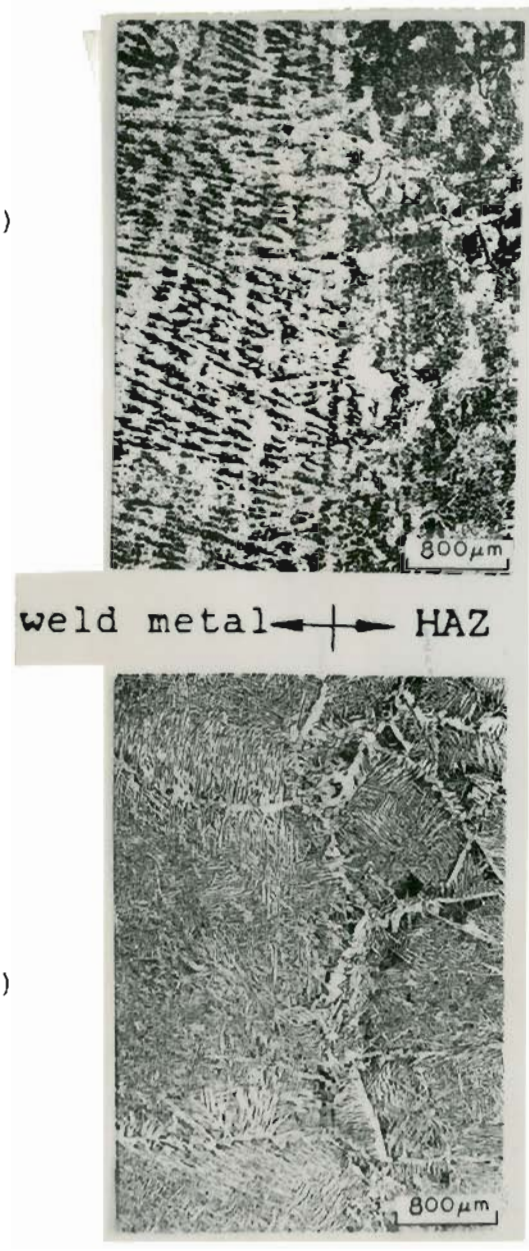

Fig. 66 Solidification structure (a) and solid state microstructure (b) near fusion boundary in A36/ 50mm thick ES welds (Weld #2A-2)

B. INFLUENCE OF ALLOYING ELEMENTS

1. FORMATION OF EQUIAXED DENDRITES

As described above, alloying additions substantially promoted an equiaxed dendritic growth near the weld center. To explain this phenomenon, it is better to recall Fig. 4 again. The increase of solute content in the weld metal could greatly influence the transition of solidification mode from columnar dendritic to equiaxed dendritic growth. That was analogous to a decrease in the solidification parameter, G/R. The central equiaxed dendrite zone induced by alloy additions showed superior resistance to hot cracking when the welding speed was increased since the simultaneously nucleated equiaxed dendrites are believed to disperse remaining impurities to a comparatively large area rather than a narrow centerline, thereby reducing detrimental segregations.

In addition, it is necessary to consider the type of primary solidified products in alloyed weld metals. Fig. 67 displays the left corners of Fe-C, Fe-Cr, Fe-Ni and Fe-Mo phase diagrams. Though the real alloyed weld metals were multi-element systems, those binary diagrams still gave helpful information. Due to the rightward displacement of maximum delta-Fe composition in the Fe-Cr, Fe-Ni or Fe-Mo phase diagrams compared with the Fe-C diagram, the primary dendrites in those alloyed mild steel weld metals are always delta-ferrite.

As known, delta-ferrite usually has a higher impurity solubility and less interfacial segregation than gamma-austenite during primary solidification. Thus, Cr, Mo and Ni additions can reduce the suceptibility of both centerline and radial hot cracking, and provide a relatively beneficial (crack resistant) solidification structure.

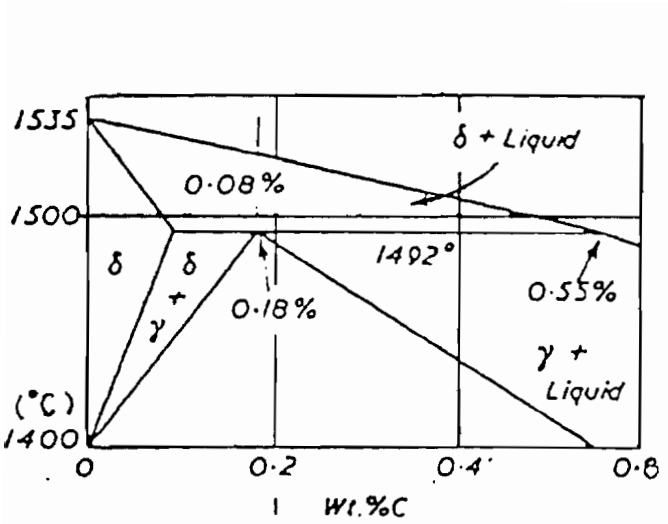

a)

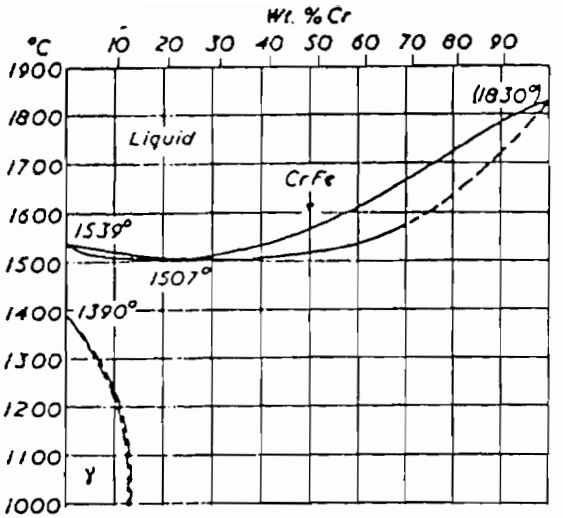

b)

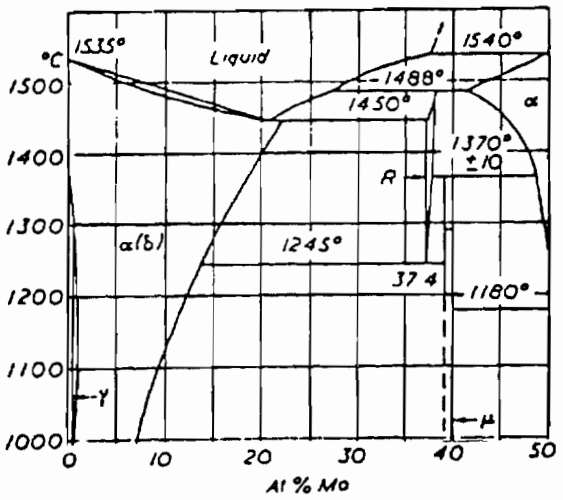

c)

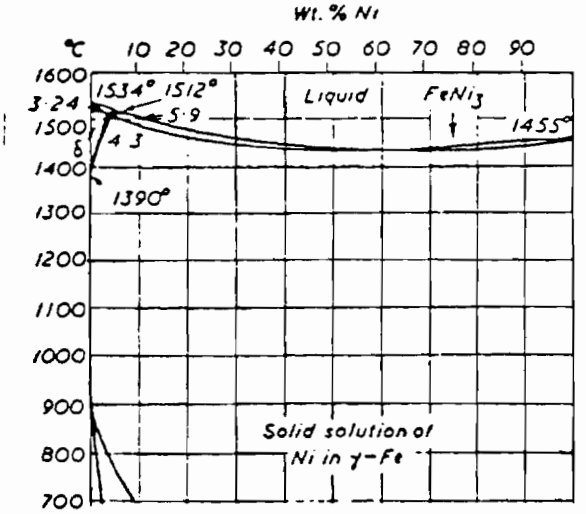

d)

Fig. 67 Left corners of a) Fe-C, b) Fe-Cr, c) Fe-Ni, and d) Fe-Mo phase diagrams.

2. FORMATION OF GRAIN-BOUNDARY AND SIDE-PLATE FERRITES

Most alloying elements affect austenite decomposition. In general, carbide-forming elements not only severely suppress high temperature austenite decomposition products, but also cause significant strengthening effects and make transformation products more complicated, because some new carbide phases may form. Austenite-stablizing elements usually depress the transformation temperature from austenite to ferrite and place obstacles to the nucleation and growth of high temperature products.

In determining the reason why Cr-Mo and Ni-Mo additions caused such sharply different morphologies during the ferritic transformation, it is important that the influence of each alloying element on the ferritic transformation products be discussed. First of all, based on the fundamental knowledge of physical metallurgy [81, 82], the following facts should be borne in mind:

1) Cr, Mo, Mn and Ni, being dissolved in austenite-Fe, raise the diffusion activation energy of carbon, and lower the carbon diffusion coefficient in austenite-Fe.

2) Cr and Mo, being ferrite-stablizers, basically shift the proeutectoid line (the A_{c3} line) in the Fe-C phase diagram upwards to the left, while Ni and Mn, being austenite-stablizers, shift it downwards to the left. Fig.68 is a schematic expression of those trends.

3) Adding Cr or Mo to the mild steel causes its austenite decomposition curve (the TTT or CCT curve) to separate into two C-curves, and shifts the upper one upward to the right. Adding Ni and Mn cause the whole

curve moving downward to the right, as shown in Fig. 69.

All those factors will be seen to directly interfere with the kinetics of both ferritic nucleation and growth.

Austenite decomposition in the steel weld metal is basically a diffusion-controlling transformation. The volume fraction of ferrite during transformation, f, can be expressed as

$$f = 1 - \exp\,[-\,x/3\,\dot{N}\,V^3\,t^4] \qquad ---(9)$$

where $\dot{N}$ is the nucleation rate, V is the growth rate, and t is time [96]. N is known to be directly proportional to the transformation driving force, ΔG. Considering the change in carbon concentration of austenite around ferrite nuclei (Fig.70), the driving force for ferrite nucleation can be written as:

$$\Delta G = RT\,\{Co\,\ln(C_\gamma/Co) + (1-Co)\,\ln[(1-C_\gamma)/(1-Co)]\,\} \qquad ---(10)$$

where C_γ is the enriched carbon concentration in the austenite around the ferrite nuclei, and C_o is the nominal carbon content of the base metal. Due to the low nominal carbon content in all the weld metals,

$$Co << 1 \text{ (i.e. } Co \dashrightarrow 0\text{).}$$

Then, $(1-Co) \dashrightarrow 1$, $(1+Co) \dashrightarrow 1$,

since, $(X)^{Co} \dashrightarrow (X)^0 = 1$,

the above equation reduces to:

$$\Delta G = RT\,[Co\,\ln(C_\gamma/Co) + \ln(1-C_\gamma)]$$

$$= RT\,\ln\{\,[(C_\gamma)^{Co}\,(1-C_\gamma)]\,/\,(Co)^{Co}\,\}$$

$$= RT\,\ln\{\,[(C_\gamma)^{Co} - (C_\gamma)^{(Co+1)}]\,/\,(Co)^{Co}\,\}$$

thus, $\Delta G = [RT\,\ln(1-C_\gamma)] \qquad ---(11)$

This means that, in the case of mild steel welds, the driving force

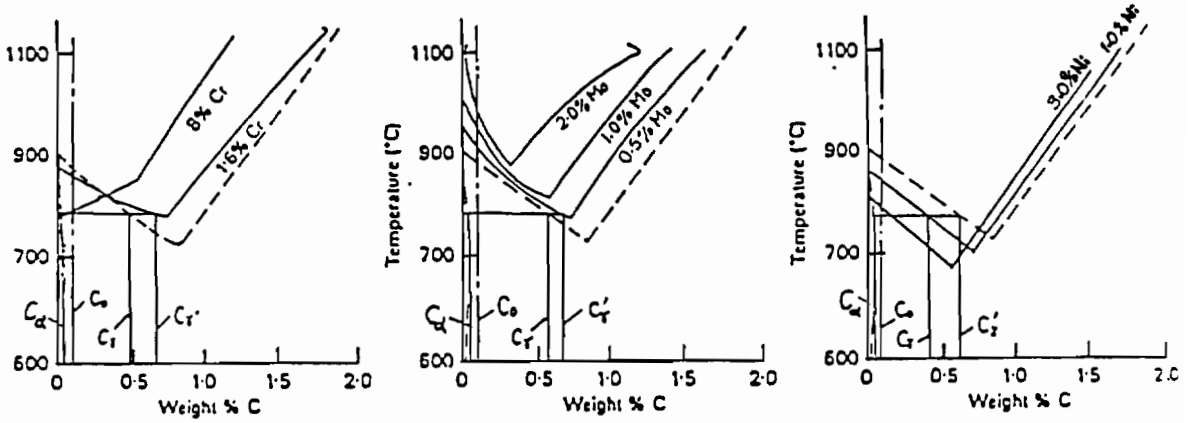

Fig. 68 Effects of alloy elements on austenite decomposition of low carbon steels.

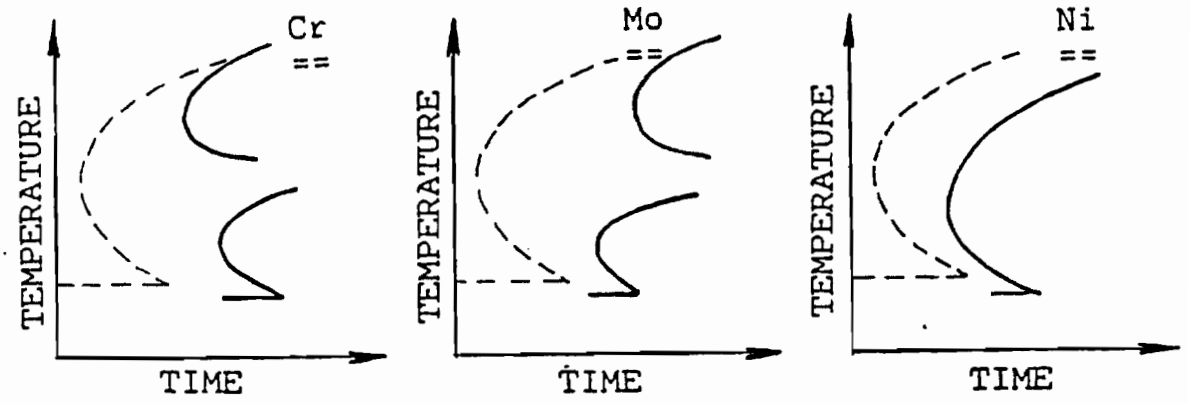

Fig. 69 Effects of alloy elements on the C-curve of low carbon steel.

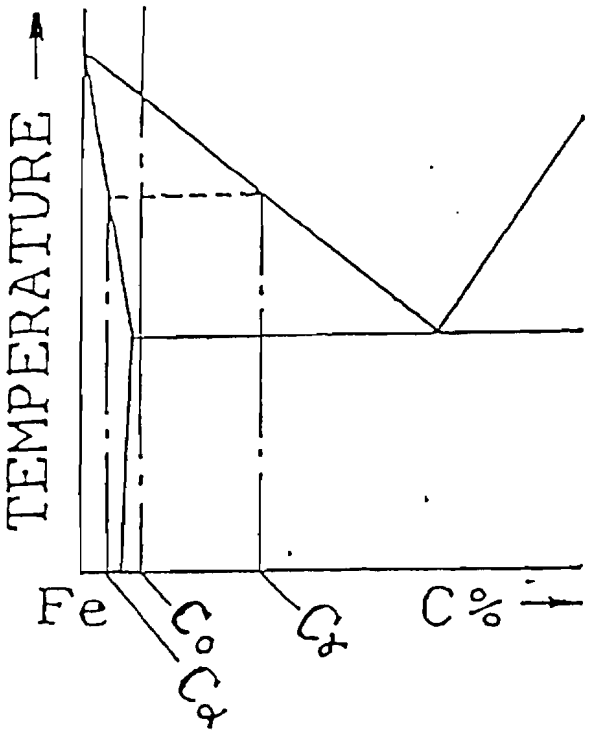

Fig.70 Variation of carbon concentration during austenite decomposition.

for ferrite nucleation is mainly governed by the enriched carbon concentration around the ferrite nuclei, C_γ. According to their effects on the A_{c3} line and eutectoid temperature in mild steels (Fig. 68), low Cr (with a small undercooling), Ni and Mn additions in the mild steel weld metal lower C_γ, thus decreasing the ferritic nucleation rate, while Mo raises C_γ, increasing this rate. But, it should be noted that, in fact, the site saturation of energetically favorable austenite corners and boundaries occurs before about 20% transformation [81], so, with a small undercooling, the actual nucleation rate is not as important as the growth rate of ferrite.

The growth rate of grain-boundary ferrite (V_{gb}) forming at a small undercooling, according to the change of carbon concentration across the growing interface (Fig. 71-a), can be expressed as:

$$V_{gb} = [D_C^\gamma (C_\gamma - Co)] / [L (C_\gamma - C_\alpha)] \quad ---(12)$$

where D_C is the carbon diffusion coefficient in austenite, L is the carbon-enriched length ahead of the growth interface, and C_α is the carbon content of ferrite. The carbon-enriched length, L, is controlled by the diffusion of carbon and could be considered as the square root of D_C t, where t is time, then

$$V_{gb} = [(D_C^\gamma)^{1/2} t^{-1/2} (C_\gamma - C_o)]/(C_\gamma - C_\alpha) \quad ---(13)$$

By similar reasoning, the growth rate of side-plate ferrite (V_{sp}) forming at an intermediate undercooling is:

$$V_{sp} = [D_C^\gamma (C_\gamma - C_o)] / [A\ r\ (C_\gamma - C_\alpha)] \quad ---(14)$$

where A is a constant and r is the tip radius of the side plate. An approximation in the case of low carbon weld metal is

$C_o \longrightarrow C_\alpha$, thus, $(C_\gamma - C_o) \longrightarrow (C_\gamma - C_\alpha)$.

so $V_{gb} \longrightarrow [(D_C^{\gamma})^{1/2} t^{-1/2}]$, ---(15)

and $V_{sp} \longrightarrow [D_C^{\gamma} / A r]$. ---(16)

It follows that the growth rate of both grain-boundary ferrite and side-plate ferrite in low carbon steel welds were principally governed by the diffusion coefficient of carbon in the austenite matrix.

Cr, Ni, Mn and Mo, being dissolved in austenite-Fe, raised the diffusion activation energy of carbon and reduced the diffusion coefficient of carbon in austenite [81], thereby effectively depressing the growth of both grain-boundary ferrite and side-plate ferrite.

Another important feature of Ni and Mn is their partitions during austenite decomposition [81]. In Fe-C-X alloys, there are two basically different proeutectoid ferrite growth modes in undercooled austenite: 1) growth with partition of the alloying element X between austenite and ferrite under local equiliblium conditions, and 2) growth without partition of X between austenite and ferrite. In the first ferrite grows at a slow rate controlled by the diffusivity of X in austenite. In the second mode, the ferrite growth rate is relatively high because it is controlled by the diffusivity of carbon which is several orders higher than that of metallic elements. As reported [81], the strong austenite-stablizers Ni, Mn and Pt are the only elements to show partition to the austenite phase. therefore, Ni and Mn could be especially effective in suppressing high temperature austenite decomposition products.

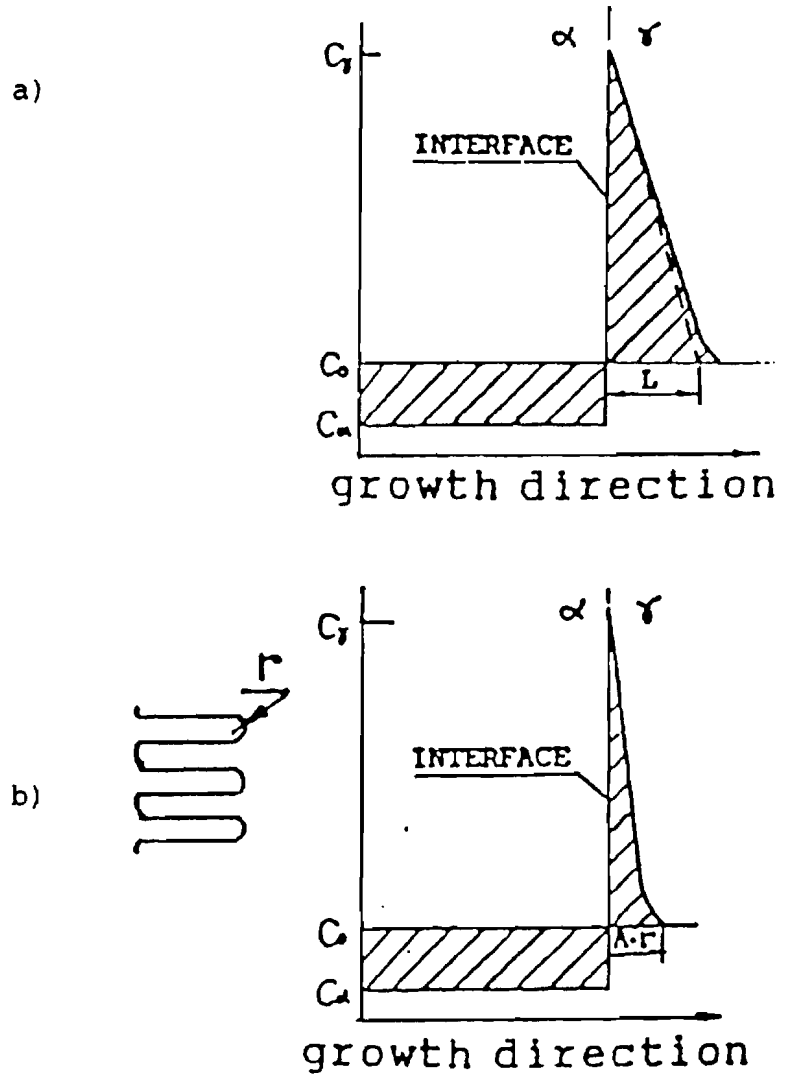

Fig. 71 Local carbon concentration around the growth frontier between austenite and ferrite for the formation of a) grain boundary ferrite, and b) side-plate ferrite.

3. FORMATION OF ACICULAR FERRITE AND BAINITIC FERRITE

Acicular ferrite is an intermediate temperature product of low carbon austenite decomposition. In order to form it, those high temperature products (blocky, grain boundary and side-plate ferrite) must be suppressed, while not excessively impeding the austenite decomposition, otherwise low temperature transformation products (bainitic ferrite and martensite) will be produced. Generally, in the absence of those additional alloying elements, grain boundaries are more favorable sites for ferritic nucleation than inclusions. In mild steel electroslag welds, the formation of grain-boundary ferrite rapidly raises the carbon content within the thin columnar austenite grains, thereby reducing the supersaturation and making intragranular nucleation even more difficult. As a result, less acicular ferrite forms in the thin columnar grain region. Only in the untransformed interior of coarse columnar austenite grains, where the enrichment of carbon plays a less significant role, and where inclusion sites become energetically favorable with more undercooling, can acicular ferrite form.

Since Cr and Mo, both ferrite stablizers, displace the upper part of the austenite decomposition curve (C-curve) upward to the right and raise the ferritic transformation temperature, the following process is proposed. Above a certain Cr-Mo content, the formation of acicular ferrite is less energetically favorable and there is a decreasing or even no chance for intersection between the cooling curve associated with ESW and the upper C-curve. Thus, the austenite matrix could bypass the upper C-curve and transform to a fully bainitic microstructure.

On the contrary, the presence of Ni and Mn, both the austenite stablizers, shift the whole c-curve downward to the right and cause the ferritic transformation temperature to decrease. Therefore, for relatively wide ranges of Ni and Mn contents and transformation temperature, the cooling curve associated with ESW continuously intersects the ferritic transformation curve, resulting in a fine acicular ferrite-predominating microstructure throughout the weld metal. No doubt, excessive Ni will further delay the ferritic transformation and eventually produce bainite or martensite. In this investigation, the beneficial role of Ni in promoting acicular ferrite was extended to at least 1.5%Ni (plus 0.3%Mo and 1.2%Mn).

Of course, the comprehensive function of multi-alloy elements is often not a simple linear summation. In this investigation, the concurrent addition of Mo plus Cr exerted too much of a negative effect on the ferritic transformation, whereas a small amount of Mo could help Ni and Mn to promote the formation of acicular ferrite.

4. CONTRIBUTION OF Ni ADDITION

As discussed above, both Ni and Mn can be utilized in alloying low carbon steel weld metals. But, chemical analyses revealed that all conventional mild steel weld metals in this investigation already contained 1.0 to 1.2% Mn. It implied that the Mn level was not sufficient to produce a substantial change in austenite decomposition due to the very slow cooling rate in ES weld metals. Although cost attractive, further increasing the Mn content is not beneficial because of excessive hardenability, the Mn/Si ratio and deoxidation. In comparison with

Mn, Ni is more favorable for the following reasons:

(1) Ni shows a rather mild strengthening effect (solution hardening only) when alloyed into the mild steel matrix. In fact, its strengthening effect is 60% less relative to that of Mn [81]. Thus, the Ni alloyed weld metal will not display excessively higher hardness and strength levels than the base metals.

(2) Ni can be dissolved into both austenite-Fe and ferrite-Fe, and its solubility in iron extends up to 18% [81]. Thus,in this investigation, there is no risk of forming comlex precipitates or metallic compounds.

(3) Ni has a low diffusivity in austenite. Table 7 gives some data of the diffusion coefficient in gama-Fe for C, Cr, Ni and Mn. Also, as reported [81], Ni shows its partition at the higher austenite decomposition temperatures. Both features make Ni extraordinarily effective in suppressing the growth of high temperature ferrite transformation products.

(4) Ni is of a low affinity for oxygen. Its addition in the mild steel weld metal does not form extra oxides as the Mn addition.

Therefore, in order to improve the weld metal microstructure, it was more appropriate to keep the existing Mn level (supplied by both base metal and filler metal) and introduce Ni as a leading role to promote the formation of acicular ferrite.

In addition, of equivalent interest is the contribution of Ni to the low temperature toughness of mild steel weld metals. During this investigation, it was found very interesting that the Ni-Mo alloyed acicular ferrite-rich microstructure showed much higher toughness than the Cr-Mo alloyed one. (Of course, the strength of the latter was

higher.) Fig. 72 displays two kinds of acicular ferrite-predominant weld metals deposited on A36 plates, which contain 0.51% Cr-0.20% Mo and 1.13% Ni-0.20% Mo respectively. At 0° F, the CVN toughness of Cr-Mo alloyed specimens was surprisingly low, 12 ft-lb, whereas that of Ni-Mo alloyed one was high at 40 ft-lb. Although the number density of acicular ferrite plates in the former was somewhat lower than in the latter, it did not explain such great a disparity in toughness adequately. Thus, before a correct answer is developed, it seems worth to discuss the contribution of Ni to the low temperature toughness of ferrite-Fe brifly.

As known, the ductile-brittle fracture transition of a material is influenced by a comparison between its yeild stress and its micro-crack growth stress (cleavage fracture strength). When a material's yield stress is greater than its cleavage fracture strength, it shows a brittle cleavage failure, and when smaller, it shows a ductile failure.

The yield stress 0y can be expressed as the Hall-Petch relation:

$$\sigma_y = \sigma_i + k_y d^{-\frac{1}{2}} \quad \text{---(17)},$$

where σ_i is the lattice friction stress, k_y is a parameter, and d is the grain diameter or subgrain size. Thus, At the same d, the variations of σi and k_y exert very important effects on yield stress, in turn, the ductile-brittle transition and toughness. σi stands for the resistance to the motion of unlocked dislocations arising from the Peierls-Nabarro lattice stress. And, k_y basically depends on two factors: the locking of dislocations and the number of available slip system [97].

TABLE 7

DIFFUSION COEFFICIENT OF ALLOYS IN GAMMA-Fe

Solvent	solute	diffusion coefficient [cm^2/s^{-1}]		
		910°C	1050°C	1300°C
gamma-Fe	C	1.7×10^{-7}	6.5×10^{-7}	4.8×10^{-6}
	Ni	7.3×10^{-13}	4.5×10^{-12}	2.5×10^{-10}
	Mn	9.0×10^{-13}	7.7×10^{-12}	4.0×10^{-10}
	Cr	3.0×10^{-12}	5.8×10^{-11}	7.8×10^{-9}

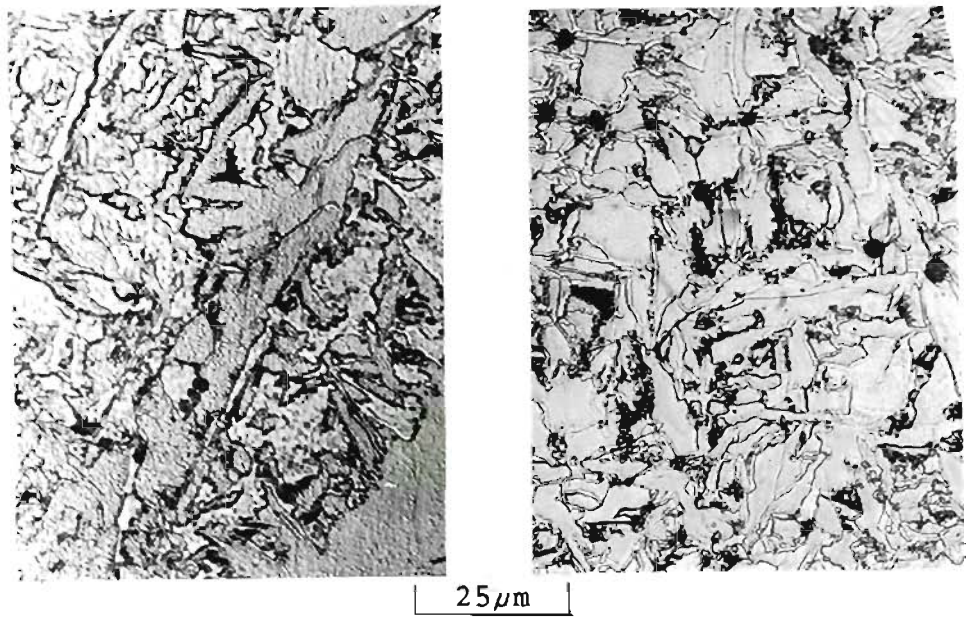

a) b)

Fig.72 Acicular ferrite-predominant A36 ES weld metals containing a) 0.51% Cr-0.20% Mo (Weld #33A), and b) 1.13% Ni-0.20% Mo (Weld #53).

Regarding the relation between the slip phenomenon and the crystal structures, three well-established laws governing the slip behavior exist [97], namely: i) the direction of slip is almost always that along which the atoms are most closely packed, ii) slip usually occurs on the most closely packed plane, and iii) from a given set of slip planes and directions, the crystal operates on the system (plane and direction) for which the resolved shear stress is the largest. A bcc lattice has only a single well-defined close packed <111> direction, but no a well-defined close packed plane. A few planes, {112}, {110} and {123}, are of equally high density of packing in the bcc lattice. The choice of those slip planes depends on temperature. Iron often slips on all the slip planes at once in a common <111> slip direction at and above the room temperature. With the decrease of temperature, slip on (112) and (123) planes begins to fade out.

The number of "active" slip systems operating at low temperatures has profound influence on not only k_y, σ_i, but also the cleavage strength. If more slip systems still remain active over a broadened low temperature range, the value of k_y will not increase rapidly, and the ease of cross slip mechanism decreases the temperature dependence of the friction stress of iron lattice [98]. Therefore, σ_y will decrease. Meanwhile, if more "active" slip systems exist at low temperature, a great amount of plastic relaxation can be produced by the operation of these slip sources at a cleavage crack tip. The effective surface energy to cause the propagation of cleavage cracks then increases, resulting in the increase of cleavage fracture strength. Thus, those factors are certainly of immense importance in controlling the ductile-

brittle transition of materials.

The Engel-Brewer theory [99] states that the structure of a material is determined by its s and p electrons, and its coherent energy by the number of s, p, and d electrons. The bcc structure is characterized by 1 s, p electron (a range of 1 to 1.5), the hcp structure by 2 s, p electrons (a range from 1.7 to 2.2), and the fcc structure by 3 s, p electrons. Thus, the electron configuration of alpha-Fe is d^7s; of Ni, d^7sp^2; of Cr, d^5s; of Si, sp^3 and of Mn, d^4sp^2 and d^6s (two coexisting configurations) [99].

Materials with covalent bonds have unfilled d-electron levels and share their electrons each other. All covalent materials behave strongly anisotropic and show slip only at high temperatures. With the decrease of temperature, they became very brittle. Alpha-Fe atoms have a unfilled 3d-electron level, thus, there is, more or less, a certain characteristic of covalent bonding. It results in a different temperature dependence of the critical resolve shear stress (CRSS) for the operation of slip systems in different planes. Especially at low temperatures, some of its slip systems are fading out, hence, the increase of yield stress (the expression of both σ_i and k_y) results which is by far greater than it would be expected from the temperature dependence of CRSS alone.

The atoms of substitutional alloys cause a disturbance in the iron matrix by changing the lattice parameter, the elastic modulus and the electron configuration. At higher temperatures, the structural disorder is superposed to that of thermal vibration. But, at low temperatures, the structural disturbance will be of greater importance

than thermal vibrations. The substitution of Cr or Mn (in some cases) atoms in the iron lattice has a slight deficiency of electrons and would not be expected to get rid of the influence of covalent bonding on alpha-Fe. The substitution of Si atoms in the iron lattice would be expected to be highly detrimental, as Si has no d electrons at all. However, compared with alpha-Fe, Ni has excessive electrons and should diminish the influence of covalent bonding. Meanwhile, as explained by W. C. Leslie and his colleagues [100], cohesive energy increases smoothly with the number of s, p, and d electrons, and toughness increases with increasing cohesive energy. Thus, Ni, with its striking electron configuration, should increase toughness markedly.

Up to this point, it could be thought that Ni, compared to other alloying elements, might keep more slip systems "active" at low temperatures, which helped to release the stress concentrations at the tip of micro-cracks, thereby delaying cleavage failure to much lower temperatures. As a matter of fact, this special contribution of Ni to low temperature toughness of alpha-Fe was already reported a long time ago [101]. Impressive evidence related to this effect of Ni is shown in Figure 73. As can be seen from this plot, for a Fe-3.28% Ni alloy, the slope of Hall-Petch relation, k_y, at 77°K was very close to that at room temperature, while for common alpha-irons, it was definite that k_y increases sharply at low temperature.

This is probably the reason why the acicular ferrite-rich weld metal alloyed by Ni-Mo additions showed higher CVN impact toughness than that alloyed by Cr-Mo additions.

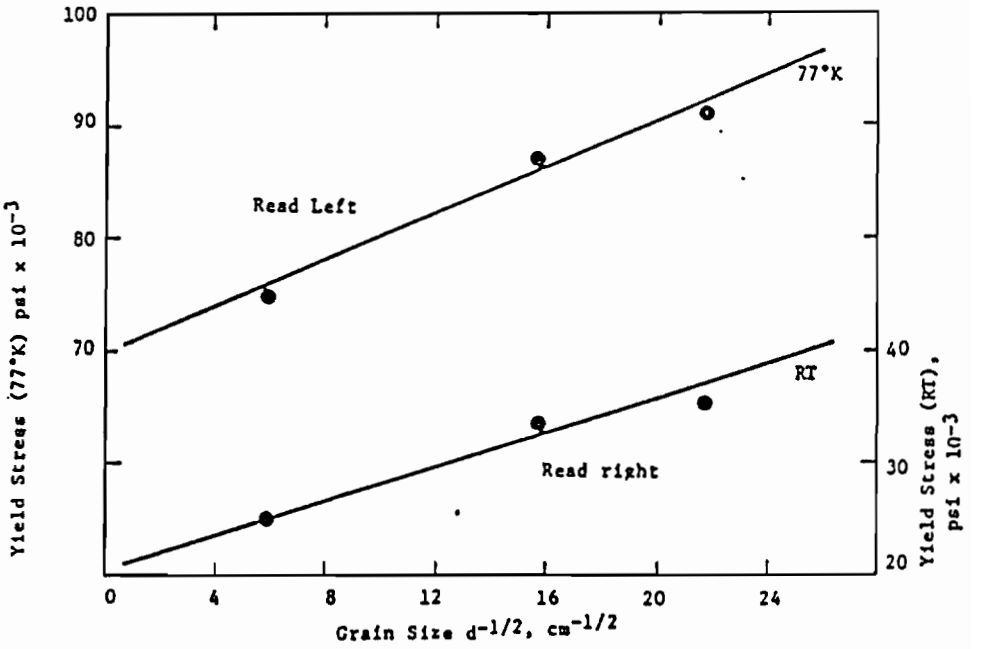

Fig. 73 Hall-Petch plots for Fe-3.28pct Ni alloy at room temperature and 77°K [101]

5. ALLOYING DESIGN OF Ni-Mo-Mn STEEL FILLER METAL

No doubt, Ni should have a leading role to upgrade the microstructure and toughness of mild steel ES weld metals. But, from a practical viewpoint, the alloying addition with a single element is always less powerful than with multi-elements. Mn is an important alloying element in both A36 and A588 steels. A Mn content similar to that of base metals has to be maintained in the filler metal. Mo was reported to promote acicular ferrite in weld metals deposited by other welding techniques [56]. If the weld metal carbon content can be controlled at a low level, the potential for carbide formation will be reduced. A small amount of Mo should effectively reduce the diffusibility of carbon and assist in suppressing high temperature austenite decomposition products.

Thus, a Ni-Mn-Mo alloying methodology was established for A36 and A588 electroslag weld metals. Commercially available AIRCO AX-90 solid wire contains a Ni-Mn-Mo composition (Table 1) and was first used to examine the alloying effect on weld metal toughness. This alloying approach proved reliable and successful. Later, a tubular filler metal was developed as a modified formulation and denoted TW8544. The composition of commercial AX-90 wire did not fully conform to the requirement of this ESW study. The major chemical differences between TW8544 and AX-90 include: 1) reduced carbon content (0.3% vs. 0.8%), 2) increased Ni content (2.3% vs. 2.1%), 3) slightly increased Al as a killing agent and 4) slightly increased Ti.

Throughout the whole investigation, TW8544 alloying filler wire was excellent for both A36 and A588 electroslag weld metals because

the resulting strength level was only slightly higher than that of the base metals, while toughness was improved reaching or surpassing the level of base alloys. It appears that, in general, the Ni-Mn-Mo alloying principle could spread to the ESW of other low carbon steels as well as other high heat input welding processes.

6. CHARACTERISTIC PARAMETER FOR ACICULAR FERRITE STUDY

Conventionally, the width of acicular ferrite plates was initially used as its characteristic parameter. A smaller width of acicular ferrite represents a smaller mean free path for the propagation of cleavage cracks, thereby resulting in better toughness. As mentioned already, acicular ferrite nucleates around inclusions in the weld metal and grows until impinging with each other. Due to an uneven distribution of weld inclusion sizes and spacings, the acicular ferrite width varied greatly. Meanwhile, the specimen observation plane cut most acicular ferrite plates in arbitrary positions. An arbitrary cutting section hardly represented the real width of acicular ferrite plates, due to its elongated spindle-like configuration. As a matter of fact, in most cases, experimental data often suffered scattering and compounded the difficulty of accurate measurement.

In view of this fact, another characteristic parameter, the number density of acicular ferrite plates (i.e. the number of acicular ferrite plates in per unit area), was used for the acicular ferrite study. As a statistical value, it was a more reliable, practical and characteristic term. It can also be correlated to its formation temperature, its cleavage resistance, as well as the distribution of

inclusions. Fig. 74 shows that the number density of acicular ferrite plates is almost linearly proportional to the CVN impact toughness. Figure 75 indicates that this number density increased with increasing the weld metal Ni-Mo content. This correlation was consistent with the fact that the increase of Ni-Mo content lowered the austenite decomposition temperature so that more fine inclusions became energetically favorable to nucleate acicular ferrite. Therefore, it is clear, by inspections of those figure that this new characteristic parameter stands above the former one in regard to the reliability and integrality.

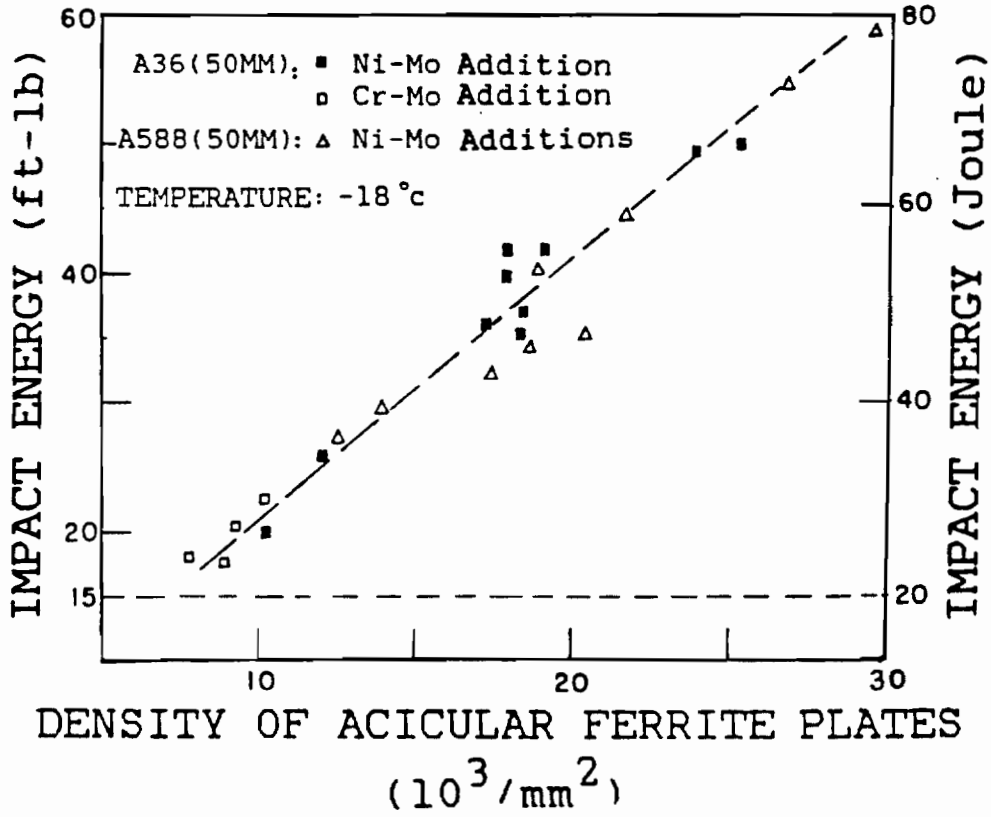

Fig. 74 Correlation between the number density of acicular ferrite plates and CVN toughness

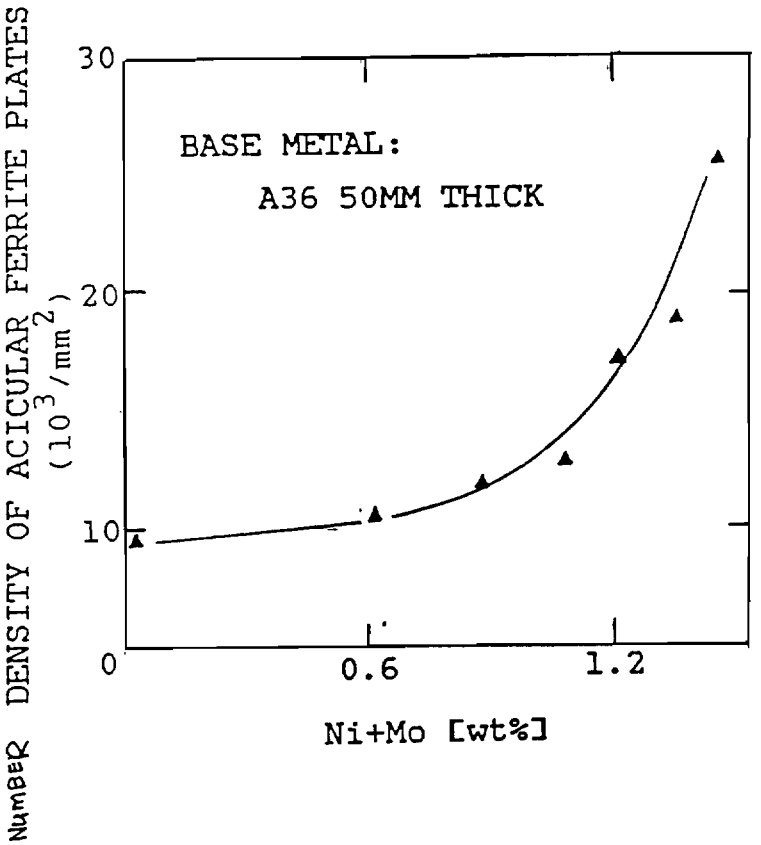

Fig. 75 Correlation between alloy content and the number density of acicular ferrite plates.

C. TUBULAR FILLER METALS

1. ADVANTAGES OF METAL-POWDER CORED FILLER METALS

The advantages of metal powder-cored tubular wire were attributed to several unique characteristics during ESW. First, the tubular wire contained metal powder which showed higher electrical resistance than the solid wire. At a given voltage and current setting, the main electrical resistance heating in the slag pool (represented by the distance between the electrode tip and the molten metal) was reduced resulting in reduced ohmic heating. Thus, the depth of weld pool decreased, the weld penetration decreased and the form factor increased. Secondly, since powder metal required less energy to melt, it became more difficult to obtain long extensions into the molten slag than with the solid electrodes. In order to maintain an ohmic relationship for the power supply, an increased filler metal feed rate was needed to attain the specific current, thus accounting for the observed increased deposition rate and decreased heat input. It should be emphasized that the superiority of tubular wire can be maximized by increasing the welding current and decreasing the operation voltage. Only at a high current and a low voltage, is the value of form factor getting more critical because of the susceptibility to the hot cracking. Then, the tubular wire welding becomes a better choice.

2. WELD METAL OXYGEN CONTENT

One early concern regarding the use of tubular wire was whether the hollow electrode would result in excessive oxidation products in the weld pool. The powder metal inside hollow electrodes was not as closely packed as the solid metal. More iron oxides could be contained inside tubular wires, which might affect the reaction in the weld pool. As reported [52], an optimum oxygen level existed in the low carbon steel weld metal for the acicular ferrite formation. Acicular ferrite could not be expected if the weld metal oxygen content was below 200ppm or above 400 ppm. Oxygen content in the weld metal governed the amount and distribution of inclusions. In a weld metal with an oxygen level below 200 ppm, there were insufficient inclusions which provided nucleation sites for acicular ferrite. While above 400 ppm, more inclusions were able to induce the early formation of grain-boundary ferrite before the temperature of weld metals cooled down to the range of acicular ferrite formation.

Chemical analyses of weld metals, as sketched in Fig. 76, proved that the concerns were uncalled-for, since the resulting 200 to 300 ppm in TW8544-deposited weld metals was the optimum oxygen level to promote the formation of acicular ferrite in weld metals.

Judging from this, the combination of Ni-Mn-Mo alloying and tubular wire (TW8544) can be expected to consistently improve the performance of mild steel electroslag weld metals.

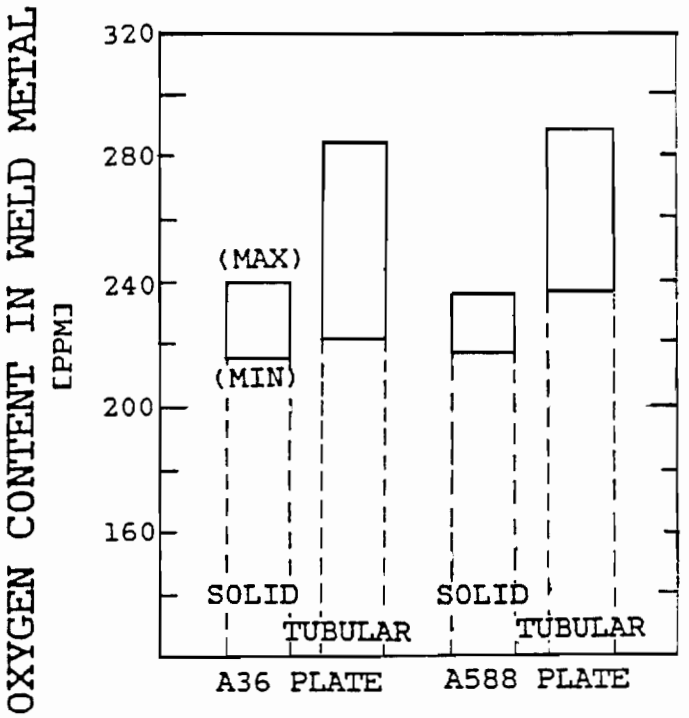

Fig. 76 The oxygen levels in A36 and A588 electroslag weld metals

D. ELECTROSLAG THERMAL TRANSFER PATTERN

1. SPECIAL HEAT GENERATION AND TRANSFER IN ELECTROSLAG WELDMENTS

It is generally accepted that reducing the welding heat input is the primary means of reducing the size of the HAZ. However, the HAZ size data in this investigation, shown in Figures 43 and 44 did not follow this trend. When the weld heat input was changed, the HAZ size of electroslag welds varied in a rather irregular manner. Even at the same heat input level, the data of HAZ size also showed great scattering. To explain this phenomenon, the thermal transfer pattern of ES welds must be taken into account.

Unlike most fusion welding processes, there is no arc heating in electroslag welding except at the starting of the weld before the flux melts by the heat of the arc. After a stable electroslag mode is set, heat is generated from the resistance heating of slag pool by electric current passing through the bath of molten slag. The ohmic heat generated melts the filler metal, guide plate and the faying surfaces of base metal to be joined. Meantime, it is also transferred throughout the welding area by convection, conduction, and radiation. Among the total heat generated, the heat transferred towards the base metal from the side-wall of weld pool, being reported close to 60% of the total heat generated [10], inevitably results in large HAZs.

The thermal transfer associated with the HAZ can be separated into two parts, as shown in Figure 77(a): (1) preheating conducted on the unmelted base metal by the molten slag bath, and (2) the heat transfer from the molten pool through the solidified deposits towards

the base metal. Variation in the weld pool geometry alters the magnitude of both parts. As the weld pool moves up, some of the base metal associated with part 1, which has already been heated up, will melt. This implies that the thermal effect related to part 1 is partially offset due to this melting. As weld penetration varies, the degree of offsetting changes. In most other welding processes, situations are different, since (1) no substantial slag preheating (part 1) exists, and (2) no offsetting happens during the motion of weld pool.

Thus, for ES weldments, the total heat built up in the HAZ is not a simple summation of these two parts of thermal transfer. It also extensively depends upon the geometry of the weld pool.

2. EFFECTS OF WELD POOL GEOMETRY ON THE HEAT-AFFECTED SIZE

To express the variation of weld pool, it is beneficial to simplify the pool shape into a rectangle and a half ellipse, as shown in Figure 77 (b), where G is the joint gap, W is the weld pool width, h is the preheating height, and D is the weld pool depth. Ignoring the small thickness difference at the location of reinforcement, the volume of molten pool, V, could be expressed as:

$$V = [h\ G + (\pi\ W\ D\ /\ 4)]\ T \qquad ---(18)$$

where T is the thickness. Table 13 indicates the variation of these factors and their effect on the HAZ size.

Usually, the reduction of heat input is achieved through narrowing the joint gap, raising the welding speed, or lowering the base metal dilution. But, in ESW, all those could give rise some adverse effects. For example, with the decrease of form factor, the

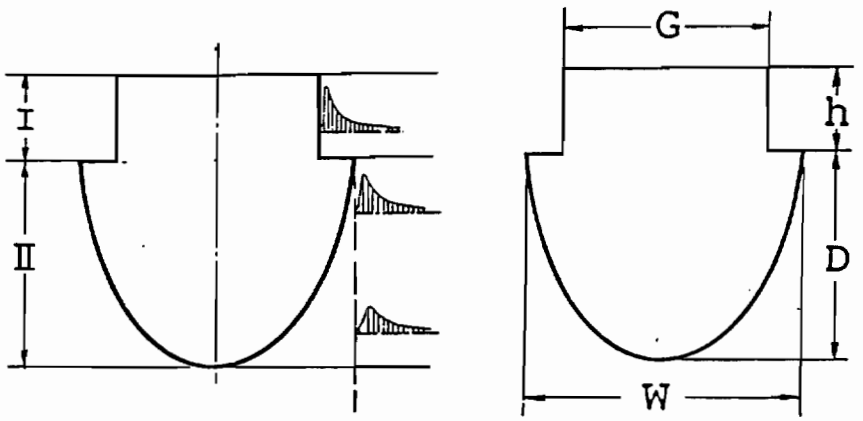

a) b)

Fig.77 The analysis of thermal transfer in the molten pool of ES welds

a) two parts of weld delivering heat into the HAZ,

b) simplified molten pool and its dimension.

TABLE 8

VARIATION OF WELD CHARACTERISTICS

characteristic	variation	effect	HAZ size
heat input	up	more heat	up
form factor(W/D)	down	greater part-2	up
dilution (W/G)	down	less offsetting	up
h	up	greater part-1	up
W	down	less offsetting	up
D	up	greater part-2	up
G	up	less offsetting	up

* The definitions of h, W, D and G can be found in Figure 77.

weld pool deepens so that the thermal effect related to part 2 increases, thereby resulting in increasing HAZ size. Similarly, the decrease of dilution reduces the offsetting, which causes more heat built up.

It is now clear that, in ESW, besides heat input, the geometry of molten pool also influences the final accumulated heat in the HAZ and its size, too.

Until the present study, no reference paid enough attention to this unique feature of thermal transfer feature in ESW. In other welding techniques, even in the case that the weld pool travels vertically, there is no substantial slag heat sources affecting the HAZ. Thus, some analogous phenomena, such as a weak thermal influence of the molten metal pool edges on the base metal above them, could be totally overshadowed.

3. HEAT AFFECTED ZONE REDUCTION

According to the understanding of various SEW practices, the relative levels of above factors are summarized in Table 14. The information in Tables 13 and 14 emphasizes the complexity of the heat transfer in ESW. For a conventional standard gap electroslag weldment, on one hand, its high heat input increases its HAZ size, but on other hand, both its high form factor and dilution, to a certain degree, decrease its HAZ size. For a narrow gap weldment, the situation is just opposite due to its reduced heat input, form factor, and dilution. Of course, two contradictory effects are surely not equivalent to each other. The final HAZ size could depend upon a variety of factors. Therefore, in order to improve the HAZ microstructure as well as its

properties, all the factors mentioned above must be carefully considered and balanced.

The best ESW process established in this study is the narrow gap/TW8544 tubular wire deposition. As a matter of fact, it indeed developed a satisfactory weld metal, but did not automatically guarantee a small HAZ as well. In a narrow gap/tubular wire ES weld, since weld penetration is reduced, the offsetting effect of heat transfer of part 2 towards part 1 becomes less, resulting in more heat in the HAZ. However, the combination of reduced penetration and weld pool depth creates a smaller bottom part of weld pool (a half ellipse), resulting in reduced heat transfer to the HAZ by part 2. Furthermore, if the total volume of flux does not decrease, the magnitude of "h" has to increase, which leads to increased heat transfer to the HAZ by part 1. Therefore, in tubular wire depositions, to reduce the total heat transfer from the weld pool to the HAZ, at least two measures should be taken: (1) reduction in gross heat input, and (2) utilization of a minimum volume of welding flux which is just sufficient to avoid arcing and lack of fusion.

TABLE 9 WELD CHARACTERISTICS OF VARIOUS ESW PROCESSES

weld process	Heat input	form factor	dilution	G	h
standard gap	high	high	high	high	high
narrow gap	low	low	low	low	low
tubular wire	low	high	low	low	*

* In tubular wire welds, if the same volume of flux is added as in solid wire welds, the value of "h" is high.
* The definitions of G and h can be found in Fig.77.

E. FUSION LINE HEAT AFFECTED ZONE TOUGHNESS

Low toughness in electroslag weldments was attributed to their coarsened grains and inhomogeneous substructures. With the help of Ni-Mo-Mn alloying additions and tubular wire design, this situation was greatly improved. Throughout the weld metal, the microstructure and properties were remarkedly refined and comparatively uniform. The overall toughness of the HAZ was better too. Then, the remaining question was how to appraise the low cleavage resistance appearing at the frontier of HAZ-1 near the fusion line in most ES welds.

To highlight the answer of this fusion line toughness problem, it is necessary to discuss the metallurgical process occurring at the fusion line. According to the fundamental understanding of fusion welding, the very front of the HAZ-1 experienced the most severe thermal cycle. Partial melting, more or less, happened there. Since the maximum temperature of the partially melted region was close to the melting point, grain coarsening inevitably occurred at the HAZ-1 of most mild steel fusion welds, resulting in a narrow potential "disaster" band near the fusionline. Variation in the usage of different fusion welding processes could only vary the width of this band and the degree of grain growth. The very front of HAZ-1 was always the weakest location to resist crack initiation and propagation, thus displaying the lowest toughness. With the increase of distance from the fusion line, toughness continuously increased as indicated in Figure 78, where the HAZ Charpy toughness data obtained from a A588 ES welds are plotted as a function of the distance from the fusion line. Generally speaking, the trend of this plot can also be applied to most welds deposited by

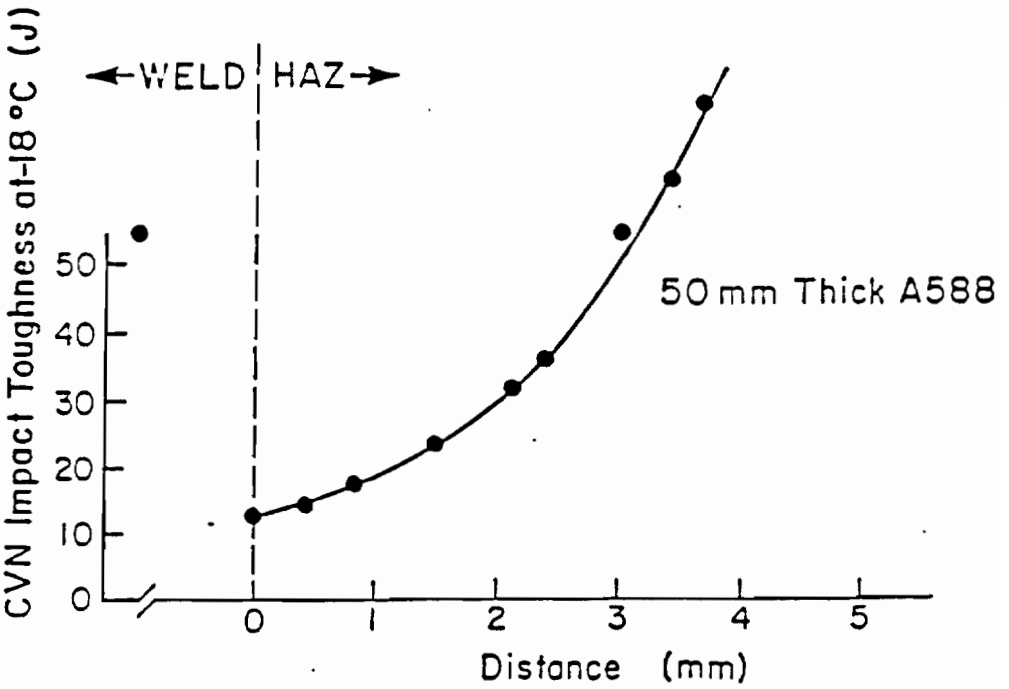

Fig. 78 The CVN impact toughness of the HAZ as a function of the distance from the fusion line

other types of fusion welding process. The only difference in the variation may be the scale of the distance term.

It is apparent that the testing site, where the notch of Charpy bars or K1c specimens is located, becomes extremely critical for any kind of welds. When joining A36 and A588 steel base metals with the GMAW or SAW processes, the sizes of the coarse grain HAZ-1 regions were around 1-2 mm and 2-3 mm respectively. The multi-pass feature of those welding techniques also made their fusion lines more ambiguous. If the standard sized CVN test bars were cut from those welds, the location of lowest toughness zone (in a 0.1-0.2mm order from the fusion line) could be rather difficult to access. As a result, the CVN impact energy data of those welds, in most cases, might not reveal the lowest toughness in the HAZ. While, the size of HAZ-1 in 50 mm and 76 mm thick ES welds of A36 and A588 steels reached 6 to 9 mm. Poor HAZ impact toughness near their fusion lines could be easily detected, since there was no difficulty making notches at about 1 mm (even less) from the fusion line. Thus, it should be borne in mind that the low toughness potential at the fusion line is a common problem for all the mild steel fusion welds, and only ES welds more clearly reveal it.

In this investigation, the K1c toughness of HAZ-1 specimens was generally higher than predicted by the CVN toughness data. This was because the K1c test used specimens much larger than the Charpy test. Along the thickness direction, a straight notch and its extended fatigue pre-crack could not keep a constant distance from the curved fusion line. The resultant fact was that the K1c toughness of HAZ-1 specimen often represented an average value. As known, K1c toughness

is more important for examining the service safety of engineering structures and full-thickness specimens are believed to behave similar to the real structural components. Therefore, this fact may lead to the suggestion that, for thick-sectional welds, the standard Charpy impact test could underestimate the actual fracture resistance of the HAZ-1.

Using the same reasoning, it could be suggested that, for small sized welds made with other common welding techniques, the HAZ Charpy test exactly resembled the situation of the HAZ K1c test for thick-walled ES welds. The standard HAZ Charpy bars of small sized welds were still too big to reveal the local low HAZ toughness at the fusionline. In addition, many other common welding techniques are frequently multi-pass process. It was definitely difficult to locate the exact fusionline for those kinds of welds. Thus, the actual meaning of the notch location on them was certainly ambiguous. Some researchers also had similar comments about this question. For example, as R. Stout pointed out [102], "overriding all of these considerations is the uncertainty about the significance of narrow bands of low toughness or low strength in the HAZ with respect to the fracture behavior of the whole weldment."

Therefore, it should be realized that, for large scale welds such as electroslag weldments, the CVN toughness of the HAZ-1 was comparatively conservative for the safety consideration of actual service, if it was measured from those locations very close to the fusion line.

VI. SUMMARY AND CONCLUSIONS

Through this investigation, the followings are concluded:

(1) A substantive correlation was found between the solidification structure and as-deposited weld metal morphology. Based on this finding, a model describing the formation sequence of ES weld metal has been suggested. The cellular dendritic to columnar dendritic transition and the kinetics of austenitic growth were the key factors affecting the products of solid state transformation in the weld metal. High form factor welds experienced their cellular dendritic to columnar dendritic transition relatively close to the fusion line, while low form factor welds experienced close to the weld center. Upon further cooling, the cellular dendritic region first transformed to coarse columnar austenite grains, followed by the formation of a high percentage of acicular ferrite. The columnar dendritic region first transformed to thin columnar austenite grains, followed by the formation of a high percentage of grain boundary ferrite and side plate ferrite.

(2) Small additions of Cr, Mo and Ni tended to promote equiaxed dendritic growth at the weld center of mild steel welds. The equiaxed dendritic structure possessed substantially improved resistance to hot cracking, permitting increased values of current and deposition rate. The presence of Cr, Ni and Mo in the weld metal also effectively inhibited the formation of grain boundary and side-plate ferrite. At an alloy content below 0.7% Cr and 0.3% Mo, Cr-Mo additions promoted the formation of acicular ferrite, and above that, resulted in a bainitic ferrite weld metal with low CVN toughness. The Ni addition, with a

series of striking metallurgical features, has a great potential to promote the formation of acicular ferrite and to improve the weld metal toughness. Ni-Mn-Mo alloying in A36 and A588 steel ES welds could create a fine acicular ferrite-predominant weld metal microstructure with impressively improved toughness.

(3) The metal powder-cored tubular filler metal exhibited several advantages over the solid filler metal, such as lower heat input, lower base metal dilution, higher deposition rate, higher form factor, and higher resistance to hot cracking. The specially designed Ni-Mn-Mo alloyed tubular filler metal, TW8544, exhibited excellent characteristics in upgrading both the CVN and K1c toughness values of A36 and A588 steel ES weldments.

(4) Electroslag welding has its special characteristic of thermal transfer. Its large molten slag pool delivers a great amount of heat to the surrounding base metals. The HAZ size in ES weldments was controlled by not only the total heat input but also the geometry of the molten weld pool.

(5) For large section welds such as electroslag weldments, the CVN impact toughness of the HAZ-1 was comparatively conservative for the safety consideration of actual service, when measured from those locations very close to the fusion line.

VII. REFERENCES

1) Hobart Brothers Co.: "Technical Guide for Electroslag welding", p.5, [1980]

2) Benter, W.P.: NCHRP Research Result Digest 74, p23, [1975]

3) Culp, J.D.: Res. Rep. #R-101, Michigan state DOT, May, [1976]

4) Einchhorn,F., Hirsch, P., and Wubbels, B.: IIW Document K11-j-76-80, [1980]

5) Andreev,V.P. and Novikova, D.R.: Auto Weld., Vol.10, p46, [1981]

6) Ann, H.S.: Paper presented at 1985 AWS Annual Meeting, Las vegas, [1985]

7) Yu, D.W., Ann, H.S., Devletian, J.H., and Wood, W.E.: in "Advances in Welding Science and Technology" (S.A. David ed.), p.267, ASM, [1986]

8) Grong, O. and Matlock, D.K.: Int. Met. Rev., Vol.10, p.46, [1986]

9) Yu, D.W., Ann, H.S., Devletian, J.H., and Wood, W.E.: in "Welding Metallurgy of Structural steels" (J.Y. Koo ed.), TMS/AIME, p.233, [1987]

10) Paton, B.: "Electroslag Welding", AWS, [1962]

11) Bentley, K.P.: BWRA Report P/18-66, [1966]

12) Shackleton, D.N.: The Weld. Ins. Report E/59/75, [1975]

13) Shackleton, D.N.: ibid DE/78/1978, [1978]

14) Shakleton, D.N.: The Weld. Ins. Bull., Nov., p339, [1975]

15) Shackleton, D.N.: Weld. J., 10, p.224-s, [1981]

16) Noel, J.S. and Troprac, A.A.: Univ. of Texas, Res. Rep. 157-1F, Proj. 3-5-71-157, Dec. [1972]

17) Culp, J.D.: Weld. J., Vol.58 (7), p.27, [1979]

18) Andersen, N.E.: Svetsaren, (1), p.9, [1973]

19) Dilawari, A.H., Eagar, T.W., and Szekely, J.: Weld. J., Vol.57(1), p.24-s, [1978]

20) Liby, A.L. and Olson, D.L.: Quarterly of Colorado Sch. of Mines, Vol. 1, p.41, [1974]

21) AWS: D1.1 "Structural Welding Code", AWS, [1982]

22) Benter, W.D. and Schilling, C.G.: NCHRP Report 201, [1979

23) Nolan, M.V. and Apps, R.L.: Weld. and Met. Fabr., Nov., p.664, [1969]

24) Mryku, E.: Auto. weld. (1), p.23, [1974]

25) Dawes, M.G.: TWI Res. and Dev., (4), p.1, [1971]

26) Sovak, I.F.: Weld. J., Vol. 60(7), p.269-s, [1981]

27) Yu, D.W., Ann, H.S., Devletian, J.H., and Wood, W.E.: in "Welding: the State of the Art" (E. Nippes ed.), p.27, ASM, [1986]

28) Medovar, B.I., Tsykulenko, A.K., Zhuk, H.V., Kareta, N.L., Markashova, L.I., and Zarivaiskaya, T.S. : Auto Weld.,(2) p.70, [1984]

29) Venkataraman, S.: Ph.D. thesis, Oregon Graduate Center, [1981]

30) Savage,W.F., Lundin, C.D., and Aronson, A.H.: Weld. J., Vol.44, p.175 [1965]

31) Savage, W.F. and Aronson A..H.: vol.45, p.85, [1966]

32) Matsuda, F.: Tran. Nat. Res. Inst. metals (Japan), (11), p,43, [1969]

33) Loper, C.R., Shideler, L.A., and Baker, R.G.: Weld. J., (4), p171, [1969]

34) Calvo, F. A., Bentley, B., and Baker, R.G.: Acta Met., (8), p.898, [1960]

35) Nakagawa, H.: J. Japan Weld. Soc., Vol. 39, p.94 [1970]

36) Nakagawa, H.: Trans. Japan Weld. Soc. (2), p.1, [1971]

37) Brown, P.E. and Adams, C.M. JR: Weld. J., Vol. 39, p. 520, [1960]

38) Brown, P.E. and Adams, C.M. JR: Trans. AFS, vol. 69, p.879,[1961]

39) Davies, G.J. and Garland, J.G.: Int. Met. Rev., Vol.20, p.89, [1975]

40) Lanzafame, J.N. and Kattamis, J.Z.: Weld.J. Vol. 52, p.226, [1973]

41) Miller, T.W.: M.S. thesis, Rensselaer Polytechic Inst., NY, [1967]

42) Bell, J.R.: M.S. thesis, ibid, [1966]

43) Bray, R.S. and Lozano, L.J.: Weld. J., Vol.44, p424, [1965]

44) Abson, D.J. and Dolby, R.E.: IIW Doc. IXj-29-80, [1980]

45) Kinsman, K.R. and Auroson, H.I.: Metal. Trans. Vol.4, p.959, [1973]

46) Choi, C.C.and Hill, D.C.: Weld. J. Vol.57(8), p232-s, [1978]

47) Howell, P.R.: J. Mat. Sci. Vol. 15, p.376, [1980]

48) Tounsend, R.D. and Kirkaldy, J.S.: Trans. ASM, Vol.61, p.605. [1968]

49) Grong, O. and Matlock, D.K.: Int. Met. Rev. Vol.31(1), p.27, [1986]

50) Bhadeshia, H.K.D.H.: J. Mat. Sci. Vol.21, p 317, [1986]

51) Oldland, R.B.: Australian Weld. Res. Dec. p.44, [1985]

52) Abson, D.J., Dolby, P.E., and Hart, P.H.M.: in proceeding of Int. conf. "Trends in Steels and Consumables for Welding", paper 25, London, [1978]

53) Cochrane, R.C. and Kirkood, R.P.: ibid, paper 35.

54) Ricks, R.A.: J. Mat. Sci. Vol.17, p732, [1982]

55) Devillers, D.J.: in "The Effect of Residual, Impurity and Micro-alloying Elements on Weldabilities", paper1, The Weld. Inst. [1984]

56) Abson, D.J. and Pargeter, R.J.: Int. Met. Rev. Vol. 31(4), p141, [1986]

57) Ann, H.S., Yu, D.W., Devletian, J.H. and Wood, W.E.: in "Advances in Welding Science and Technology ", p.615, [1986]

58) Irvine, K.J. and Pickering, F.B.: Iron and Steel, Vol.35(5), p.235, [1958]

59) Lyttle, I.E., Doschu, K.E., and Fragetta, W.A.: Weld. J., Vol.48(10), p.493-s, [1969]

60) Temlett, H.F.: Brit. Weld. J., Vol.8(9), p.437, [1961]

61) Dolby, R.E.: Weld. Inst. Res. Rep. #14/1976/M, [1976]

62) "Technical Forecast '86": Metal Progress, Vol.13(1), p.13, [1986]

63) Shiga, A.: IIW Doc. IX-880-74, [1974]

64) Evans, G.M.: Oerlikon Schweissmitt, Vol.38(90), P.4, [1980]

65) Koteck, D.J.: personal communication to K.E. Dorschu, [1977]

66) Moll, R.A. and Stout, R.D.: Weld. J., Vol.46(12), p.551-s, [1967]

67) Widgery, D.j.: Weld. J., Vol.55(3), p.57-s, [1976]

68) Evans, G.M.: Weld. J., Vol.59(3), p.57-s, [1980]

69) Dorschu, K.E.: Weld. Res. Counc. Bull., # 231, p.11, [1977]

70) Evans, G.M.: Weld. J., Vol.61(4), p.125-s, [1982]

71) Taylor, D.S.: Weld. Met. & Fabr. Vol.50(9), p.452, [1982]

72) Abson, D.J.: Res. Rep. 194/82, TWI, Abington, [1982]

73) Teledyne Inc.: UK patent # 1297865, [1972]

74) Sakaki, H.: J. Japan Weld. Soc. Vol.28(12), p.858, [1959]

75) Evans, G.M., IIW Doc. II-4-630-84, [1984]

76) Abson, D.J.: Rep. #68/1978/M, TWI, [1978]

77) Ito, Y. and Nakanishi, M.: Sumitomo Search, 15, p.42, [1976]

78) Hannerz, N.E.: IIW Doc. IX-1169-80, [1980]

79) Dorschu, K.E. and Stout, R.D.: Weld. J., Vol.40(3), p97-s, [1961]

80) Ohwa, T.: IIW Doc. II-221-62, [1962]

81) Estering, K.: "Introduction to the Physical Metallurgy of welding", Butterworths, London, [1983]

82) Honeycombe, R.W.K.: "Steels: Microstructure and Properties" ASM, [1981]

83) Sagan, S.E. and Compbell, H.C.: Weld. Res. Counc. Bull.,#59, [1960]

84) Heuschkel, J.: Weld. J., Vol.52(1), p.1-s, [1973]

85) Morigaki, K.: IIW doc. II-746-75, [1975]

86) Bosward, I.G. and John, R.: in " Trends in Steels and Consumables for Welding", TWI, p.135, [1979]

87) Hirabayash, T.: in symp. "Physical Metallurgy of weldments", AIME, [1976]

88) Judson, P. and Mckeown, D.J.: in " Offshore Welding Structures", paper 3, TWI [1983]

89) Hill, D.C. and Levine, E.: in "Physical Metallurgy of Metal Joining", (ed. R. Kossowsky and M.E. Glicksman), New york, AIME, p.36-52, [1980]

90) Flemings, M. C.: "Solidification Process", McGraw-Hill, New York, (1974)

91) Abson, D.J.: Weld. Res. Inst. Bulletian 202, p.24, [1978]

92) Brouwer, G.: Austrlian Weld. J., (7), p.153, (1971)

93) Hu, H., ed.: "The Nature and Behavior of Grain Boundaries", Plenum, New York, p.256, [1972]

94) Verhoevere, J.D.: "Fundamental of Physical Metallurgy", John Wiley & Son, Chapter 12, [1975]

95) Kato, M.: Trans. JWS, (2), p.10, [1972]

96) Porter, D.A. and Easterling, K.E.: " Phase Transformation in Metal and Alloys", Van Nostrant Reinhold, London, P.29, (1981)

97) Smallman, R.E.: "Modern Physical Metallurgy" 4th ed., Butterworths, London, [1985]

98) Brown, N and Ekvall, R.A.: Acta Met., Vol.62, p.1001, [1962]

99) Brewer, L,: "Bonding and Structure of Transition Metals", Science, Vol. 161, p.115, [1968]

100) Leslie, W.C., Sober, R.J., Babcock, S.G., and Green, S.J.: Trans. ASM, Vol.62, p.694, [1969]

101) Jolley, W.: Trans. TMS/AIME, Vol.42 (2), P.313, [1968]

102) Stout, R.: Met. Quart., Vol. 16 (4), p.1, [1976]

APPENDIX:

CVN IMPACT TEST DATA

APPENDIX : CVN IMPACT TEST DATA

Weld ID	Specimen ID	Current (A)	Voltage (V)	Zone	Temperature °F	Temperature °C	CVN Toughness ft-lb	CVN Toughness Joules
50mm A36	7PR	--	--	BM	-100	-73	3	4
50mm A36	7PJ	--	--	BM	-100	-73	3	4
50mm A36	7PF	--	--	BM	- 60	-51	6	8
50mm A36	7PP	--	--	BM	- 60	-51	7	9
50mm A36	7PJ	--	--	BM	- 30	-34	21	28
50mm A36	7PE	--	--	BM	- 30	-34	23	31
50mm A36	7PS	--	--	BM	0	-18	32	43
50mm A36	7PO	--	--	BM	0	-18	31	42
50mm A36	7PG	--	--	BM	0	-18	30	41
50mm A36	7PN	--	--	BM	32	0	67	91
50mm A36	7PC	--	--	BM	32	0	48	65
50mm A36	7PQ	--	--	BM	50	10	60	81
50mm A36	7PH	--	--	BM	50	10	60	81
50mm A36	7PT	--	--	BM	68	20	86	117
50mm A36	7PL	--	--	BM	68	20	84	117
50mm A36	7PD	--	--	BM	104	40	90	122
50mm A36	7PB	--	--	BM	104	40	93	126
50mm A36	7PM	--	--	BM	104	40	81	110
50mm A36	7PK	--	--	BM	150	65	90	122
50mm A36	7PA	--	--	BM	150	65	85	115
76mm A36	36I	--	--	BM	- 80	-62	2.5	3
76mm A36	36F	--	--	BM	- 80	-62	3.5	5
76mm A36	36G	--	--	BM	- 20	-29	3.5	5
76mm A36	36D	--	--	BM	0	-18	4.5	6
76mm A36	36C	--	--	BM	0	-18	10	14
76mm A36	36N	--	--	BM	32	0	37	50
76mm A36	36P	--	--	BM	32	0	10	14
76mm A36	36N	--	--	BM	50	10	48	65
76mm A36	36K	--	--	BM	50	10	53	72
76mm A36	36E	--	--	BM	68	20	53	72
76mm A36	36J	--	--	BM	68	20	16	22
76mm A36	36L	--	--	BM	68	20	42	57
76mm A36	36H	--	--	BM	100	38	73	99
76mm A36	36O	--	--	BM	100	38	45	61
76mm A36	36A	--	--	BM	150	65	100	135
76mm A36	36B	--	--	BM	150	65	100	135

APPENDIX : CVN IMPACT TEST DATA
(cont.)

Weld ID	Specimen ID	Current (A)	Voltage (V)	Zone	Temperature °F	Temperature °C	CVN Toughness ft-lb	CVN Toughness Joules
76mm A588	88D	--	--	BM	- 80	-62	40	54
76mm A588	88C	--	--	BM	- 80	-62	2	3
76mm A588	88J	--	--	BM	- 80	-62	3.5	5
76mm A588	881	--	--	BM	- 20	-29	1.5	2
76mm A588	88A	--	--	BM	0	-18	5	7
76mm A588	88L	--	--	BM	0	-18	9	12
76mm A588	88N	--	--	BM	32	0	59	80
76mm A588	88K	--	--	BM	32	0	37	50
76mm A588	88F	--	--	BM	50	10	70	95
76mm A588	88O	--	--	BM	50	10	80	108
76mm A588	88H	--	--	BM	68	20	68	92
76mm A588	88P	--	--	BM	68	20	56	76
76mm A588	88M	--	--	BM	100	38	89	120
76mm A588	88G	--	--	BM	100	38	92	125
76mm A588	88B	--	--	BM	150	65	120	163
76mm A588	88E	--	--	BM	150	65	114	154
50mm A588	7EH	--	--	BM	-100	-73	3	4
50mm A588	7EB	--	--	BM	-100	-73	4	5
50mm A588	7EE	--	--	BM	- 60	-51	8.5	12
50mm A588	7EN	--	--	BM	- 60	-51	6.5	9
50mm A588	7EL	--	--	BM	- 30	-34	5	7
50mm A588	7EI	--	--	BM	- 30	-34	10	14
50mm A588	7EP	--	--	BM	0	-18	8	11
50mm A588	7EG	--	--	BM	0	-18	15	20
50mm A588	7EK	--	--	BM	32	0	28	38
50mm A588	7EO	--	--	BM	32	0	31	42
50mm A588	7EJ	--	--	BM	50	10	47	64
50mm A588	7EF	--	--	BM	50	10	5	7
50mm A588	7EM	--	--	BM	68	20	35	47
50mm A588	7EC	--	--	BM	104	40	50	68
50mm A588	7EA	--	--	BM	150	65	56.5	77
50mm A588	7EQ	--	--	BM	150	65	48	65

APPENDIX : CVN IMPACT TEST DATA
(cont.)

Weld ID	Specimen ID	Current (A)	Voltage (V)	Zone	Temperature °F	Temperature °C	CVN Toughness ft-lb	CVN Toughness Joules
50mm A36 SG/25P	1DN	600	42	T/2	-100	-73	2.5	3
50mm A36 SG/25P	1DA	600	42	T/2	-100	-73	3	4
50mm A36 SG/25P	1DB	600	42	T/2	- 60	-51	9	12
50mm A36 SG/25P	1DS	600	42	T/2	- 60	-51	5	7
50mm A36 SG/25P	1DJ	600	42	T/2	- 30	-34	20	27
50mm A36 SG/25P	1DC	600	42	T/2	- 30	-34	5	7
50mm A36 SG/25P	1DT	600	42	T/2	0	-18	10	14
50mm A36 SG/25P	1DL	600	42	T/2	0	-18	27	37
50mm A36 SG/25P	1DP	600	42	T/2	0	-18	18	24
50mm A36 SG/25P	1DB	600	42	T/2	0	-18	21	28
50mm A36 SG/25P	1DQ	600	42	T/2	32	0	23	31
50mm A36 SG/25P	1DG	600	42	T/2	32	0	24	33
50mm A36 SG/25P	1DO	600	42	T/2	50	10	26	35
50mm A36 SG/25P	1DH	600	42	T/2	50	10	25	34
50mm A36 SG/25P	1DF	600	42	T/2	68	20	54	73
50mm A36 SG/25P	1DK	600	42	T/2	68	20	30	41
50mm A36 SG/25P	1DI	600	42	T/2	104	40	52	70
50mm A36 SG/25P	1DR	600	42	T/2	104	40	28	38
50mm A36 SG/25P	1DM	600	42	T/2	150	65	67	91
50mm A36 SG/25P	1DE	600	42	T/2	150	65	65	88
50mm A36 SG/25P	5DH	600	42	T/4	- 60	-51	8	11
50mm A36 SG/25P	5DN	600	42	T/4	- 60	-51	5	7
50mm A36 SG/25P	5DP	600	42	T/4	- 30	-34	5	7
50mm A36 SG/25P	5DF	600	42	T/4	- 30	-34	4	5
50mm A36 SG/25P	5DE	600	42	T/4	0	-18	19	26
50mm A36 SG/25P	5DC	600	42	T/4	0	-18	8	11
50mm A36 SG/25P	5DB	600	42	T/4	0	-18	14	19
50mm A36 SG/25P	5DO	600	42	T/4	0	-18	16.5	22
50mm A36 SG/25P	5DG	600	42	T/4	32	0	25	34
50mm A36 SG/25P	5DM	600	42	T/4	32	0	22	30
50mm A36 SG/25P	5DQ	600	42	T/4	50	10	26	35
50mm A36 SG/25P	5DK	600	42	T/4	50	10	30	41
50mm A36 SG/25P	5DR	600	42	T/4	68	20	33	45
50mm A36 SG/25P	5DL	600	42	T/4	68	20	34	46
50mm A36 SG/25P	5DJ	600	42	T/4	104	40	47	64
50mm A36 SG/25P	5DI	600	42	T/4	104	40	28	40
50mm A36 SG/25P	5DS	600	42	T/4	150	65	52	70
50mm A36 SG/25P	5DT	600	42	T/4	150	65	55	75

APPENDIX : CVN IMPACT TEST DATA
(cont.)

Weld ID	Specimen ID	Current (A)	Voltage (V)	Zone	Temperature °F	Temperature °C	CVN Toughness ft-lb	CVN Toughness Joules
50mm A36 NG/25P	6PH	1000	38	T/4	-100	-73	7	9
50mm A36 NG/25P	6PG	1000	38	T/4	- 80	-62	15	20
50mm A36 NG/25P	6PI	1000	38	T/4	- 60	-51	18	24
50mm A36 NG/25P	6PF	1000	38	T/4	- 60	-51	12	16
50mm A36 NG/25P	6PB	1000	38	T/4	- 20	-29	22	30
50mm A36 NG/25P	6PJ	1000	38	T/4	- 20	-29	14.5	20
50mm A36 NG/25P	6PC	1000	38	T/4	0	-18	29	39
50mm A36 NG/25P	6PD	1000	38	T/4	0	-18	21	28
50mm A36 NG/25P	6PK	1000	38	T/4	68	20	41	56
50mm A36 NG/25P	6PA	1000	38	T/4	100	38	42	60
50mm A36 NG/25P	6PE	1000	38	T/4	100	38	67	91
50mm A36 NG/25P	4PU	1000	38	HAZ	-100	-73	7	9
50mm A36 NG/25P	4PJ	1000	38	HAZ	-100	-73	3	4
50mm A36 NG/25P	4PQ	1000	38	HAZ	- 60	-51	12.5	17
50mm A36 NG/25P	4PK	1000	38	HAZ	- 60	-51	21	28
50mm A36 NG/25P	4PD	1000	38	HAZ	- 30	-34	8	11
50mm A36 NG/25P	4PG	1000	38	HAZ	- 30	-34	9	12
50mm A36 NG/25P	4PH	1000	38	HAZ	0	-18	35	47
50mm A36 NG/25P	4PB	1000	38	HAZ	0	-18	13	18
50mm A36 NG/25P	4PP	1000	38	HAZ	0	-18	46	62
50mm A36 NG/25P	4PB	1000	38	HAZ	0	-18	32	43
50mm A36 NG/25P	4PC	1000	38	HAZ	0	-18	14	19
50mm A36 NG/25P	4PS	1000	38	HAZ	0	-18	39	53
50mm A36 NG/25P	4PA	1000	38	HAZ	32	0	28	38
50mm A36 NG/25P	4PE	1000	38	HAZ	32	0	37	50
50mm A36 NG/25P	4PL	1000	38	HAZ	50	10	55	75
50mm A36 NG/25P	4PC	1000	38	HAZ	50	10	60	81
50mm A36 NG/25P	4PF	1000	38	HAZ	68	20	75	101
50mm A36 NG/25P	4PR	1000	38	HAZ	68	20	82	111
50mm A36 NG/25P	4PJ	1000	38	HAZ	104	40	61	83
50mm A36 NG/25P	4PO	1000	38	HAZ	104	40	90	122
50mm A36 NG/25P	4PI	1000	38	HAZ	104	40	75	102
50mm A36 NG/25P	4PN	1000	38	HAZ	150	65	97	131
50mm A36 NG/25P	4PN	1000	38	HAZ	150	65	91	123

APPENDIX : CVN IMPACT TEST DATA
(cont.)

Weld ID	Specimen ID	Current (A)	Voltage (V)	Zone	Temperature °F	Temperature °C	CVN Toughness ft-lb	CVN Toughness Joules
50mm A36 NG/ST	3RT	800	38	T/2	- 80	-62	4	5
50mm A36 NG/ST	3RJ	800	38	T/2	- 80	-62	3	4
50mm A36 NG/ST	3RG	800	38	T/2	- 60	-51	9	12
50mm A36 NG/ST	3RC	800	38	T/2	- 60	-51	8.5	12
50mm A36 NG/ST	3RE	800	38	T/2	- 20	-29	14.5	20
50mm A36 NG/ST	3RF	800	38	T/2	0	-18	49	67
50mm A36 NG/ST	3RD	800	38	T/2	32	0	65	88
50mm A36 NG/ST	3RF	800	38	T/2	32	0	59	80
50mm A36 NG/ST	3RE	800	38	T/2	68	20	59	80
50mm A36 NG/ST	3RG	800	38	T/2	100	38	75	102
50mm A36 NG/ST	3RC	800	38	T/2	150	65	79	107
50mm A36 NG/ST	3RZ	800	38	T/2	150	65	85	115
50mm A36 NG/ST	6RM	800	38	T/4	-100	-73	5.5	7
50mm A36 NG/ST	6RN	800	38	T/4	-100	-73	5	7
50mm A36 NG/ST	6RC	800	38	T/4	- 80	-62	8	11
50mm A36 NG/ST	6RH	800	38	T/4	- 80	-62	11.5	16
50mm A36 NG/ST	6RA	800	38	T/4	- 60	-51	18.5	25
50mm A36 NG/ST	6RB	800	38	T/4	- 60	-51	22	30
50mm A36 NG/ST	6RO	800	38	T/4	- 40	-40	27	37
50mm A36 NG/ST	6RZ	800	38	T/4	- 40	-40	26	35
50mm A36 NG/ST	6RD	800	38	T/4	- 20	-29	34	46
50mm A36 NG/ST	6RE	800	38	T/4	- 20	-29	27	37
50mm A36 NG/ST	6RF	800	38	T/4	0	-18	44	60
50mm A36 NG/ST	6RG	800	38	T/4	0	-18	53	72
50mm A36 NG/ST	6RQ	800	38	T/4	32	0	64	87
50mm A36 NG/ST	6RP	800	38	T/4	32	0	69	93
50mm A36 NG/ST	6RI	800	38	T/4	50	10	70	95
50mm A36 NG/ST	6RJ	800	38	T/4	50	10	75	102
50mm A36 NG/ST	6RH	800	38	T/4	68	20	74	100
50mm A36 NG/ST	6RC	800	38	T/4	68	20	75	102
50mm A36 NG/ST	6RK	800	38	T/4	104	40	80	108
50mm A36 NG/ST	6RL	800	38	T/4	104	40	76	103

APPENDIX : CVN IMPACT TEST DATA
(cont.)

Weld ID	Specimen ID	Current (A)	Voltage (V)	Zone	Temperature °F	Temperature °C	CVN Toughness ft-lb	CVN Toughness Joules
50mm A36 NG/ST	4RR	800	38	HAZ	-100	-73	3	4
50mm A36 NG/ST	4RO	800	38	HAZ	-100	-73	4.5	6
50mm A36 NG/ST	4RL	800	38	HAZ	- 60	-51	7	9
50mm A36 NG/ST	4RF	800	38	HAZ	- 60	-51	5	7
50mm A36 NG/ST	4RE	800	38	HAZ	- 30	-34	22	30
50mm A36 NG/ST	4RK	800	38	HAZ	- 30	-34	9	12
50mm A36 NG/ST	4RB	800	38	HAZ	0	-18	20	27
50mm A36 NG/ST	4RT	800	38	HAZ	0	-18	13	18
50mm A36 NG/ST	4RA	800	38	HAZ	0	-18	5	7
50mm A36 NG/ST	4RC	800	38	HAZ	32	0	32	44
50mm A36 NG/ST	4RQ	800	38	HAZ	32	0	23	31
50mm A36 NG/ST	4RH	800	38	HAZ	50	10	49	66
50mm A36 NG/ST	4RM	800	38	HAZ	50	10	56	76
50mm A36 NG/ST	4RS	800	38	HAZ	68	20	58	79
50mm A36 NG/ST	4RN	800	38	HAZ	68	20	73	99
50mm A36 NG/ST	4RI	800	38	HAZ	104	40	84	114
50mm A36 NG/ST	4RD	800	38	HAZ	150	65	81.3	110
50mm A36 NG/ST	4RP	800	38	HAZ	150	65	91	123
50mm A36 NG/ST	4YG	1000	35	HAZ	-100	-73	3.5	5
50mm A36 NG/ST	4YG	1000	35	HAZ	-100	-73	3	5
50mm A36 NG/ST	4YJ	1000	35	HAZ	- 60	-51	4	5.4
50mm A36 NG/ST	4YE	1000	35	HAZ	- 60	-51	6.5	9
50mm A36 NG/ST	4YO	1000	35	HAZ	- 30	-34	9	12
50mm A36 NG/ST	4YH	1000	35	HAZ	- 30	-34	8	11
50mm A36 NG/ST	4YB	1000	35	HAZ	0	-18	10	14
50mm A36 NG/ST	4YK	1000	35	HAZ	0	-18	8	11
50mm A36 NG/ST	4YC	1000	35	HAZ	0	-18	11	15
50mm A36 NG/ST	4YR	1000	35	HAZ	0	-18	54	73
50mm A36 NG/ST	4YM	1000	35	HAZ	32	0	49	66
50mm A36 NG/ST	4YD	1000	35	HAZ	32	0	40	54
50mm A36 NG/ST	4YC	1000	35	HAZ	50	10	45	61
50mm A36 NG/ST	4YS	1000	35	HAZ	50	10	73	99
50mm A36 NG/ST	4YF	1000	35	HAZ	68	20	67	91
50mm A36 NG/ST	4YA	1000	35	HAZ	68	20	55	75
50mm A36 NG/ST	4YN	1000	35	HAZ	104	40	85	115
50mm A36 NG/ST	4YI	1000	35	HAZ	104	40	78	106
50mm A36 NG/ST	4YL	1000	35	HAZ	150	65	104	141
50mm A36 NG/ST	4YQ	1000	35	HAZ	150	65	93	126

APPENDIX *: CVN IMPACT TEST DATA
(cont.)

Weld ID	Specimen ID	Current (A)	Voltage (V)	Zone	Temperature °F	Temperature °C	CVN Toughness ft-lb	CVN Toughness Joules
76mm A36 SG/25P	1BE	850	38	T/2	- 40	-40	2.3	3
76mm A36 SG/25P	1BD	850	38	T/2	- 40	-40	19.2	26
76mm A36 SG/25P	1BG	850	38	T/2	- 20	-29	6	8
76mm A36 SG/25P	1BF	850	38	T/2	- 20	-29	4.6	6
76mm A36 SG/25P	1BA	850	38	T/2	0	-18	13	18
76mm A36 SG/25P	1BB	850	38	T/2	0	-18	13.1	18
76mm A36 SG/25P	1BC	850	38	T/2	0	-18	13.8	19
76mm A36 SG/25P	1BQ	850	38	T/2	32	0	28	38
76mm A36 SG/25P	1BP	850	38	T/2	32	0	20	27
76mm A36 SG/25P	1BR	850	38	T/2	50	10	37.5	51
76mm A36 SG/25P	1BS	850	38	T/2	50	10	42	57
76mm A36 SG/25P	1BH	850	38	T/2	68	20	47	64
76mm A36 SG/25P	1BI	850	38	T/2	68	20	44	60
76mm A36 SG/25P	1BN	850	38	T/2	100	38	42	60
76mm A36 SG/25P	1BO	850	38	T/2	100	38	60	81
76mm A36 SG/25P	1BM	850	38	T/2	150	65	75	102
76mm A36 SG/25P	1BC	850	38	T/2	150	65	79	107
76mm A36 SG/25P	1BJ	850	38	T/2	200	93	75	102
76mm A36 SG/25P	1BK	850	38	T/2	200	93	74	100
76mm A36 SG/25P	5NN	850	38	T/4	-100	-73	3.5	5
76mm A36 SG/25P	5NK	850	38	T/4	-100	-73	2	3
76mm A36 SG/25P	5NZ	850	38	T/4	- 60	-51	6.5	9
76mm A36 SG/25P	5NS	850	38	T/4	- 60	-51	2	3
76mm A36 SG/25P	5NB	850	38	T/4	- 30	-34	3.5	5
76mm A36 SG/25P	5NQ	850	38	T/4	- 30	-34	6	8
76mm A36 SG/25P	5NG	850	38	T/4	0	-18	5	7
76mm A36 SG/25P	5NJ	850	38	T/4	0	-18	5	7
76mm A36 SG/25P	5NE	850	38	T/4	0	-18	13	18
76mm A36 SG/25P	5NL	850	38	T/4	0	-18	20	27
76mm A36 SG/25P	5ND	850	38	T/4	32	0	18	24
76mm A36 SG/25P	5NR	850	38	T/4	32	0	20	27
76mm A36 SG/25P	5NT	850	38	T/4	50	10	20	27
76mm A36 SG/25P	5NP	850	38	T/4	50	10	22	30
76mm A36 SG/25P	5NF	850	38	T/4	68	20	36	49
76mm A36 SG/25P	5NL	850	38	T/4	104	40	29	39
76mm A36 SG/25P	5NO	850	38	T/4	104	40	39	53
76mm A36 SG/25P	5NN	850	38	T/4	150	65	49	66
76mm A36 SG/25P	5NA	850	38	T/4	150	65	55	75

APPENDIX : CVN IMPACT TEST DATA
(cont.)

Weld ID	Specimen ID	Current (A)	Voltage (V)	Zone	Temperature °F	Temperature °C	CVN Toughness ft-lb	CVN Toughness Joules
76mm A36 SG/25P	2BM	850	38	HAZ	- 60	-51	4	5.4
76mm A36 SG/25P	2BL	850	38	HAZ	- 60	-51	13.5	5
76mm A36 SG/25P	2BE	850	38	HAZ	- 40	-40	4.8	7
76mm A36 SG/25P	2BD	850	38	HAZ	- 40	-40	5.2	7
76mm A36 SG/25P	2BG	850	38	HAZ	- 20	-29	6.3	9
76mm A36 SG/25P	2BF	850	38	HAZ	- 20	-29	3.6	5
76mm A36 SG/25P	2BA	850	38	HAZ	0	-18	20.3	28
76mm A36 SG/25P	2BC	850	38	HAZ	0	-18	15.5	21
76mm A36 SG/25P	2BB	850	38	HAZ	0	-18	5	7
76mm A36 SG/25P	2BR	850	38	HAZ	32	0	12	16
76mm A36 SG/25P	2BS	850	38	HAZ	32	0	18	25
76mm A36 SG/25P	2BQ	850	38	HAZ	100	38	43	58
76mm A36 SG/25P	2BP	850	38	HAZ	100	38	48	65
76mm A36 SG/25P	2BN	850	38	HAZ	150	65	75	102
76mm A36 SG/25P	2BO	850	38	HAZ	150	65	78	106
76mm A36 NG/25P	3FT	1000	40	T/2	-100	-73	1.5	2
76mm A36 NG/25P	3FP	1000	40	T/2	-100	-73	1	1
76mm A36 NG/25P	3FN	1000	40	T/2	- 70	-57	4.5	6
76mm A36 NG/25P	3FR	1000	40	T/2	- 60	-51	2	3
76mm A36 NG/25P	3FO	1000	40	T/2	- 60	-51	12	16
76mm A36 NG/25P	3FB	1000	40	T/2	- 40	-40	6.5	9
76mm A36 NG/25P	3FE	1000	40	T/2	- 30	-34	21	28
76mm A36 NG/25P	3FG	1000	40	T/2	- 30	-34	16.5	22
76mm A36 NG/25P	3FF	1000	40	T/2	0	-18	23.5	32
76mm A36 NG/25P	3FJ	1000	40	T/2	0	-18	10	14
76mm A36 NG/25P	3FI	1000	40	T/2	0	-18	20	27
76mm A36 NG/25P	3FC	1000	40	T/2	40	4	37	50
76mm A36 NG/25P	3FK	1000	40	T/2	40	4	36	49
76mm A36 NG/25P	3FO	1000	40	T/2	68	20	30	41
76mm A36 NG/25P	3FM	1000	40	T/2	68	20	45	61
76mm A36 NG/25P	3FH	1000	40	T/2	100	38	45	61
76mm A36 NG/25P	3FA	1000	40	T/2	100	38	41	56
76mm A36 NG/25P	3FL	1000	40	T/2	125	51	48	65
76mm A36 NG/25P	3FS	1000	40	T/2	125	51	50	68
76mm A36 NG/25P	3FB	1000	40	T/2	150	65	55	75
76mm A36 NG/25P	3FU	1000	40	T/2	150	65	55	75

APPENDIX : CVN IMPACT TEST DATA
(cont.)

Weld ID	Specimen ID	Current (A)	Voltage (V)	Zone	Temperature °F	Temperature °C	CVN Toughness ft-lb	CVN Toughness Joules
76mm A36 NG/25P	6FA	1000	40	T/4	-100	-73	5	7
76mm A36 NG/25P	6FF	1000	40	T/4	-100	-73	1.5	2
76mm A36 NG/25P	6FT	1000	40	T/4	- 70	-57	1.5	2
76mm A36 NG/25P	6FP	1000	40	T/4	- 60	-51	5	7
76mm A36 NG/25P	6FK	1000	40	T/4	- 60	-51	13.5	18
76mm A36 NG/25P	6FQ	1000	40	T/4	- 40	-40	7	9
76mm A36 NG/25P	6FM	1000	40	T/4	- 30	-34	15.1	20
76mm A36 NG/25P	6FI	1000	40	T/4	- 30	-34	7	9
76mm A36 NG/25P	6FN	1000	40	T/4	0	-18	25	34
76mm A36 NG/25P	6FS	1000	40	T/4	0	-18	16	22
76mm A36 NG/25P	6FD	1000	40	T/4	40	4	32	44
76mm A36 NG/25P	6FE	1000	40	T/4	68	20	40	54
76mm A36 NG/25P	6FC	1000	40	T/4	68	20	49	66
76mm A36 NG/25P	6FL	1000	40	T/4	100	38	41	56
76mm A36 NG/25P	6FG	1000	40	T/4	100	38	42	57
76mm A36 NG/25P	6FO	1000	40	T/4	100	38	46	62
76mm A36 NG/25P	6FB	1000	40	T/4	125	51	51	69
76mm A36 NG/25P	6FR	1000	40	T/4	125	51	44	60
76mm A36 NG/25P	6FP	1000	40	T/4	150	65	77	104
76mm A36 NG/25P	6FH	1000	40	T/4	150	65	54	73
76mm A36 NG/25P	4FI	1000	40	HAZ	-100	-73	2	3
76mm A36 NG/25P	4FF	1000	40	HAZ	- 80	-62	8	11
76mm A36 NG/25P	4FP	1000	40	HAZ	- 80	-62	3	4
76mm A36 NG/25P	4FI	1000	40	HAZ	- 60	-51	6	8
76mm A36 NG/25P	4FE	1000	40	HAZ	- 60	-51	6	8
76mm A36 NG/25P	4FD	1000	40	HAZ	- 60	-51	3.5	5
76mm A36 NG/25P	4FR	1000	40	HAZ	- 60	-51	4.5	6
76mm A36 NG/25P	4FS	1000	40	HAZ	- 20	-29	4	5
76mm A36 NG/25P	4FE	1000	40	HAZ	- 20	-29	10	14
76mm A36 NG/25P	4FG	1000	40	HAZ	0	-18	20	27
76mm A36 NG/25P	4FN	1000	40	HAZ	0	-18	9	12
76mm A36 NG/25P	4FO	1000	40	HAZ	32	10	35.5	48
76mm A36 NG/25P	4FM	1000	40	HAZ	32	10	30.5	41
76mm A36 NG/25P	4FA	1000	40	HAZ	68	20	45	61
76mm A36 NG/25P	4FL	1000	40	HAZ	100	38	60	81
76mm A36 NG/25P	4FC	1000	40	HAZ	100	38	84	114
76mm A36 NG/25P	4FH	1000	40	HAZ	150	65	73	99
76mm A36 NG/25P	4FQ	1000	40	HAZ	150	65	91	123

APPENDIX : CVN IMPACT TEST DATA
(cont.)

Weld ID	Specimen ID	Current (A)	Voltage (V)	Zone	Temperature °F	Temperature °C	CVN Toughness ft-lb	CVN Toughness Joules
76mm A36 NG/ST	3JJ	1000	38	T/2	-100	-73	1.5	2
76mm A36 NG/ST	3JP	1000	38	T/2	-100	-73	1	1.3
76mm A36 NG/ST	3JC	1000	38	T/2	- 60	-51	3	4
76mm A36 NG/ST	3JI	1000	38	T/2	- 60	-51	3	4
76mm A36 NG/ST	3JA	1000	38	T/2	- 40	-40	9.5	13
76mm A36 NG/ST	3JR	1000	38	T/2	- 40	-40	4.5	6
76mm A36 NG/ST	3JM	1000	38	T/2	- 40	-40	4.5	6
76mm A36 NG/ST	3JJ	1000	38	T/2	- 30	-34	18	24
76mm A36 NG/ST	3JG	1000	38	T/2	- 30	-34	2	3
76mm A36 NG/ST	3JT	1000	38	T/2	- 30	-34	3.5	5
76mm A36 NG/ST	3JF	1000	38	T/2	0	-18	24	33
76mm A36 NG/ST	3JL	1000	38	T/2	0	-18	18	24
76mm A36 NG/ST	3JS	1000	38	T/2	34	1	7	9
76mm A36 NG/ST	3JH	1000	38	T/2	34	1	19	26
76mm A36 NG/ST	3JQ	1000	38	T/2	34	1	13.5	18
76mm A36 NG/ST	3JD	1000	38	T/2	68	20	23	31
76mm A36 NG/ST	3JM	1000	38	T/2	68	20	23	31
76mm A36 NG/ST	3JE	1000	38	T/2	100	38	41	36
76mm A36 NG/ST	3JN	1000	38	T/2	100	38	39	53
76mm A36 NG/ST	3JB	1000	38	T/2	125	51	49	66
76mm A36 NG/ST	3JK	1000	38	T/2	125	51	48	65
76mm A36 NG/ST	6JB	1000	38	T/4	-100	-73	3	4
76mm A36 NG/ST	6JC	1000	38	T/4	-100	-73	1.0	1.3
76mm A36 NG/ST	6JJ	1000	38	T/4	- 60	-51	2	3
76mm A36 NG/ST	6JH	1000	38	T/4	- 60	-51	2	3
76mm A36 NG/ST	6JP	1000	38	T/4	- 30	-34	3	5
76mm A36 NG/ST	6JQ	1000	38	T/4	- 30	-34	3.5	5
76mm A36 NG/ST	6JR	1000	38	T/4	0	-18	7.5	10
76mm A36 NG/ST	6JN	1000	38	T/4	0	-18	13	18
76mm A36 NG/ST	6JK	1000	38	T/4	34	1	24	33
76mm A36 NG/ST	6JL	1000	38	T/4	34	1	30	41
76mm A36 NG/ST	6JD	1000	38	T/4	68	20	30	41
76mm A36 NG/ST	6JA	1000	38	T/4	68	20	29	39
76mm A36 NG/ST	6JF	1000	38	T/4	68	20	39	53
76mm A36 NG/ST	6JE	1000	38	T/4	100	38	35	47
76mm A36 NG/ST	6JS	1000	38	T/4	100	38	43	58
76mm A36 NG/ST	6JM	1000	38	T/4	125	51	56	76
76mm A36 NG/ST	6JO	1000	38	T/4	125	51	54	73

APPENDIX : CVN IMPACT TEST DATA
(cont.)

Weld ID	Specimen ID	Current (A)	Voltage (V)	Zone	Temperature °F	Temperature °C	CVN Toughness ft-lb	CVN Toughness Joules
76mm A36 NG/ST	4JE	1000	38	HAZ	- 60	-51	4	5
76mm A36 NG/ST	4JL	1000	38	HAZ	- 60	-51	4.5	6
76mm A36 NG/ST	4JN	1000	38	HAZ	- 20	-29	6.5	9
76mm A36 NG/ST	4JP	1000	38	HAZ	- 20	-29	10	13
76mm A36 NG/ST	4JF	1000	38	HAZ	0	-18	14	19
76mm A36 NG/ST	4JS	1000	38	HAZ	0	-18	10	13
76mm A36 NG/ST	4JK	1000	38	HAZ	0	-18	32	43
76mm A36 NG/ST	4JA	1000	38	HAZ	32	0	18	24
76mm A36 NG/ST	4JT	1000	38	HAZ	32	0	12.5	17
76mm A36 NG/ST	4JH	1000	38	HAZ	68	20	30	41
76mm A36 NG/ST	4JC	1000	38	HAZ	68	20	22	30
76mm A36 NG/ST	4JV	1000	38	HAZ	100	38	85	115
76mm A36 NG/ST	4JI	1000	38	HAZ	100	38	38	51
76mm A36 NG/ST	4JJ	1000	38	HAZ	150	65	86	117
76mm A36 NG/ST	4JG	1000	38	HAZ	150	65	98	133
76mm A36 NG/ST2	3ZE	1300	35	T/2	-100	-73	3.5	5
76mm A36 NG/ST2	3ZQ	1300	35	T/2	-100	-73	4	5
76mm A36 NG/ST2	3ZN	1300	35	T/2	- 60	-51	4	5
76mm A36 NG/ST2	3ZR	1300	35	T/2	- 60	-51	5.5	7
76mm A36 NG/ST2	3ZL	1300	35	T/2	- 30	-34	11	15
76mm A36 NG/ST2	3ZS	1300	35	T/2	- 30	-34	4	5
76mm A36 NG/ST2	3ZJ	1300	35	T/2	0	-18	7	9
76mm A36 NG/ST2	3ZD	1300	35	T/2	0	-18	33	44
76mm A36 NG/ST2	3ZT	1300	35	T/2	0	-18	43	58
76mm A36 NG/ST2	3ZB	1300	35	T/2	0	-18	22	30
76mm A36 NG/ST2	3ZH	1300	35	T/2	32	0	32	43
76mm A36 NG/ST2	3ZI	1300	35	T/2	32	0	57	79
76mm A36 NG/ST2	3ZD	1300	35	T/2	50	10	29	39
76mm A36 NG/ST2	3ZF	1300	35	T/2	50	10	29	39
76mm A36 NG/ST2	3ZA	1300	35	T/2	68	20	55	75
76mm A36 NG/ST2	3ZM	1300	35	T/2	68	20	53	71
76mm A36 NG/ST2	3ZC	1300	35	T/2	104	40	53	71
76mm A36 NG/ST2	3ZP	1300	35	T/2	104	40	68	92
76mm A36 NG/ST2	3ZG	1300	35	T/2	150	65	81	110
76mm A36 NG/ST2	3ZK	1300	35	T/2	150	65	69	94

APPENDIX : CVN IMPACT TEST DATA
(cont.)

Weld ID	Specimen ID	Current (A)	Voltage (V)	Zone	Temperature °F	Temperature °C	CVN Toughness ft-lb	CVN Toughness Joules
76mm A36 NG/ST2	6ZT	1300	35	T/4	-100	-73	3	4
76mm A36 NG/ST2	6ZP	1300	35	T/4	-100	-73	2	3
76mm A36 NG/ST2	6ZO	1300	35	T/4	- 60	-51	3	4
76mm A36 NG/ST2	6ZA	1300	35	T/4	- 60	-51	3	4
76mm A36 NG/ST2	6ZE	1300	35	T/4	- 30	-34	14	19
76mm A36 NG/ST2	6ZL	1300	35	T/4	- 30	-34	5	7
76mm A36 NG/ST2	6ZH	1300	35	T/4	0	-18	32	43
76mm A36 NG/ST2	6ZF	1300	35	T/4	0	-18	38	51
76mm A36 NG/ST2	6ZJ	1300	35	T/4	0	-18	36	48
76mm A36 NG/ST2	6ZS	1300	35	T/4	32	0	45	61
76mm A36 NG/ST2	6ZM	1300	35	T/4	32	0	24	33
76mm A36 NG/ST2	6ZG	1300	35	T/4	50	10	38	51
76mm A36 NG/ST2	6ZN	1300	35	T/4	50	10	49	66
76mm A36 NG/ST2	6ZD	1300	35	T/4	68	20	51	69
76mm A36 NG/ST2	6ZS	1300	35	T/4	68	20	51	69
76mm A36 NG/ST2	6ZI	1300	35	T/4	104	40	62	84
76mm A36 NG/ST2	6ZQ	1300	35	T/4	104	40	24	33
76mm A36 NG/ST2	6ZC	1300	35	T/4	150	65	81	110
76mm A36 NG/ST2	6ZB	1300	35	T/4	150	65	72	98
76mm A36 NG/ST2	4ZK	1300	35	HAZ	-100	-73	3	4
76mm A36 NG/ST2	4ZH	1300	35	HAZ	-100	-73	3	4
76mm A36 NG/ST2	4ZS	1300	35	HAZ	- 60	-51	6	8
76mm A36 NG/ST2	4ZJ	1300	35	HAZ	- 60	-51	2.5	3
76mm A36 NG/ST2	4ZC	1300	35	HAZ	- 30	-34	8	11
76mm A36 NG/ST2	4ZG	1300	35	HAZ	- 30	-34	7	9
76mm A36 NG/ST2	4ZI	1300	35	HAZ	0	-18	20	27
76mm A36 NG/ST2	4ZA	1300	35	HAZ	0	-18	9	12
76mm A36 NG/ST2	4ZM	1300	35	HAZ	0	-18	13	18
76mm A36 NG/ST2	4ZF	1300	35	HAZ	0	-18	30	41
76mm A36 NG/ST2	4ZE	1300	35	HAZ	32	0	22	30
76mm A36 NG/ST2	4ZN	1300	35	HAZ	32	0	8	11
76mm A36 NG/ST2	4ZQ	1300	35	HAZ	50	10	47	64
76mm A36 NG/ST2	4ZL	1300	35	HAZ	50	10	66	89
76mm A36 NG/ST2	4ZP	1300	35	HAZ	68	20	38	52
76mm A36 NG/ST2	4ZO	1300	35	HAZ	68	20	21	29
76mm A36 NG/ST2	4ZI	1300	35	HAZ	104	40	52	71
76mm A36 NG/ST2	4ZR	1300	35	HAZ	104	40	66	90
76mm A36 NG/ST2	4ZB	1300	35	HAZ	150	65	74	100
76mm A36 NG/ST2	4ZT	1300	35	HAZ	150	65	104	141

APPENDIX : CVN IMPACT TEST DATA
(cont.)

Weld ID	Specimen ID	Current (A)	Voltage (V)	Zone	Temperature °F	Temperature °C	CVN Toughness ft-lb	CVN Toughness Joules
50mm A588 SG/WS	1EE	600	42	T/2	- 40	-40	2.7	4
50mm A588 SG/WS	1ED	600	42	T/2	- 40	-40	13.7	19
50mm A588 SG/WS	1EF	600	42	T/2	- 20	-29	17.7	24
50mm A588 SG/WS	1EG	600	42	T/2	- 20	-29	3.5	5
50mm A588 SG/WS	1EB	600	42	T/2	0	-18	9	12
50mm A588 SG/WS	1EC	600	42	T/2	0	-18	5	7
50mm A588 SG/WS	1EA	600	42	T/2	0	-18	7	9
50mm A588 SG/WS	1EQ	600	42	T/2	32	0	25	34
50mm A588 SG/WS	1ER	600	42	T/2	32	0	25	34
50mm A588 SG/WS	1ET	600	42	T/2	50	10	31	42
50mm A588 SG/WS	1ES	600	42	T/2	50	10	30	41
50mm A588 SG/WS	1EH	600	42	T/2	68	20	33.5	45
50mm A588 SG/WS	1EI	600	42	T/2	68	20	41	56
50mm A588 SG/WS	1EP	600	42	T/2	100	38	40	54
50mm A588 SG/WS	1ED	600	42	T/2	100	38	48.5	66
50mm A588 SG/WS	1EL	600	42	T/2	150	65	55	75
76mm A36 NG/ST2	1EN	600	42	T/2	150	65	50	68
50mm A588 SG/WS	5EQ	600	42	T/4	-100	-73	5	7
50mm A588 SG/WS	5EH	600	42	T/4	- 60	-51	4	5
50mm A588 SG/WS	5EI	600	42	T/4	- 60	-51	2.5	3
50mm A588 SG/WS	5ED	600	42	T/4	- 30	-34	20	27
50mm A588 SG/WS	5EA	600	42	T/4	- 30	-34	4	5
50mm A588 SG/WS	5EB	600	42	T/4	0	-18	6	8
50mm A588 SG/WS	5EP	600	42	T/4	0	-18	5	7
50mm A588 SG/WS	5EL	600	42	T/4	32	0	34	46
50mm A588 SG/WS	5EK	600	42	T/4	32	0	7	9
50mm A588 SG/WS	5EJ	600	42	T/4	50	10	25	34
50mm A588 SG/WS	5ER	600	42	T/4	50	10	27	37
50mm A588 SG/WS	5EN	600	42	T/4	68	20	41	56
50mm A588 SG/WS	5EG	600	42	T/4	68	20	30	41
50mm A588 SG/WS	5ET	600	42	T/4	104	40	40	54
50mm A588 SG/WS	5EC	600	42	T/4	104	40	47	64
50mm A588 SG/WS	5EF	600	42	T/4	150	65	60	81
50mm A588 SG/WS	5EE	600	42	T/4	150	65	55	75

APPENDIX : CVN IMPACT TEST DATA
(cont.)

Weld ID	Specimen ID	Current (A)	Voltage (V)	Zone	Temperature °F	Temperature °C	CVN Toughness ft-lb	CVN Toughness Joules
50mm A588 SG/WS	2EL	600	42	HAZ	- 60	-51	1	2
50mm A588 SG/WS	2EM	600	42	HAZ	- 60	-51	3	4
50mm A588 SG/WS	2EE	600	42	HAZ	- 40	-40	6	8
50mm A588 SG/WS	2ED	600	42	HAZ	- 40	-40	9	12
50mm A588 SG/WS	2EF	600	42	HAZ	- 20	-29	4	5
50mm A588 SG/WS	2EG	600	42	HAZ	- 20	-29	6.2	8
50mm A588 SG/WS	2EA	600	42	HAZ	0	-18	4	5
50mm A588 SG/WS	2EC	600	42	HAZ	0	-18	6.2	8
50mm A588 SG/WS	2EB	600	42	HAZ	0	-18	25.3	34
50mm A588 SG/WS	2ER	600	42	HAZ	32	0	10.5	14
50mm A588 SG/WS	2ES	600	42	HAZ	32	0	22	30
50mm A588 SG/WS	2EQ	600	42	HAZ	100	38	36	49
50mm A588 SG/WS	2EP	600	42	HAZ	100	38	20	27
50mm A588 SG/WS	2EN	600	42	HAZ	150	65	50	68
50mm A588 SG/WS	2EC	600	42	HAZ	150	65	56	76
50mm A588 SG/WS	2EK	600	42	HAZ	200	93	94	127
50mm A588 SG/WS	2EJ	600	42	HAZ	200	93	84.5	114
50mm A588 NG/WS	3QI	1000	38	T/2	-100	-73	5	7
50mm A588 NG/WS	3QE	1000	38	T/2	-100	-73	4	5
50mm A588 NG/WS	3QP	1000	38	T/2	- 60	-51	12	16
50mm A588 NG/WS	3QJ	1000	38	T/2	- 60	-51	8	11
50mm A588 NG/WS	3QF	1000	38	T/2	- 30	-34	10	14
50mm A588 NG/WS	3QA	1000	38	T/2	- 30	-34	9	12
50mm A588 NG/WS	3QD	1000	38	T/2	0	-18	9	12
50mm A588 NG/WS	3QM	1000	38	T/2	0	-18	10	14
50mm A588 NG/WS	3QQ	1000	38	T/2	0	-18	20	27
50mm A588 NG/WS	3QB	1000	38	T/2	0	-18	13	18
50mm A588 NG/WS	3QN	1000	38	T/2	32	0	18	24
50mm A588 NG/WS	3QC	1000	38	T/2	32	0	38	51
50mm A588 NG/WS	3QL	1000	38	T/2	50	10	54	73
50mm A588 NG/WS	3QH	1000	38	T/2	50	10	43	58
50mm A588 NG/WS	3QR	1000	38	T/2	68	20	70	95
50mm A588 NG/WS	3QS	1000	38	T/2	68	20	73	99
50mm A588 NG/WS	3QG	1000	38	T/2	104	40	57	99
50mm A588 NG/WS	3QS	1000	38	T/2	104	40	66	89
50mm A588 SG/WS	3QT	1000	38	T/2	150	65	77	104
50mm A588 SG/WS	3QK	1000	38	T/2	150	65	75	102

APPENDIX : CVN IMPACT TEST DATA
(cont.)

Weld ID	Specimen ID	Current (A)	Voltage (V)	Zone	Temperature °F	Temperature °C	CVN Toughness ft-lb	CVN Toughness Joules
50mm A588 NG/WS	6QJ	1000	38	T/4	-100	-73	1	1.4
50mm A588 NG/WS	6QL	1000	38	T/4	- 60	-51	3	4
50mm A588 NG/WS	6QI	1000	38	T/4	- 60	-51	3	4
50mm A588 NG/WS	6QE	1000	38	T/4	- 30	-34	8	11
50mm A588 NG/WS	6QG	1000	38	T/4	- 30	-34	7	9
50mm A588 NG/WS	6QN	1000	38	T/4	0	-18	18	24
50mm A588 NG/WS	6QP	1000	38	T/4	0	-18	8	11
50mm A588 NG/WS	6QF	1000	38	T/4	32	0	31	42
50mm A588 NG/WS	6QH	1000	38	T/4	50	10	45	61
50mm A588 NG/WS	6QM	1000	38	T/4	50	10	59	80
50mm A588 NG/WS	6QK	1000	38	T/4	68	20	46	62
50mm A588 NG/WS	6QA	1000	38	T/4	68	20	52	70
50mm A588 NG/WS	6QC	1000	38	T/4	125	51	76	103
50mm A588 NG/WS	6QB	1000	38	T/4	150	65	79	107
50mm A588 NG/WS	6QO	1000	38	T/4	150	65	76	103
50mm A588 NG/WS	4QN	1000	38	HAZ	-100	-73	4	5
50mm A588 NG/WS	4QQ	1000	38	HAZ	- 60	-51	4	5
50mm A588 NG/WS	4QD	1000	38	HAZ	- 60	-51	5.5	7
50mm A588 NG/WS	4QA	1000	38	HAZ	- 30	-34	6	8
50mm A588 NG/WS	4QJ	1000	38	HAZ	- 30	-34	5.5	7
50mm A588 NG/WS	4QP	1000	38	HAZ	0	-18	9	12
50mm A588 NG/WS	4QO	1000	38	HAZ	0	-18	11	15
50mm A588 NG/WS	4QG	1000	38	HAZ	32	0	15	20
50mm A588 NG/WS	4QE	1000	38	HAZ	50	10	19	26
50mm A588 NG/WS	4QS	1000	38	HAZ	50	10	15	20
50mm A588 NG/WS	4QH	1000	38	HAZ	68	20	29	39
50mm A588 NG/WS	4QK	1000	38	HAZ	68	20	26	35
50mm A588 NG/WS	4QF	1000	38	HAZ	100	38	31	42
50mm A588 NG/WS	4QI	1000	38	HAZ	100	38	30	40
50mm A588 NG/WS	4QC	1000	38	HAZ	125	51	55	75
50mm A588 NG/WS	4QT	1000	38	HAZ	125	51	60	81
50mm A588 NG/WS	4QM	1000	38	HAZ	150	65	72	98

APPENDIX : CVN IMPACT TEST DATA
(cont.)

Weld ID	Specimen ID	Current (A)	Voltage (V)	Zone	Temperature °F	Temperature °C	CVN Toughness ft-lb	CVN Toughness Joules
50mm A588 NG/ST	3SP	1000	38	T/2	-100	-73	9	12
50mm A588 NG/ST	3SA	1000	38	T/2	-100	-73	6	8
50mm A588 NG/ST	3SH	1000	38	T/2	- 60	-51	6.6	9
50mm A588 NG/ST	3SB	1000	38	T/2	- 60	-51	6.7	9
50mm A588 NG/ST	3SE	1000	38	T/2	- 30	-34	22	30
50mm A588 NG/ST	3SK	1000	38	T/2	- 30	-34	21	28
50mm A588 NG/ST	3SE	1000	38	T/2	0	-18	29	39
50mm A588 NG/ST	3SD	1000	38	T/2	0	-18	34	46
50mm A588 NG/ST	3SI	1000	38	T/2	32	0	49	66
50mm A588 NG/ST	3SF	1000	38	T/2	50	10	50	68
50mm A588 NG/ST	3SO	1000	38	T/2	50	10	77	104
50mm A588 NG/ST	3SN	1000	38	T/2	68	20	77	104
50mm A588 NG/ST	3SL	1000	38	T/2	100	38	82	111
50mm A588 NG/ST	3SC	1000	38	T/2	100	38	72	98
50mm A588 NG/ST	3SJ	1000	38	T/2	150	65	74	100
50mm A588 NG/ST	3SM	1000	38	T/2	150	65	88	119
50mm A588 NG/ST	6SL	800	38	T/4	-100	-73	4.5	6
50mm A588 NG/ST	6SJ	800	38	T/4	- 60	-51	8.2	11
50mm A588 NG/ST	6SM	800	38	T/4	- 60	-51	9.2	12
50mm A588 NG/ST	6SP	800	38	T/4	- 30	-34	35	47
50mm A588 NG/ST	6SB	800	38	T/4	- 30	-34	8	11
50mm A588 NG/ST	6SE	800	38	T/4	0	-18	24.5	33
50mm A588 NG/ST	6SO	800	38	T/4	0	-18	38	51
50mm A588 NG/ST	6SI	800	38	T/4	32	0	44	65
50mm A588 NG/ST	6SZ	800	38	T/4	32	0	37	50
50mm A588 NG/ST	6SF	800	38	T/4	50	10	23	31
50mm A588 NG/ST	6SG	800	38	T/4	50	10	25	34
50mm A588 NG/ST	6SN	800	38	T/4	68	20	48	65
50mm A588 NG/ST	6SK	800	38	T/4	68	20	45	61
50mm A588 NG/ST	6SC	800	38	T/4	100	38	71	96
50mm A588 NG/ST	6SH	800	38	T/4	150	65	90	122
50mm A588 NG/ST	6SA	800	38	T/4	150	65	80	108

APPENDIX : CVN IMPACT TEST DATA
(cont.)

Weld ID	Specimen ID	Current (A)	Voltage (V)	Zone	Temperature °F	Temperature °C	CVN Toughness ft-lb	CVN Toughness Joules
50mm A588 NG/ST	4SJ	800	38	HAZ	-100	-73	7	9
50mm A588 NG/ST	4SB	800	38	HAZ	-100	-73	3	4
50mm A588 NG/ST	4SP	800	38	HAZ	- 60	-51	9.5	13
50mm A588 NG/ST	4SE	800	38	HAZ	- 60	-51	4.5	6
50mm A588 NG/ST	4SC	800	38	HAZ	- 30	-34	7.2	10
50mm A588 NG/ST	4SA	800	38	HAZ	- 30	-34	8.5	12
50mm A588 NG/ST	4SF	800	38	HAZ	0	-18	12	16
50mm A588 NG/ST	4ST	800	38	HAZ	0	-18	18.5	25
50mm A588 NG/ST	4SL	800	38	HAZ	50	10	21	28
50mm A588 NG/ST	4SD	800	38	HAZ	50	10	23	31
50mm A588 NG/ST	4SR	800	38	HAZ	68	20	41	56
50mm A588 NG/ST	4SN	800	38	HAZ	100	38	56	76
50mm A588 NG/ST	4SS	800	38	HAZ	100	38	50	68
50mm A588 NG/ST	4SC	800	38	HAZ	125	51	57	77
50mm A588 NG/ST	4SO	800	38	HAZ	150	65	86	117
50mm A588 NG/ST	4SK	800	38	HAZ	150	65	82	111
76mm A588 SG/WS	1AD	850	38	T/2	- 40	-40	2.2	3
76mm A588 SG/WS	1AC	850	38	T/2	- 40	-40	2.2	3
76mm A588 SG/WS	1AE	850	38	T/2	- 20	-29	3.4	4.6
76mm A588 SG/WS	1AF	850	38	T/2	- 20	-29	3	4
76mm A588 SG/WS	1AA	850	38	T/2	0	-18	7	9
76mm A588 SG/WS	1AB	850	38	T/2	0	-18	4	5
76mm A588 SG/WS	1AO	850	38	T/2	32	0	7	9
76mm A588 SG/WS	1AP	850	38	T/2	32	0	8	11
76mm A588 SG/WS	1AQ	850	38	T/2	50	10	19	26
76mm A588 SG/WS	1AR	850	38	T/2	50	10	10	14
76mm A588 SG/WS	1AH	850	38	T/2	68	20	42.5	58
76mm A588 SG/WS	1AG	850	38	T/2	68	20	34.5	48
76mm A588 SG/WS	1AN	850	38	T/2	100	38	45	61
76mm A588 SG/WS	1AM	850	38	T/2	100	38	49	66
76mm A588 SG/WS	1AK	850	38	T/2	150	65	62	84
76mm A588 SG/WS	1AL	850	38	T/2	150	65	64	87
76mm A588 SG/WS	1AI	850	38	T/2	200	93	72	98

APPENDIX : CVN IMPACT TEST DATA
(cont.)

Weld ID	Specimen ID	Current (A)	Voltage (V)	Zone	Temperature °F	Temperature °C	CVN Toughness ft-lb	CVN Toughness Joules
76mm A588 SG/WS	5AE	850	38	T/4	- 65	-53	2	3
76mm A588 SG/WS	5AM	850	38	T/4	- 65	-53	2	3
76mm A588 SG/WS	5AL	850	38	T/4	- 20	-29	2	3
76mm A588 SG/WS	5AC	850	38	T/4	0	-18	3	4
76mm A588 SG/WS	5AD	850	38	T/4	0	-18	4	5
76mm A588 SG/WS	5AG	850	38	T/4	50	10	14	19
76mm A588 SG/WS	5AH	850	38	T/4	50	10	16.5	22
76mm A588 SG/WS	5AB	850	38	T/4	68	20	21	28
76mm A588 SG/WS	5AI	850	38	T/4	68	20	20	27
76mm A588 SG/WS	5AA	850	38	T/4	104	40	63	85
76mm A588 SG/WS	5AK	850	38	T/4	104	40	61	83
76mm A588 SG/WS	5AF	850	38	T/4	160	68	71	96
76mm A588 SG/WS	5AJ	850	38	T/4	160	68	68	92
76mm A588 SG/WS	2AD	850	38	HAZ	- 40	-40	1.5	2
76mm A588 SG/WS	2AC	850	38	HAZ	- 40	-40	1.5	2
76mm A588 SG/WS	2AE	850	38	HAZ	- 20	-29	3.3	4
76mm A588 SG/WS	2AF	850	38	HAZ	- 20	-29	3.6	4
76mm A588 SG/WS	2AA	850	38	HAZ	0	-18	2	3
76mm A588 SG/WS	2AB	850	38	HAZ	0	-18	2.7	4
76mm A588 SG/WS	2AO	850	38	HAZ	32	0	4	5
76mm A588 SG/WS	2AQ	850	38	HAZ	50	10	3	4
76mm A588 SG/WS	2AR	850	38	HAZ	50	10	3	4
76mm A588 SG/WS	2AH	850	38	HAZ	68	20	16	22
76mm A588 SG/WS	2AG	850	38	HAZ	68	20	5	7
76mm A588 SG/WS	2AN	850	38	HAZ	100	38	12	16
76mm A588 SG/WS	2AT	850	38	HAZ	100	38	13	18
76mm A588 SG/WS	2AL	850	38	HAZ	150	65	27	37
76mm A588 SG/WS	2AI	850	38	HAZ	200	93	75	102
76mm A588 SG/WS	2AJ	850	38	HAZ	200	93	41.5	56

APPENDIX : CVN IMPACT TEST DATA
(cont.)

Weld ID	Specimen ID	Current (A)	Voltage (V)	Zone	Temperature °F	Temperature °C	CVN Toughness ft-lb	CVN Toughness Joules
76mm A588 NG/WS	3HL	1000	38	T/2	-100	-73	1	1.4
76mm A588 NG/WS	3HI	1000	38	T/2	- 60	-51	1.5	2
76mm A588 NG/WS	3HE	1000	38	T/2	- 60	-51	1.5	2
76mm A588 NG/WS	3HG	1000	38	T/2	- 30	-34	2.2	3
76mm A588 NG/WS	3HT	1000	38	T/2	- 30	-34	2	3
76mm A588 NG/WS	3HK	1000	38	T/2	0	-18	3.5	5
76mm A588 NG/WS	3HJ	1000	38	T/2	50	10	5	7
76mm A588 NG/WS	3HH	1000	38	T/2	50	10	9	12
76mm A588 NG/WS	3HA	1000	38	T/2	68	20	14	19
76mm A588 NG/WS	3HB	1000	38	T/2	68	20	12.5	17
76mm A588 NG/WS	3HD	1000	38	T/2	100	38	26	35
76mm A588 NG/WS	3HM	1000	38	T/2	100	38	34	46
76mm A588 NG/WS	3HP	1000	38	T/2	125	52	59	80
76mm A588 NG/WS	3HC	1000	38	T/2	125	52	50	68
76mm A588 NG/WS	3HO	1000	38	T/2	150	65	53	72
76mm A588 NG/WS	3HN	1000	38	T/2	150	65	64	87
76mm A588 NG/WS	6HP	1000	38	T/4	- 60	-51	1.5	2
76mm A588 NG/WS	6HK	1000	38	T/4	- 60	-51	1.5	2
76mm A588 NG/WS	6HI	1000	38	T/4	- 30	-34	2	3
76mm A588 NG/WS	6HJ	1000	38	T/4	0	-18	5	7
76mm A588 NG/WS	6HM	1000	38	T/4	0	-18	4	5
76mm A588 NG/WS	6HL	1000	38	T/4	0	-18	3.5	5
76mm A588 NG/WS	6HE	1000	38	T/4	50	10	7	9
76mm A588 NG/WS	6HD	1000	38	T/4	50	10	9	12
76mm A588 NG/WS	6HO	1000	38	T/4	68	20	17	23
76mm A588 NG/WS	6HB	1000	38	T/4	68	20	9	12
76mm A588 NG/WS	6HA	1000	38	T/4	100	38	42	57
76mm A588 NG/WS	6HN	1000	38	T/4	100	38	15.5	21
76mm A588 NG/WS	6HF	1000	38	T/4	125	52	34	46
76mm A588 NG/WS	6HH	1000	38	T/4	125	52	29	39
76mm A588 NG/WS	6HL	1000	38	T/4	150	65	42	57
76mm A588 NG/WS	6HG	1000	38	T/4	150	65	40	54

APPENDIX : CVN IMPACT TEST DATA
(cont.)

Weld ID	Specimen ID	Current (A)	Voltage (V)	Zone	Temperature °F	Temperature °C	CVN Toughness ft-lb	CVN Toughness Joules
76mm A588 NG/WS	4HI	1000	38	HAZ	- 60	-51	1.1	1.5
76mm A588 NG/WS	4HM	1000	38	HAZ	- 30	-34	1.5	2
76mm A588 NG/WS	4HP	1000	38	HAZ	- 30	-34	1	1
76mm A588 NG/WS	4HC	1000	38	HAZ	0	-18	2	3
76mm A588 NG/WS	4HG	1000	38	HAZ	0	-18	2	3
76mm A588 NG/WS	4HA	1000	38	HAZ	32	0	2	3
76mm A588 NG/WS	4HF	1000	38	HAZ	50	10	4	5
76mm A588 NG/WS	4HO	1000	38	HAZ	68	20	16.5	22
76mm A588 NG/WS	4HE	1000	38	HAZ	68	20	5.5	7
76mm A588 NG/WS	4HJ	1000	38	HAZ	68	20	4.5	6
76mm A588 NG/WS	4HL	1000	38	HAZ	100	38	15	21
76mm A588 NG/WS	4HN	1000	38	HAZ	125	52	18.5	25
76mm A588 NG/WS	4HH	1000	38	HAZ	125	52	27	36
76mm A588 NG/WS	4HD	1000	38	HAZ	150	65	38	45
76mm A588 NG/WS	3TS	1300	38	T/2	- 60	-51	2.5	3
76mm A588 NG/WS	3TC	1300	38	T/2	- 60	-51	2	3
76mm A588 NG/WS	3TM	1300	38	T/2	- 20	-29	3.5	5
76mm A588 NG/WS	3TJ	1300	38	T/2	- 20	-29	3	4
76mm A588 NG/WS	3TP	1300	38	T/2	0	-18	4.5	6
76mm A588 NG/WS	3TR	1300	38	T/2	0	-18	3.5	5
76mm A588 NG/WS	3TG	1300	38	T/2	32	0	7	9
76mm A588 NG/WS	3TD	1300	38	T/2	32	0	10.5	14
76mm A588 NG/WS	3TS	1300	38	T/2	68	20	14	19
76mm A588 NG/WS	3TH	1300	38	T/2	68	20	14	19
76mm A588 NG/WS	3TI	1300	38	T/2	100	38	40	54
76mm A588 NG/WS	3TA	1300	38	T/2	100	38	34	46
76mm A588 NG/WS	3TE	1300	38	T/2	125	52	37	50
76mm A588 NG/WS	3TR	1300	38	T/2	125	52	70	95
76mm A588 NG/WS	3TC	1300	38	T/2	150	65	58	79
76mm A588 NG/WS	3TL	1300	38	T/2	150	65	66	89

APPENDIX : CVN IMPACT TEST DATA
(cont.)

Weld ID	Specimen ID	Current (A)	Voltage (V)	Zone	Temperature °F	Temperature °C	CVN Toughness ft-lb	CVN Toughness Joules
76mm A588 NG/WS	6TD	1300	38	T/4	- 80	-62	4.5	6
76mm A588 NG/WS	6TC	1300	38	T/4	- 60	-51	3	4
76mm A588 NG/WS	6TP	1300	38	T/4	- 60	-51	2.5	3
76mm A588 NG/WS	6TR	1300	38	T/4	- 20	-29	4.5	6
76mm A588 NG/WS	6TN	1300	38	T/4	- 20	-29	3.5	5
76mm A588 NG/WS	6TM	1300	38	T/4	0	-18	4.5	6
76mm A588 NG/WS	6TJ	1300	38	T/4	0	-18	6.5	9
76mm A588 NG/WS	6TA	1300	38	T/4	32	0	5.5	7
76mm A588 NG/WS	6TP	1300	38	T/4	32	0	6.5	9
76mm A588 NG/WS	6TQ	1300	38	T/4	68	20	12.5	20
76mm A588 NG/WS	6TG	1300	38	T/4	68	20	15	20
76mm A588 NG/WS	6TL	1300	38	T/4	100	38	49	66
76mm A588 NG/WS	6TD	1300	38	T/4	100	38	22	30
76mm A588 NG/WS	6TF	1300	38	T/4	125	52	47	64
76mm A588 NG/WS	6TK	1300	38	T/4	125	52	69	93
76mm A588 NG/WS	6TI	1300	38	T/4	150	65	66	89
76mm A588 NG/WS	6TE	1300	38	T/4	150	65	57	77
76mm A588 NG/WS	4TQ	1300	38	HAZ	- 60	-51	1.5	2
76mm A588 NG/WS	4TF	1300	38	HAZ	- 20	-29	5	7
76mm A588 NG/WS	4TB	1300	38	HAZ	- 20	-29	2.5	3
76mm A588 NG/WS	4TS	1300	38	HAZ	0	-18	4.5	6
76mm A588 NG/WS	4TC	1300	38	HAZ	0	-18	5	7
76mm A588 NG/WS	4TI	1300	38	HAZ	32	0	3.5	5
76mm A588 NG/WS	4TF	1300	38	HAZ	32	0	3.5	5
76mm A588 NG/WS	4TD	1300	38	HAZ	68	20	12	16
76mm A588 NG/WS	4TG	1300	38	HAZ	68	20	16	22
76mm A588 NG/WS	4TT	1300	38	HAZ	100	38	19	26
76mm A588 NG/WS	4TH	1300	38	HAZ	100	38	50	68
76mm A588 NG/WS	4TE	1300	38	HAZ	125	52	44	60
76mm A588 NG/WS	4TB	1300	38	HAZ	125	52	10	14
76mm A588 NG/WS	4TC	1300	38	HAZ	150	65	84	114
76mm A588 NG/WS	4TK	1300	38	HAZ	150	65	53	72

APPENDIX : CVN IMPACT TEST DATA
(cont.)

Weld ID	Specimen ID	Current (A)	Voltage (V)	Zone	Temperature °F	Temperature °C	CVN Toughness ft-lb	CVN Toughness Joules
76mm A588 NG/ST	3LL	1000	38	T/2	-100	-73	1.5	2
76mm A588 NG/ST	3LQ	1000	38	T/2	- 60	-51	2.5	3.4
76mm A588 NG/ST	3LS	1000	38	T/2	- 60	-51	2	2.7
76mm A588 NG/ST	3LE	1000	38	T/2	- 30	-34	4	5.4
76mm A588 NG/ST	3LR	1000	38	T/2	- 30	-34	4	5.4
76mm A588 NG/ST	3LB	1000	38	T/2	0	-18	5	6.8
76mm A588 NG/ST	3LA	1000	38	T/2	0	-18	7	9.5
76mm A588 NG/ST	3LC	1000	38	T/2	32	0	14	19
76mm A588 NG/ST	3LK	1000	38	T/2	32	0	13	18
76mm A588 NG/ST	3LG	1000	38	T/2	50	10	15	20
76mm A588 NG/ST	3LP	1000	38	T/2	50	10	13	18
76mm A588 NG/ST	3LD	1000	38	T/2	68	20	14	19
76mm A588 NG/ST	3LI	1000	38	T/2	68	20	18	24.4
76mm A588 NG/ST	3LN	1000	38	T/2	100	38	31	42
76mm A588 NG/ST	3LO	1000	38	T/2	100	38	38	51.5
76mm A588 NG/ST	3LF	1000	38	T/2	150	65	34	46
76mm A588 NG/ST	3LH	1000	38	T/2	150	65	44	60
76mm A588 NG/ST	6LQ	1000	38	T/4	- 60	-51	2.5	3.4
76mm A588 NG/ST	6LP	1000	38	T/4	- 60	-51	2	2.7
76mm A588 NG/ST	6LL	1000	38	T/4	- 30	-34	3.5	4.7
76mm A588 NG/ST	6LK	1000	38	T/4	- 30	-34	4	5.4
76mm A588 NG/ST	6LR	1000	38	T/4	- 30	-34	4	5.4
76mm A588 NG/ST	6LS	1000	38	T/4	0	-18	7	9.5
76mm A588 NG/ST	6LT	1000	38	T/4	0	-18	5	6.8
76mm A588 NG/ST	6LC	1000	38	T/4	32	0	8	10.8
76mm A588 NG/ST	6LE	1000	38	T/4	32	0	7	9.5
76mm A588 NG/ST	6LB	1000	38	T/4	50	10	17	23.1
76mm A588 NG/ST	6LJ	1000	38	T/4	50	10	10	13.6
76mm A588 NG/ST	6LD	1000	38	T/4	68	20	14	19
76mm A588 NG/ST	6LG	1000	38	T/4	68	20	15	20
76mm A588 NG/ST	6LN	1000	38	T/4	100	38	29	39.3
76mm A588 NG/ST	6LM	1000	38	T/4	100	38	26	36
76mm A588 NG/ST	6LA	1000	38	T/4	125	52	50	67.8
76mm A588 NG/ST	6LH	1000	38	T/4	125	52	44	60
76mm A588 NG/ST	6LI	1000	38	T/4	150	65	44	60
76mm A588 NG/ST	6LF	1000	38	T/4	150	65	43	58.5

APPENDIX : CVN IMPACT TEST DATA
(cont.)

Weld ID	Specimen ID	Current (A)	Voltage (V)	Zone	Temperature °F	Temperature °C	CVN Toughness ft-lb	CVN Toughness Joules
76mm A588 NG/ST	4LH	1000	38	HAZ	- 60	-51	1	1.4
76mm A588 NG/ST	4LK	1000	38	HAZ	- 60	-51	1.2	1.6
76mm A588 NG/ST	4LF	1000	38	HAZ	- 30	-34	2	2.7
76mm A588 NG/ST	4LJ	1000	38	HAZ	0	-18	3	4.1
76mm A588 NG/ST	4LA	1000	38	HAZ	0	-18	2	2.7
76mm A588 NG/ST	4LN	1000	38	HAZ	50	10	5.5	7.4
76mm A588 NG/ST	4LO	1000	38	HAZ	50	10	4	5.4
76mm A588 NG/ST	4LC	1000	38	HAZ	68	20	10	13.6
76mm A588 NG/ST	4LP	1000	38	HAZ	68	20	9	12.2
76mm A588 NG/ST	4LG	1000	38	HAZ	100	38	15	20
76mm A588 NG/ST	4LL	1000	38	HAZ	100	38	45	61
76mm A588 NG/ST	4LD	1000	38	HAZ	125	52	67	90.9
76mm A588 NG/ST	4LQ	1000	38	HAZ	125	52	55	74.6
76mm A588 NG/ST	4LB	1000	38	HAZ	150	65	61	82.7
76mm A588 NG/ST	4LM	1000	38	HAZ	150	65	65	88
76mm A588 NG/ST2	3VS	1300	35	T/2	-100	-73	4.5	6.1
76mm A588 NG/ST2	3VD	1300	35	T/2	-100	-73	4	5.4
76mm A588 NG/ST2	3VI	1300	35	T/2	- 80	-62	5	6.8
76mm A588 NG/ST2	3VH	1300	35	T/2	- 80	-62	5	6.8
76mm A588 NG/ST2	3VT	1300	35	T/2	- 60	-52	5.5	7.5
76mm A588 NG/ST2	3VR	1300	35	T/2	- 20	-29	13	17.7
76mm A588 NG/ST2	3VE	1300	35	T/2	- 20	-29	16	21.7
76mm A588 NG/ST2	3VA	1300	35	T/2	0	-18	26	35.3
76mm A588 NG/ST2	3VC	1300	35	T/2	0	-18	26	35
76mm A588 NG/ST2	3VN	1300	35	T/2	32	0	30	40
76mm A588 NG/ST2	3VP	1300	35	T/2	32	0	27	36.6
76mm A588 NG/ST2	3VS	1300	35	T/2	68	20	50	67.8
76mm A588 NG/ST2	3VO	1300	35	T/2	68	20	50	67.8
76mm A588 NG/ST2	3VG	1300	35	T/2	68	20	50	67.8
76mm A588 NG/ST2	3VM	1300	35	T/2	150	65	85	115
76mm A588 NG/ST2	3VJ	1300	35	T/2	150	65	79	107

APPENDIX : CVN IMPACT TEST DATA
(cont.)

Weld ID	Specimen ID	Current (A)	Voltage (V)	Zone	Temperature °F	Temperature °C	CVN Toughness ft-lb	CVN Toughness Joules
76mm A588 NG/ST2	6VH	1300	35	T/4	-100	-73	3.5	4.7
76mm A588 NG/ST2	6VI	1300	35	T/4	-100	-73	3.5	4.7
76mm A588 NG/ST2	6VT	1300	35	T/4	- 80	-62	7.5	10.2
76mm A588 NG/ST2	6VF	1300	35	T/4	- 80	-62	6	8.2
76mm A588 NG/ST2	6VQ	1300	35	T/4	- 60	-51	6.5	8.8
76mm A588 NG/ST2	6VO	1300	35	T/4	- 60	-51	10	13.6
76mm A588 NG/ST2	6VP	1300	35	T/4	- 20	-29	17	23.1
76mm A588 NG/ST2	6VN	1300	35	T/4	- 20	-29	22	29.8
76mm A588 NG/ST2	6VE	1300	35	T/4	0	-18	33	45
76mm A588 NG/ST2	6VK	1300	35	T/4	0	-18	27	36.6
76mm A588 NG/ST2	6VD	1300	35	T/4	32	0	42	57
76mm A588 NG/ST2	6VJ	1300	35	T/4	32	0	44	60
76mm A588 NG/ST2	6VB	1300	35	T/4	68	20	48	65
76mm A588 NG/ST2	6VG	1300	35	T/4	68	20	50	68
76mm A588 NG/ST2	6VA	1300	35	T/4	100	38	78	105
76mm A588 NG/ST2	6VC	1300	35	T/4	100	38	70	95
76mm A588 NG/ST2	6VL	1300	35	T/4	150	65	90	122
76mm A588 NG/ST2	6VS	1300	35	T/4	150	65	97	131
76mm A588 NG/ST2	4VC	1300	35	HAZ	-100	-73	2	3
76mm A588 NG/ST2	4VK	1300	35	HAZ	- 80	-62	4	5.4
76mm A588 NG/ST2	4VQ	1300	35	HAZ	- 60	-51	2.5	3.4
76mm A588 NG/ST2	4VI	1300	35	HAZ	- 60	-51	3	4
76mm A588 NG/ST2	4VA	1300	35	HAZ	- 20	-29	5	6.8
76mm A588 NG/ST2	4VM	1300	35	HAZ	- 20	-29	5	6.8
76mm A588 NG/ST2	4VH	1300	35	HAZ	0	-18	8	11.5
76mm A588 NG/ST2	4VF	1300	35	HAZ	0	-18	5	6.8
76mm A588 NG/ST2	4VG	1300	35	HAZ	32	0	9	12
76mm A588 NG/ST2	4VR	1300	35	HAZ	32	0	34	46
76mm A588 NG/ST2	4VB	1300	35	HAZ	32	0	34	46
76mm A588 NG/ST2	4VE	1300	35	HAZ	68	20	49	67
76mm A588 NG/ST2	4VS	1300	35	HAZ	68	20	39	53
76mm A588 NG/ST2	4VO	1300	35	HAZ	100	38	43	58
76mm A588 NG/ST2	4VP	1300	35	HAZ	100	38	83	113
76mm A588 NG/ST2	4VQ	1300	35	HAZ	100	38	64	87
76mm A588 NG/ST2	4VV	1300	35	HAZ	150	65	93	126
76mm A588 NG/ST2	4VJ	1300	35	HAZ	150	65	69	94